TEL AVIV UNIVERSITY
THE RAYMOND AND BEVERLY SACKLER
SCHOOL OF PHYSICS AND ASTRONOMY

אוניברסיטת תל-אביב
בית הספר לפיזיקה ואסטרונומיה
ע"ש ריימונד ובברלי סאקלר

Heavy Flavor Gauge Boson search at the LHC

חיפוש אחר בוזוני כיול כבדים במאיץ ההדרונים הגדול

Ph.D thesis

Presented to the

The Raymond and Beverly Sackler
School of Physics & Astronomy,
Tel-Aviv University

By

Avi Gershon[1]

אבי גרשון

Supervisor

Prof. Erez Etzion[2] ,

פרופ' ארז עציון

February 26, 2016

[1]email: avigersh@tau.ac.il
[2]email: erez.etzion@cern.ch

Contents

Chapter 1

Introduction

With this new era in particle physics, marked with the operational starting of the Large Hadron Collider (LHC) at the European laboratory of particle Physics (CERN) in Geneva, Experimental particle physics received the much needed oxygen it was missing in the previous years. This new era, enabled physicists to prove or rather disprove by setting exclusion limits on many of the new beyond the Standard Model (BSM) theories that accumulated over the years. This has been achieved due to the huge data collected with record energy during its first three years of operation.

Despite its many successes, the Standard Model (SM) [1] of particle physics is believed to be an effective field theory valid only for energies up to the TeV scale. Due to its uniquely large mass, the top quark is of particular interest for the electroweak symmetry breaking mechanism and could potentially be related to new physics phenomena. Several proposed extensions to the SM predict the existence of heavy particles that decay primarily to top quark pairs.

This thesis contains two parts: a theoretical motivation study that was done during the early stage of the PhD described in Section 2 and an experimental data analysis part.

The theoretical aspect of this work was done in collaboration with Dr. Gilad Perez and Dr. Seung J. Lee, at the time both from the Weizmann institute. This work included Monte Carlo modeling of flavor gauge boson models. The study of flavor gauge boson was implemented with the MOSES framework [2] and the PYTHIA [3] simulation code. Additional verification to these studies came from an independent implementation with MadGraph [4] by Dr. Lee. The Monte Carlo modelling was partly carried out during MCnet short-term studentship under the guidance of Dr Mark Sutton.

The experimental search is made in the top anti-top decay channel where one W from a top decays leptonically (to an electron or muon plus neutrino) and the W from the second top decays hadronically. This leads to a signature with one high-transverse- momentum lepton, large missing transverse momentum (from the escaping neutrino) and hadronic jets. The analysis is designed to deal with both boosted configurations where the top decay products overlap in the detector and with resolved configurations where the top decay products are all well separated in the detector. Generally, the decay products are more boosted when the invariant $t\bar{t}$ mass is larger. A variety of new physics scenarios give rise to heavy particles that decay primarily to $t\bar{t}$. High-mass particles that do this are particularly attractive targets for searches in light of recent measurements of the forward-backward asymmetry in $t\bar{t}$ at the Tevatron [5]. Examples of models that produce the signature of high-mass $t\bar{t}$ systems clustered about a particular mass are topcolor-assisted technicolor (TC2)1 which produces a top-philic Z'-like particle [6], [7] and [8], a Randall-Sundrum (RS) warped extra-dimension that would result in a bulk Kaluza-Klein (KK) gluon [9, 10] and a bulk Randall-Sundrum spin-2 graviton [11]. Several searches for $t\bar{t}$ resonances have been performed at hadron-hadron colliders. The Z' benchmark model considered here is dominated by $q\bar{q}$ initial states and thus Tevatron searches and early

LHC searches had comparable sensitivity to detect it. The CDF [12], [13] and [14] and $D\emptyset$ [15] collaborations have both performed searches for $t\bar{t}$ resonances using approximately 5 fb^{-1} integrated luminosity with the most stringent limit excluding a leptophobic topcolor Z' with mass less than 915 GeV. The CMS collaboration has published searches in the all-hadronic, dileptonic and lepton+jets decay channels [16], [17] and [18] which exclude a leptophobic topcolor Z' with $\Gamma_{Z'}/m_{Z'} = 1.2\%$ in the mass range < 1.5 TeV and a KK gluon with mass < 1.82 TeV. The previous searches at ATLAS were made using 2011 data: the first publication [19] looked at resolved configurations in the lepton+jets and the dilepton final states excluding a leptophobic topcolor Z' with mass less than 880 GeV; the second publication [20] considered boosted configurations in the lepton+jets channel only and excluded the same class of leptophobic topcolor Z' for masses from 600-1150 GeV. These first searches only used the first 2 fb^{-1} of the 2011 data. Subsequent searches were made using the full 2011 dataset in the all-hadronic [21] and lepton+jets channel [22]. The strongest limits comes from the latter, translating to lower limits on the Z' and KK gluon of 1.7 and 1.9 TeV respectively.

In the current research we have investigate the existence of new physics, first with a specific model that involves the existence of a new gauge bosons. We continue with participation in the ATLAS search for the resonance in $q\bar{q} \to t\bar{t}$ s-channel process. Here we look for wide spectrum of new physics signatures not limiting ourselves to a too specific theory beyond the Standard Model.

In the second chapter, we discuss the detection potential of $t\bar{t}$ resonance in proton proton collision in 7 TeV as well as some aspects for the design Run-2 LHC energy of 14 TeV. We begin with a theoretical description of the "Flavor Gauge Boson" model, continuing with theoretical calculations of the $t\bar{t}$ s and t-channel processes as derived this model.

Section three contains the experimental facilities including a description of the LHC accelerator and the ATLAS experiment.

In section four we present the ATLAS data analysis, now that the LHC "run1" data collection endeavor is finished and reached the unprecedented 20fb^{-1} of data at such a high energy. On the second chapter we present a search for s-channel resonance in $t\bar{t}$ based on the 14fb^{-1} dataset collected with the ATLAS detector at the first year of running at 8 TeV. Since ATLAS has modified several analysis tools after collecting this sample, these results were published independently as preliminary ATLAS results. ATLAS continued to collect additional 6fb^{-1} of proton-proton collisions data at 8 TeV. The ATLAS analysis of this sample is still ongoing but is expected to be published by ATLAS in the near future.

Chapter 2

Theoretical Motivation

2.1 Flavor physics introduction

"Flavor", in the context of this work, is used to describe several copies of the same gauge representation, namely several fields that are assigned the same quantum charges. We can also define the term "flavor physics" as the interactions that distinguish between different flavors. Ref [23] titled "Flavor Physics Constraints for Physics Beyond the Standard Model" contains comprehensive details of these ideas and is the basis of this work. When one looks for motivation for "flavor physics", one may look at interactions involving changes within the up-type (u, c, t) sector or within the down-type (d, s, b) flavors separately i.e. "flavor changing neutral current" (FCNC) processes. In the SM such processes are highly suppressed and are not possible at the tree level. This makes FCNC processes a unique probe for new physical processes, assuming that the new physics does not have the same flavor suppression as in the standard model. One can then compare to the SM even if it takes place at energy scales which are orders of magnitude higher than the weak scale[1].

[1]The electroweak or weak scale, is the energy scale around 246 GeV, a typical energy of processes described by the electroweak theory

This sensitivity to new physics is the main reason for the experimental effort to measure flavor parameters and the theoretical effort to interpret the new LHC data.

2.2 The flavor gauge boson model

We present a specific Flavor Gauge Boson (FGB) model with an $SU(3)$ symmetry between flavors with the same electric charge. In this model there are 24 FGBs with specific couplings to left and right handed particles, such that there are three different types of FGB as listed in table 2.1.

Up or Down type quarks	Chirality	Notation
Up and Down	Left	Q
Up	Right	U
Down	Right	D

Table 2.1: *The three different types of the FGB where* U *denotes the* u, c, t *up-type quarks and* D *denotes the* d, s, b *down-type quarks.*

In this model, the interaction can be written as,

$$\begin{aligned} &C \times (\tilde{g}_{\mathrm{Q}})_{ij}\, \bar{\mathrm{Q}}_i \Lambda^a_{ij} A^a_{Q\mu} \gamma^\mu \mathrm{Q}_j \\ &C \times (\tilde{g}_{\mathrm{U}})_{ij}\, \bar{\mathrm{U}}_i \Lambda^a_{ij} A^a_{U\mu} \gamma^\mu \mathrm{U}_j \\ &C \times (\tilde{g}_{\mathrm{D}})_{ij}\, \bar{\mathrm{D}}_i \Lambda^a_{ij} A^a_{D\mu} \gamma^\mu \mathrm{D}_j \end{aligned} \tag{2.1}$$

where Q_j, U_j and D_j are the j^{th} entries of the corresponding flavor-vectors seen in Table 2.1 (j=1,2,3 for u,c,t or d,s,b), $A^a_{q\mu}$ (q=Q,U,D) are the FGB vector fields associated with the a^{th} Gell-Mann matrix Λ^a (see Appendix), γ^μ are the Dirac matrices and C is a free dimensionless scaling factor, ranging between zero and three, as allowed by the FGB model.

In our specific model, all the couplings $(\tilde{g}_q)_{ij}$ are taken to be $\sqrt{2}$. One can define an

effective couplings as

$$\left(g_{\rm q}^{a}\right)_{ij} = C \times \left(\tilde{g}_{\rm q}\right)_{ij} \times \Lambda_{ij}^{a} \tag{2.2}$$

For example, the interaction of the right-handed up quark to A_U^3 (i=j=1), corresponding to the process $u + \bar{u} \to A_U^3$ is given by

$$(g_{\rm U}^3)_{11} = C \times \left(\tilde{g}_{\rm U}\right)_{u\bar{u}} \times \Lambda_{11}^3 = C \times \left(\sqrt{2}\right) \times \left(\frac{1}{\sqrt{2}}\right) \tag{2.3}$$

The partial width of A_q^a to decay into $q_i \bar{q}_j$ is given by,

$$\left(\Gamma_{\rm q}^{a}\right)_{ij} = \frac{N_c^F M}{4\pi \times 6} \left(\left(g_{\rm q}^{a}\right)_{ij}\right)^2 \tag{2.4}$$

where $N_c^F = 3$ is the number of colors, M is FGB mass which is taken to be the same for all 24 FGBs, and is assumed to be sufficiently high, so that the quark masses, including the top mass can be neglected.

Summing over i, j will then give the total width of A_q^a,

$$\Gamma_{\rm q}^{a} = \sum_{i=1}^{3}\sum_{j=1}^{3}\left(\Gamma_{\rm q}^{a}\right)_{ij} = \sum_{i=1}^{3}\sum_{j=1}^{3}\frac{N_c^F M}{4\pi \times 6}\left(\left(g_{\rm q}^{a}\right)_{ij}\right)^2 \tag{2.5}$$

The search for this model can have two main experimental routes, one via a s-channel and the other via t-channel (as can be seen in the next subsections). The signature chosen by us for studying the properties of these channels is the one that contains at least one outgoing *top*, the reason for doing so is two-fold. The first reason is that in some other versions of the FGB model, the coupling constants for heavy flavors (t, b vs c, s, u and d) are larger than the light flavors, rather than being equal, the technical details of this

phenomena are beyond the scope of this thesis. The second reason is that for high p_T jets, the top-jet is the only one which can be distinguished from the other quarks, as will be explained in section 2.4.

The $t\bar{t}$ cross section has been measured in [24]. The LHC experiments systematics and statistical errors are still higher than the Tevatron's uncertainties. Therefore, the Tevatron (CDF) $t\bar{t}$ cross section is used to constrain the FGB model parameters.

Taking into account FGB effect combined with the SM (including interference between SM and FGB model), with 10 percent allowed deviation, one can exclude the existence of an FGB with mass below 1.3 TeV [25] with the specific coupling scale C=1.

2.3 Implementation of the s-channel FGB Exchange

For s-channel flavor conserving processes, and due to Parton Distribution Function (PDF)'s suppression, only the Gell-Mann matrices Λ^3 and Λ^8 contribute (see Appendix).

Since Λ^3 and Λ^8 are diagonal, there is no flavor mixing.

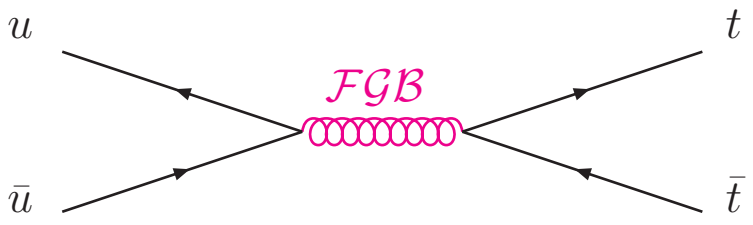

Figure 2.1: *The s-channel process considered in this document.*

The matrix element for this s-channel process (see also [26]),

$$q_i + \bar{q}_j \to A_q \to q_k + \bar{q}_l, \tag{2.6}$$

is given by,

$$\mathcal{M}_{\rm q}^{a} = \frac{\left(g_{\rm q}^{a}\right)_{ij}\left(g_{\rm q}^{a}\right)_{kl}}{(s-M^2)+iM\Gamma_{\rm q}^{a}} \tag{2.7}$$

from which one can obtain the differential cross-section $\frac{d\sigma}{d\hat{t}}$

$$\frac{d\sigma_{\rm q}}{d\hat{t}} = \frac{2}{\hat{s}}\frac{(N_C^q)_{kl}}{(N_C^q)_{ij}}2\pi\frac{1}{4\hat{s}(4\pi)^2}\frac{\hat{s}^2}{4}\left|\sum_a \mathcal{M}_{\rm q}^{a}\right|^2\left(1+4\lambda^2\cos\hat{\theta}\right)^2 \tag{2.8}$$

where $\hat{\theta}$ is the polar angle of the outgoing quark relative to the incoming quark in the $q\bar{q}$ rest frame, (with the azimuthal angle ϕ, distributed uniformly), $(N_C^q)_{kl}$ and $(N_C^q)_{ij}$ are the outgoing and incoming quarks colors, and λ is the helicity ($\lambda = \pm 1/2$) which must be the same for the incoming and outgoing quarks. Neglecting the *top* mass with respect to $\sqrt{\hat{s}}$,

$$\hat{t} = -\frac{\hat{s}}{2}(1-\cos\hat{\theta}) \tag{2.9}$$

The summation on a is performed over all FGBs which couple to the specific incoming and outgoing quark states.

2.3.1 Theoretical calculations with MOSES

Figures 2(a), 2(b), 3(a) and 3(b) present the differential and integrated cross sections for 14 Tev and 7 TeV collision energy [2], assuming $C = 2$, for s-channel $q+\bar{q} \to t\bar{t}$, the PDF set used was "cteq6m.LHpdf" [27] under the MOSES framework [2], which is a tool developed by our group and is introduced in the following sections.

[2]This energies were selected prior to the LHC run, and before the 8 TeV, data was collected. Now we know that LHC is expected in Run-2 to run at 13 TeV.

Figure 2.2: s-channel Plots at 14 TeV

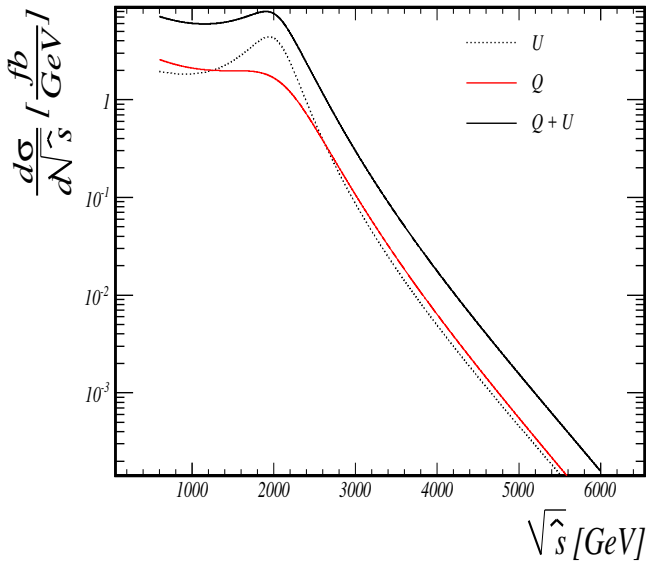

(a) Differential cross section for FGB mass of 2000 GeV. Dotted line indicates the U type, red line indicates Q type and black line indicates the sum of the two contributions. For the $\sqrt{\hat{s}}$ range between 600 and 6000 GeV, the U type total cross section is 4.786×10^3 fb and the Q type total cross section is 3.584×10^3 fb

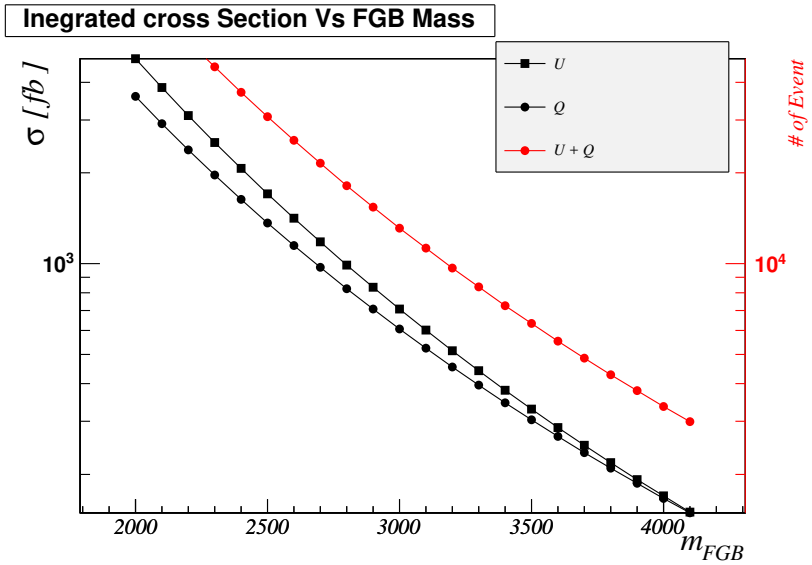

(b) Integrated cross section for $\sqrt{\hat{s}}$ between 600 and 6000 GeV as a function of FGB mass, for Q and U type FGB. The expected number of FGB events with integrated luminosity of 10 fb^{-1} is presented in the right scale.

Figure 2.3: s-channel Plots at 7 TeV

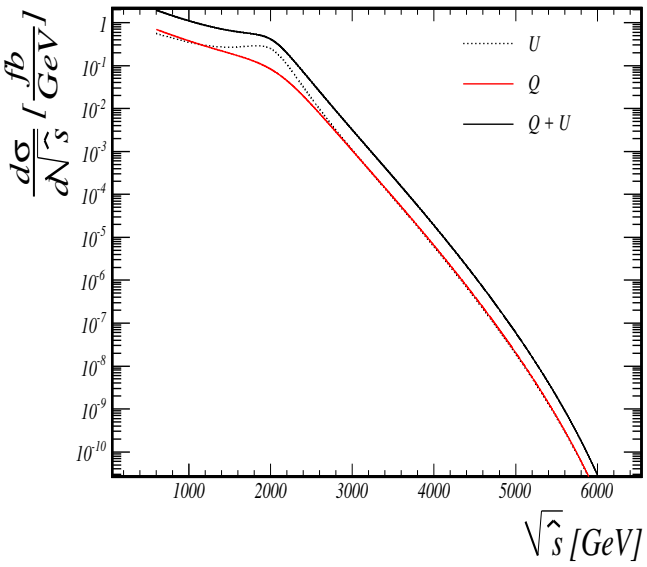

(a) Differential cross section with FGB mass of 2000 GeV at 7 TeV collision energy. For the $\sqrt{\hat{s}}$ range between 600 and 6000 GeV, the U type total cross section is 5.158×10^2 fb, Q type total cross section is 4.333×10^2 fb

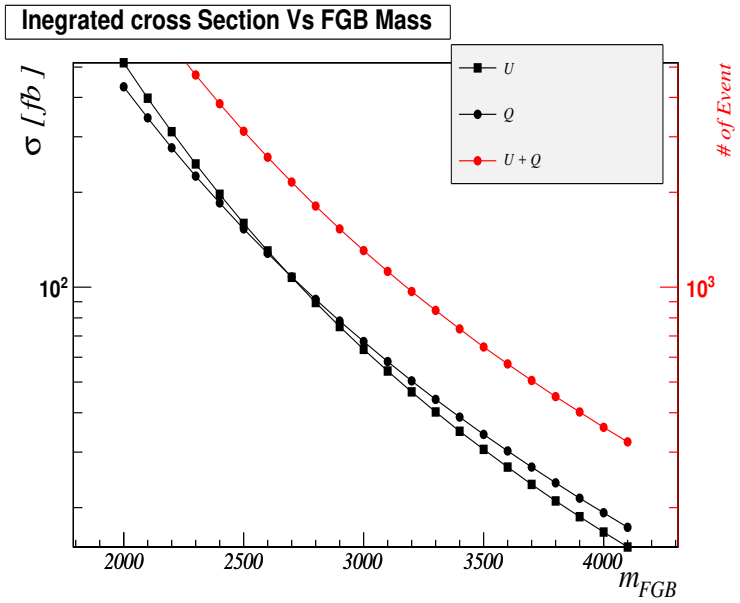

(b) Integrated cross section for $\sqrt{\hat{s}}$ between 600 and 6000 GeV as a function of FGB mass, for Q and U type FGB. The expected number of FGB events with integrated luminosity of 10 fb^{-1} is presented in the right scale.

2.4 The t-channel exchange process

The FGB model can introduce two different t-channel processes with t-quark in the final state, as in 2.4(a) and 2.4(b) where for 2.4(a) a single *top* process is obtained through an FGB exchange where the main processes are $u\bar{d} \to t\bar{b}, c\bar{s} \to t\bar{b}$ and their charge conjugates, while in 2.4(b) $t\bar{t}$ pair are produced

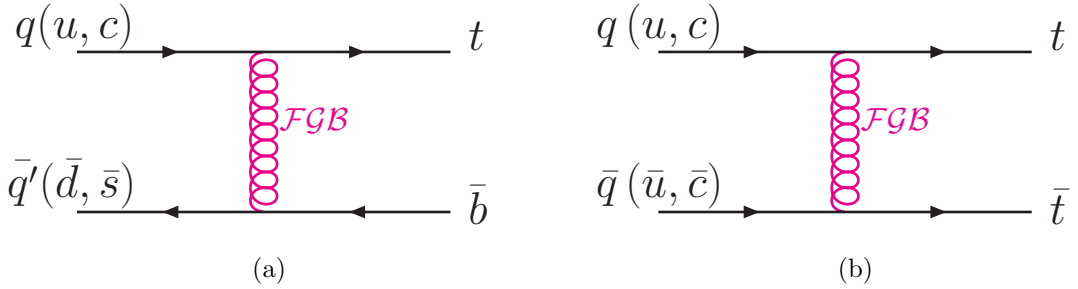

(a) (b)

Figure 2.4: *The t-channel investigated in this document is shown, where for type Q both (a) and (b) are possible and for type U only (b) is possible.*

Corresponding to the calculation done in [28] and [29] for single *top* at the SM [3], we can now write the differential cross section for $u\bar{d} \to t\bar{b}\,(d\bar{u} \to b\bar{t})$, $u\bar{u} \to t\bar{t}$ (distinguishable particles) as

$$\frac{d\sigma_{Q,\mathrm{u\bar{d}}\to\mathrm{t\bar{b}}}}{d\hat{t}} = 2^{\dagger} \times \pi \frac{1}{(4\pi)^2} \left(\left(g_{\mathrm{q}}^{a}\right)_{u\bar{t}} \left(g_{\mathrm{q}}^{a}\right)_{d\bar{b}} \right)^2 \frac{\hat{u}\left(\hat{u} - M_t^2\right)}{\hat{s}^2 \left(\hat{t} - M^2\right)^2} \tag{2.10}$$

,

$$\frac{d\sigma_{Q/U,\mathrm{u\bar{u}}\to\mathrm{t\bar{t}}}}{d\hat{t}} = 2 \times \pi \frac{1}{(4\pi)^2} \left(\left(g_{\mathrm{q}}^{a}\right)_{u\bar{t}} \left(g_{\mathrm{q}}^{a}\right)_{\bar{u}t} \right)^2 \frac{\left(\hat{u} - M_t^2\right)^2}{\left(\hat{s} - M_t^2\right)^2 \left(\hat{t} - M^2\right)^2} \tag{2.11}$$

where we have neglected the mass of b quark, M is the FGB mass and $\hat{t}$ is given by

$$\hat{t} = -\frac{\hat{s}}{2}\left(1 - \frac{M_t^2}{\hat{s}}\right)\left(1 - \cos\hat{\theta}\right) \tag{2.12}$$

[3] The single *top* SM cross section for $W^{\pm}$ t-channel exchange with incoming quark anti-quark pairs is $\frac{d\sigma_{Q,\mathrm{b\bar{d}}\to\mathrm{t\bar{u}}}}{d\hat{t}} = \pi g_w^4 \frac{\left(\hat{u}-M_b^2\right)\left(\hat{u}-M_t^2\right)}{\left(\hat{s}-M_b^2\right)^2\left(\hat{t}-M^2\right)^2}$, where $g_w^2 = \frac{\alpha}{2\sin\theta_w{}^2}$

[†] This factor 2 is due to constructive interference between two contributing FGB's, i.e., two Gell-Mann matrices.

and

$$\hat{s} + \hat{t} + \hat{u} = M_t^2 + M_{t/b}^2 \tag{2.13}$$

The t-channel single *top* is sensitive to physics beyond the SM (BSM), in the SM the FCNC is forbidden at the tree level, as as such, its measurement can serve as an evidence for new physics. In the following chapters we present a comparison between the SM and the expected BSM signatures.

2.5 Standard model background for FGB model

In the following sections we will address the SM background for this model.

2.5.1 The Standard Model Production of Single *top* and $t\bar{t}$ at the LHC

Top quark production in the SM, as reviewed in [30], is dominated by two main processes. The first one is the electroweak production of single *top* where the main contributing diagrams are plotted in figures 2.5 and 2.6. The expected total cross-section is 300 pb for proton-proton collisions at the center of mass energy of 14 TeV ([31], [30] and [32]). The second one is the $t\bar{t}$ pair production as seen in figure 2.7 with Next to Leading Order (NLO) level total cross section estimated to be 833 pb for proton-proton collisions with center of mass energy of 14 TeV, where about 90% of the events come from gluon-gluon fusion.

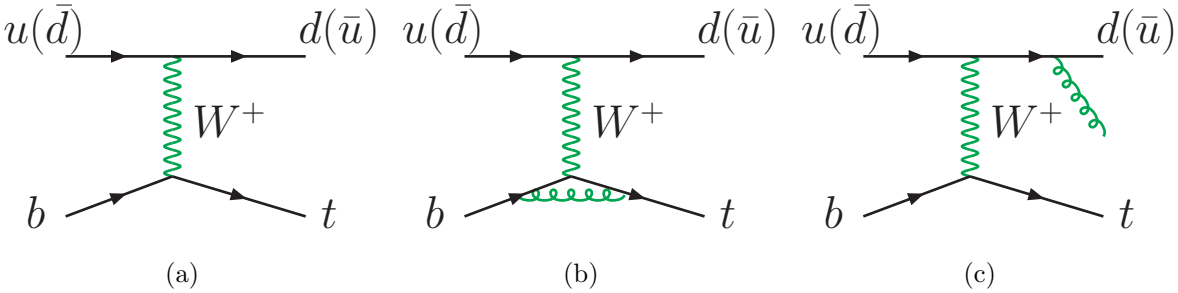

Figure 2.5: *(a) Leading order Feynman diagram for W-gluon fusion single top production. (b) and (c) are two examples of α_s correction to leading order diagram, (b) is a correction to the b vertex and (c) is a final state radiation of a gluon.*

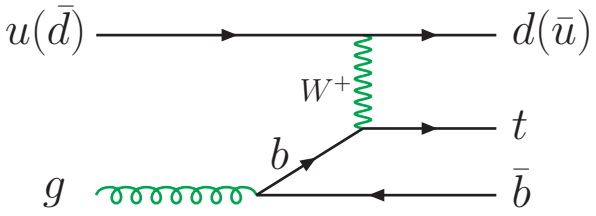

Figure 2.6: *Next to leading order single top production diagram.*

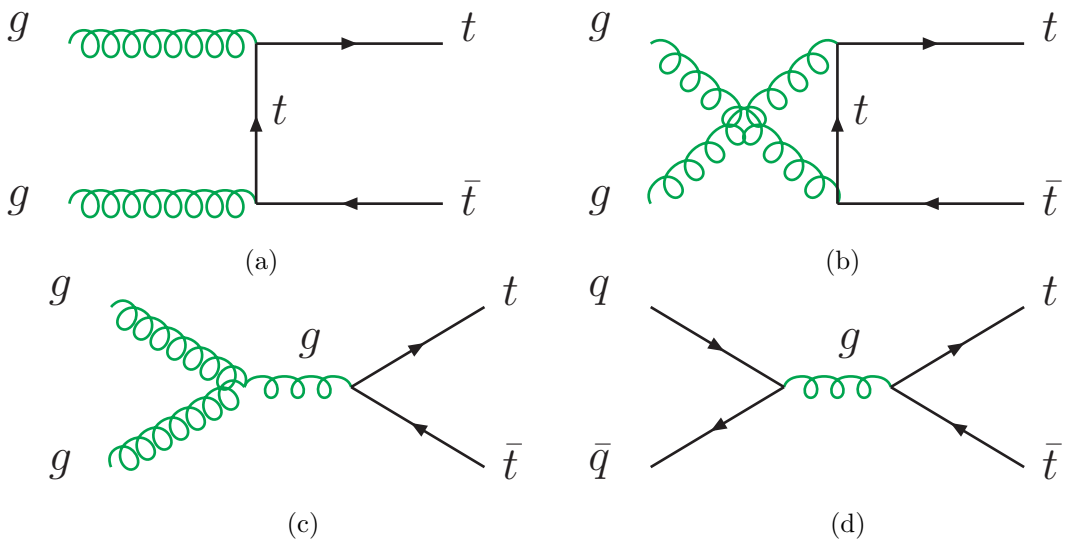

Figure 2.7: *SM $t\bar{t}$ pair production at the LHC*

2.5.2 Standard model *top* decay

The *top* quark, because of its huge mass, is extremely short lived with a predicted lifetime of only about 5×10^{-25} sec. As a result the *top* quarks will decay before they start hadronizing into *top* hadrons. More than 99% of the time, the decay products will be a W boson and

a *bottom* (b) quark. The W boson may decay hadronically into a pair of light quarks or leptonically into a lepton-neutrino pair. A *top* pair production is characterized by two W's (W^+ and W^-) and two b-jets from the $t\bar{t}$ pair decays.

2.5.3 Standard Model Background From Di-jets

One of the dominant sources of background to this search comes from production of two light (non-*top*) jets. This SM jet production may be wrongly classified either as a single *top* or sometimes even as a $t\bar{t}$ final state. Di-jets can come from $qg \to qg$, $qq \to qq$, $gg \to gg$, $q\bar{q} \to q\bar{q}$, $q\bar{q} \to gg$ and $gg \to q\bar{q}$. The key features that may allow one to distinguish between the signal and this source of background are the jet shapes, jet transverse momentum (p_T) and the angular distribution of the jets.

2.6 Reconstruction of boosted *top* jets.

At the LHC the top quark mass is much lighter than the beam energy and therefore it will be produced as a collimated single jet with very high transverse momenta. Therefore, in order to identify $t\bar{t}$ and single *top* events an algorithm to reconstruct a boosted *top* jet is needed, some examples can be found in [33] and [34]. For example in reference [33] the algorithm described is based mainly on the spatial structure and energy flow of the jets. While the QCD background high mass jets are characterized by two sub-jets (planar jets), the non QCD i.e. boosted *top* quarks decaying hadronically, are considered to have a three-parton structure in general (non-planar jets) as well as a very different energy flow (angular distribution of the energy within the jet). With the lowest order partonic QCD jet consisting of the original parton plus one soft gluon, there is no resemblance to

any possible pattern of *top* decays. Using the characteristics mention above, a method of template overlaps was developed, designed to filter targeted highly boosted particles (such as the FGB) decays from QCD jets and other background. Template overlaps are functional measures that quantify how well the energy flow of a physical jet matches the flow of a boosted partonic decay. Any region of the partonic phase space for the boosted decays defines a template.

Their study included several Monte Carlo (MC) generators (without any detector simulation) and the jet reconstruction algorithm in use was the anti-k_T algorithm.

The relevant results for the reconstruction of *top* jets at high p_T can be seen in Table 2.2.

This and other algorithms will have to be investigated with MC samples using full detector simulation.

	Jet mass cut only		Mass cut + Template overlap	
	Top-jet efficiency [%]	fake rate [%]	Top-jet efficiency [%]	fake rate [%]
PYTHIA 8	58	3.6	21	0.022
MG/ME	52	3.7	11	0.017
SHERPA	34	3.2	7	0.032

Table 2.2: *Efficiencies and fake rates for jets with $R = 0.5$ (using anti-k_T : $D = 0.5$), 950 GeV $\leq p_0 \leq$ 1050 GeV the jet energy, 160 GeV $\leq m_J \leq$ 190 GeV and $m_{top} =$ 174 GeV. The left pair of columns show efficiencies and fake rates found by imposing the jet mass window only. For the different MC simulations different mass cuts and template overlaps have been applied. MG/ME is MadGraph/MadEvent [4].*

2.7 Monte Carlo Study

In order to perform an MC study, we first modified MOSES - an MC framework that has been developed by our group at Tel Aviv University to support FGB generation. Signal and background MC samples generated within this framework were utilised for efficiency

and background estimate studies.

2.7.1 Monte Carlo implementation within the MOSES environment

In the summer of 2010, I participated in a MCnet project under the supervision of Dr. Mark Sutton. In this project I have implemented the s and t-channel of the FGB process in MOSES as well as a stand alone PYTHIA 8 class [3] ("sigma2procces"). Collaborating with the theorists G. Perez and S. J. Lee (Weizmann institute), we verified the t and s-channel calculations. The implemented s-channel has been introduced to the PYTHIA authors at Lund.

Working closely with my colleagues at the Tel Aviv group, I have written an event reader for MOSES. This event reader provides a user friendly and flexible simulation generator interface for new physics processes within the MOSES framework.

The event reader allows one to run over a root file [35] generated by MOSES and to store its physical quantities such as energy and momentum of electrons, muons and jets (three different types of jet algorithms) in the memory for further implementations.

2.7.2 FGB Simulation Studies

The generation of MC events was done via PYTHIA 8 utilizing MOSES 1.3.4, this work has been verified independently with the MADGRAPH simulation program.

To reduce the level of SM di-jet events, all events are generated with the requirement of at least two outgoing jets with $p_T > 10$ GeV and $\sqrt{\hat{s}} > 1000$ GeV. The SM background for the s-channel is dominated by $t\bar{t}$ events (fakes and real, see table 2.2 for the fake and efficiency rates). For the t-channel the main background comes from single *top* events.

Clearly the fake rate for single *top* is much higher than for $t\bar{t}$ final state.

The t-channel $u\bar{d} \to t\bar{b}$ is a FCNC process that does not exist in the SM (at the tree level). For the SM single *top* production rate such as $b\bar{u} \to t\bar{d}$ is low because it occurs only by charge current weak interaction. Therefore, we have chosen to focus our studies on this channel.

The differential cross section for t-channel and a comparison to fake SM signal can be seen in figure 2.8 where a cut on $\left|\cos\hat{\theta}\right| < 0.8$ was applied. Figures 2.9(a) and 2.9(b) show the angular dependence of the FGB model versus the SM, here the cut $\sqrt{\hat{s}} > 1200$ GeV was applied. Figures 2.10(a) and 2.10(b) show scatter plots of $\sqrt{\hat{s}}$ vs. $\cos\hat{\theta}$ where both cuts have been applied. The expected number of events after the cuts for the background and signal in the t-channel are listed in tables 2.3 and 2.4 respectively.

The s-channel results can be seen in Figs. 2.11(a) (7 TeV) and 2.11(b) (14 TeV). The expected number of events for 10 fb^{-1} after $\left|\cos\hat{\theta}\right| < 0.8$ and $\hat{s} > 1500$ GeV cuts for the background and signal in the s-channel are listed in table 2.5.

SM	$xx \to JJ$	$xx \to t\bar{t}$	$xx \to tJ$	Sum
$\left\|cos\hat{\theta}\right\| < 0.8$	1488	622	24	2134
$\sqrt{\hat{s}} > 1200$ GeV	10058768	501	433	10059702
Both cuts	489	189	10	688

Table 2.3: *The number of SM background events expected for integrated luminosity of* 10^{-1} fb. *The cut* $p_T > 10$ GeV *was applied at the generation level and the samples were generated for* 1 TeV$< \sqrt{\hat{s}} <$ 5 TeV. *The first row shows the event number after applying the* $\cos\hat{\theta}$ *cut only, the second row shows the number of events expected when only the* $\sqrt{\hat{s}}$ *cut is applied and the last line shows the number of events when both cuts are applied.*

FGB:Mass	1300	1500	1500	1500
FGB:Scaling	1.0	1.3	1.0	2.1
$\left\|\cos\hat{\theta}\right\| < 0.8$	184	314	116	2119
$\sqrt{\hat{s}} > 1200$ GeV	166	294	105	2057
Both cuts	100	176	65	1229

Table 2.4: *The number of events expected for integrated luminosity of* 10 fb^{-1} *for different FGB masses and scaling,* $p_T > 10$ GeV *was applied at the generation level and the samples were generated for* 1 TeV$< \sqrt{\hat{s}} <$ 5 TeV. *The first row shows the event number after applying the* $\cos\hat{\theta}$ *cut only, the second row shows the number of events expected when only* $\sqrt{\hat{s}}$ *cut is applied and the last row shows the number of events when both cuts are applied.*

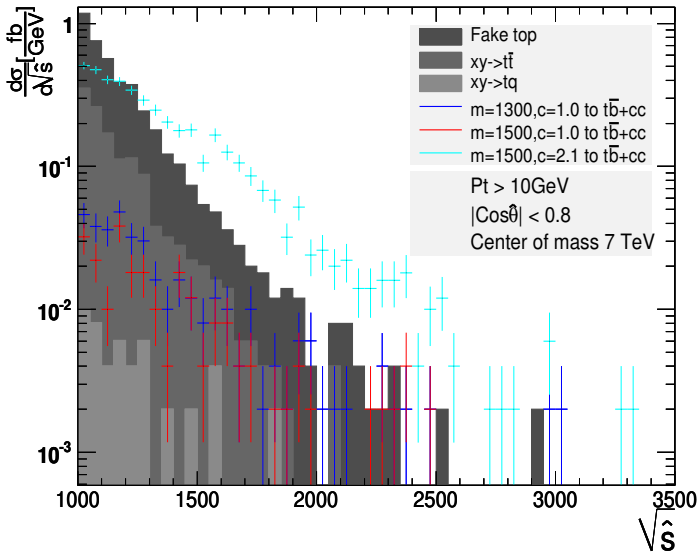

Figure 2.8: t-channel generation. Histograms are presented for each of the Q type relevant for a $t\bar{b}$(+CC) final state. The SM process taken into account are $gg \to gg$, $gg \to q\bar{q}$, $q\bar{q} \to q\bar{q}$, $qq \to qq$, $q\bar{q} \to t\bar{q}$, $qq \to tq$, $qg \to qg$, $gg \to t\bar{t}$, $q\bar{q} \to t\bar{t}$. m denotes the FGB mass and c denotes the scaling factor assumed.

	7 TeV	14 TeV
SM	1.5	32.9
Q type	3.7	69.3
U type	8.0	126.1

Table 2.5: *The number of events expected at* 10 fb^{-1} *in the s-channel with a final* $t\bar{t}$ *state, where the FGB mass is 2 TeV and the scaling equals to 2. A requirement that* $p_T > 10$ GeV *was applied at the generation level and the samples were generated for* 1 TeV$< \sqrt{\hat{s}} <$ 5 TeV. *The event number given is after applying* $\left|\cos\hat{\theta}\right| < 0.9$ *and* $\hat{s} > 1500$ *GeV.*

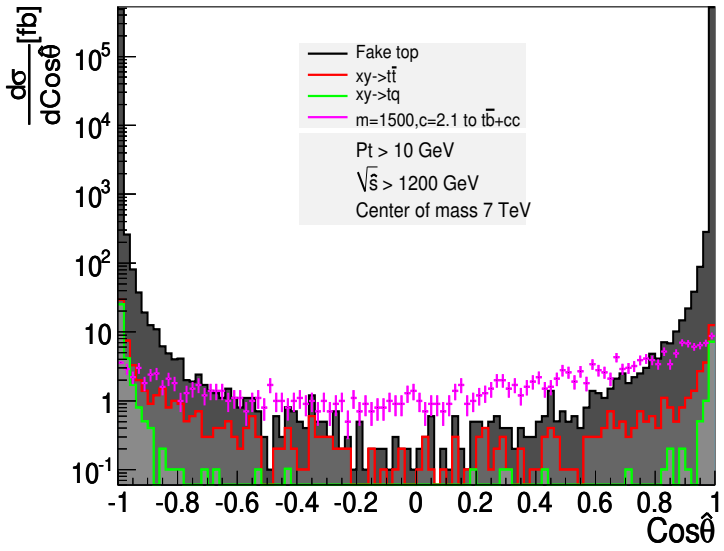

(a)

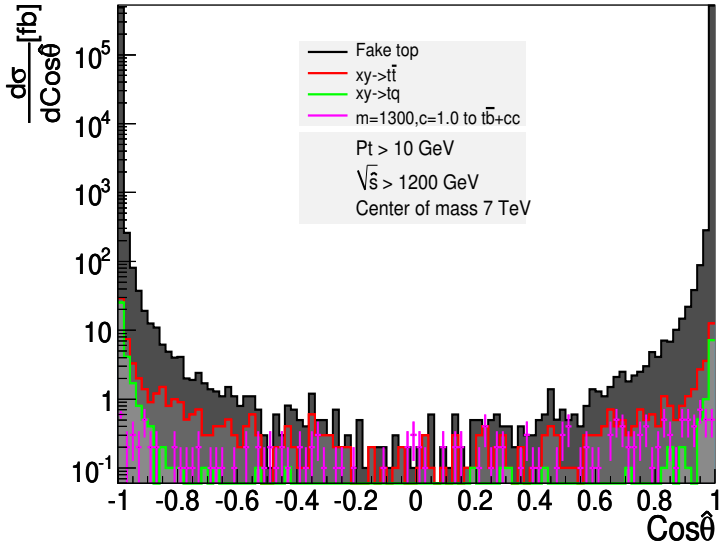

(b)

Figure 2.9: t-channel scattering plots are presented for the Q type relevant for a $t\bar{b}$(+CC) final state. The SM process taken into account are $gg \to gg$, $gg \to q\bar{q}$, $q\bar{q} \to q\bar{q}$, $qq \to qq$, $q\bar{q} \to t\bar{q}$, $qq \to tq$, $qg \to qg$, $gg \to t\bar{t}$, $q\bar{q} \to t\bar{t}$. m denotes the FGB mass and c denotes the scaling factor assumed. Plots 2.9(a) and 2.9(b) are for different masses and couplings.

2.8 Conclusions

In this chapter we have shown, that FGB signal can be detected under some specific FGB coupling - LHC energy setup. Furthermore, we have also shown that the "standard" s-channel process have a good chance of being detected utilizing boosted objects resonance search techniques.

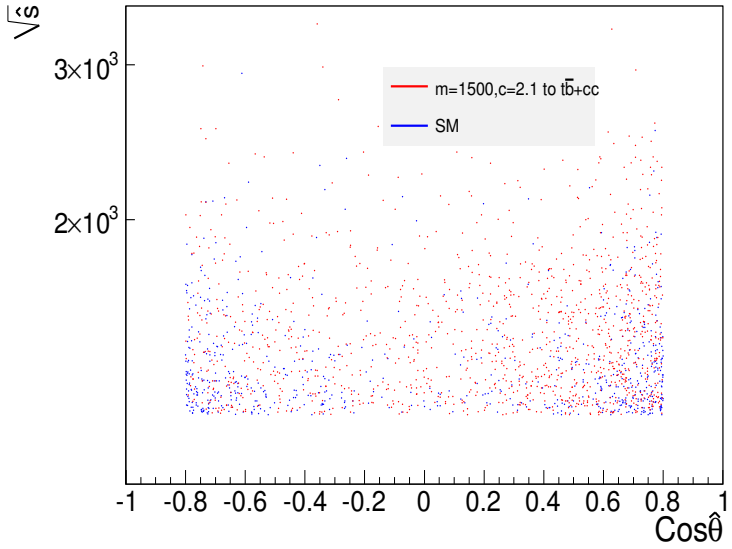

(a)

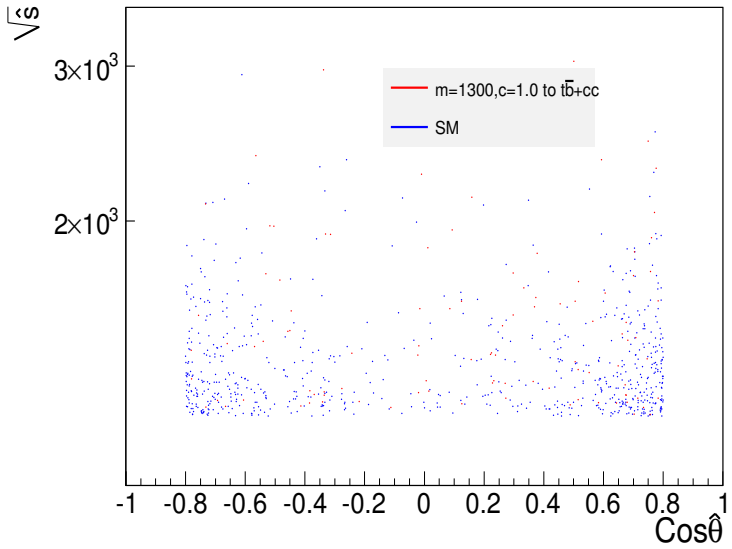

(b)

Figure 2.10: t-channel scattering plots after applying all cuts i.e. $\left|\cos\hat{\theta}\right| < 0.8$, $\sqrt{\hat{s}} > 1200$ GeV and $p_T > 10$ GeV are presented for the Q type relevant for a $t\bar{b}$(+CC) final state. The SM process taken into account are $gg \to gg$, $gg \to q\bar{q}$, $q\bar{q} \to q\bar{q}$, $qq \to qq$, $q\bar{q} \to t\bar{q}$, $qq \to tq$, $qg \to qg$, $gg \to t\bar{t}$, $q\bar{q} \to t\bar{t}$. m denotes the FGB mass and c denotes the scaling factor assumed. Plots 2.10(a) and 2.10(b) are for different masses and couplings.

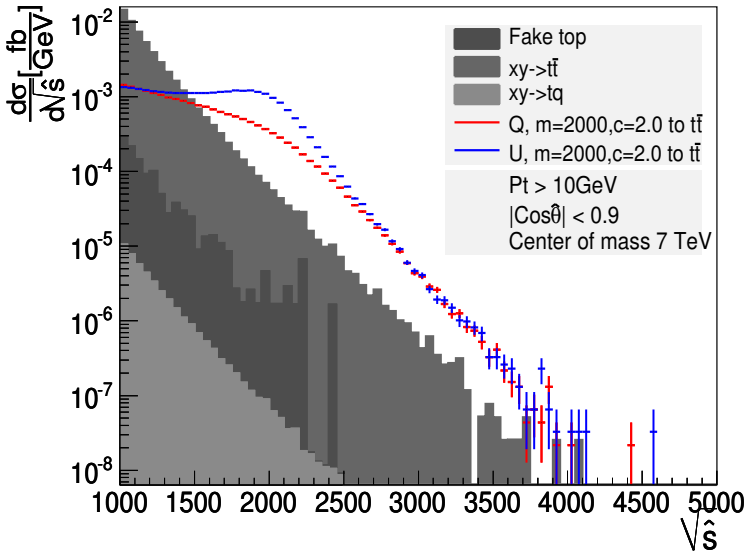

(a) 7 TeV

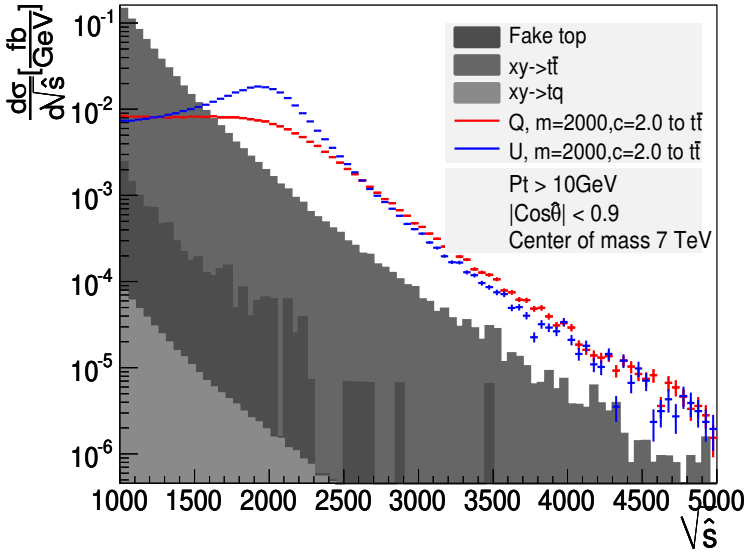

(b) 14 TeV

Figure 2.11: s-channel generation. Histograms are presented for each of the quark types relevant for a $t\bar{t}$ final state. The SM process taken into account are $gg \to gg$, $gg \to q\bar{q}$, $q\bar{q} \to q\bar{q}$, $qq \to qq$, $q\bar{q} \to t\bar{q}$, $qq \to tq$, $qg \to qg$, $gg \to t\bar{t}$, $q\bar{q} \to t\bar{t}$. The FGB mass was taken to be 2 TeV and the scaling factor is 2.

Chapter 3

The Experimental Facility

3.1 The large hadron collider

3.1.1 Overview

The Large Hadron Collider (LHC) [36] is the most powerful state-of-the-art facility for particle physics research by colliding proton beams accelerated to record energies.

The LHC consists of a 27-kilometre ring of superconducting magnets with a number of accelerating structures to boost the energy of the particles along the way. During the 2010-2012 period the LHC has managed to reach unprecedented center-of-mass energy of up to 8 TeV at a peak instantaneous luminosity of almost $10^{34} cm^{-2} s^{-1}$. Next, the LHC is planned to increase energy even further, up to the design value of 13-14 TeV, along with a further increase of the luminosity. Apart from proton-proton collisions, the LHC machine is also capable of accelerating and colliding beams of heavy ions as well as heavy ions against protons.

The main goal of the LHC was to discover the Higgs boson and the exploration of the SM in the TeV energy range. The search for the Higgs boson has succeeded to discover

the Higgs boson [37] and reached the phase of studying its properties along with searches for new physics involved with the new discovered Higgs boson. Another equally important goal in the design of the LHC, is the search for potential new physics signatures one expects to observe at the TeV energy regime.

Located at the CERN laboratory outside Geneva, about 100 meters deep underground, the LHC is about 27 km in circumference Figure (3.1). The proton (heavy-ion) beams are running in two different beam-pipes, and intersect in four interaction points, where the four major experiments that study the collisions they produce are installed, as shown in Figure3.1. This allows particles of the same charge - proton-proton (heavy ions) to be accelerated in opposite directions, before bringing them into collisions. The experiments are ATLAS [38], CMS [39], ALICE [40], and LHCb [41]. In addition, there are also three minor (more specific) experiments operating at LHC. These are LHCf [42], TOTEM [43] and MoEDAL [44].

3.1.2 The LHC experiments and the physics program of the ATLAS and the CMS experiments

Being multipurpose experiments, the ATLAS and CMS are optimized, first of all, to the searches for the SM Higgs boson and searches for the new physics that are generally predicted to occur at the TeV energy scale [45]. Apart from the TeV-scale physics, the high luminosity and increased cross-sections at the LHC enable further high precision tests of QCD, electroweak interactions, and flavor physics. For example, the top quark is produced at the LHC at a rate of a few tens of Hz, providing the opportunity to test its couplings and spin. The formidable luminosity and, therefore, the high interaction rate are required for these experiments, since the cross-sections for many processes mentioned above are

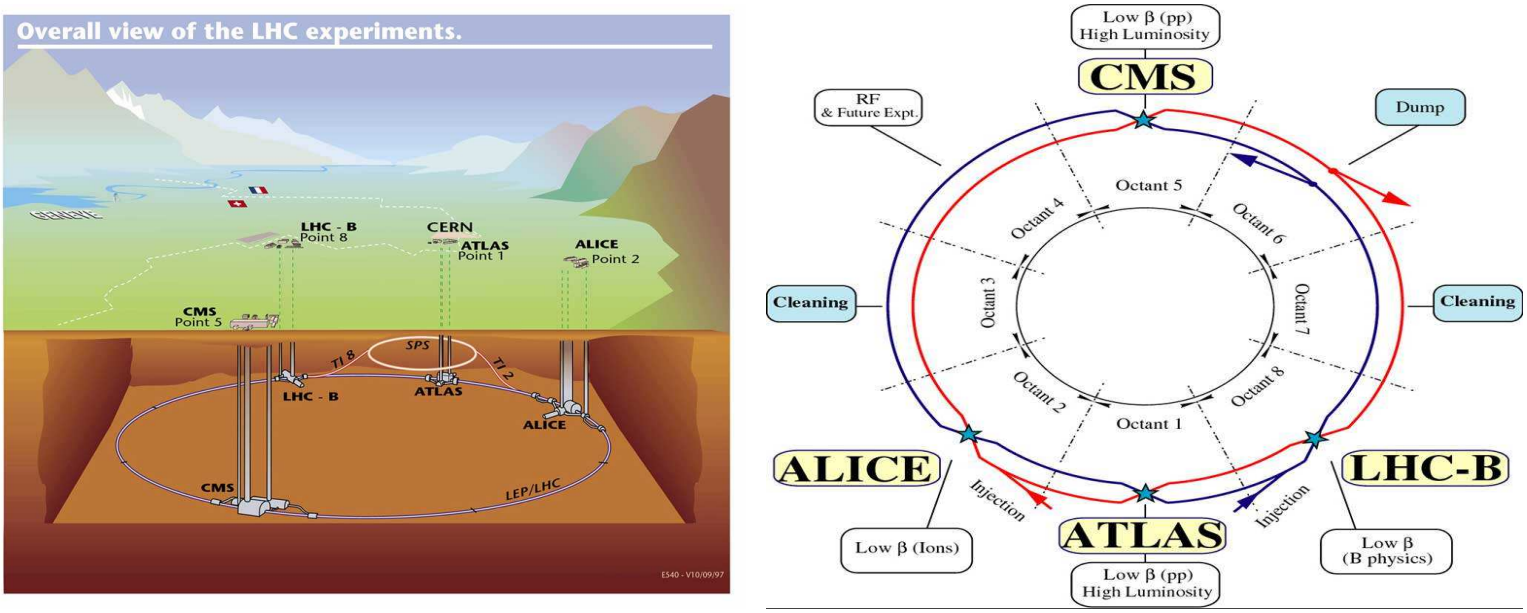

(a) (b)

Figure 3.1: The four main LHC experiments. This diagram shows the locations of the four main experiments (ALICE, ATLAS, CMS and LHCb). Located between 50 m and 150 m underground, huge caverns have been excavated to house the giant detectors. The SPS, the final link in the pre-acceleration chain, and its connection tunnels to the LHC are also shown.

very small. For example, the cross-section for the SM Higgs boson production is about ten orders of magnitude lower than the total cross-section of p-p scattering (Figure 3.2). At the same time the nature of hadron interactions implies that proton-proton collision products are dominated by the multi-jet production via the non-perturbative QCD processes. While prevailing over the other processes, multi-jet production usually occurs with low momentum (transverse momentum) transfer between the interacting hadrons. Hence, ATLAS and CMS are designed to explore those collisions which exhibit high transverse momentum transfer.

LHCb and ALICE

The LHCb as the name suggests, is designed for the studying of the b-quark physics. Its primary goal is to look for indirect evidence of new physics in CP violation and rare

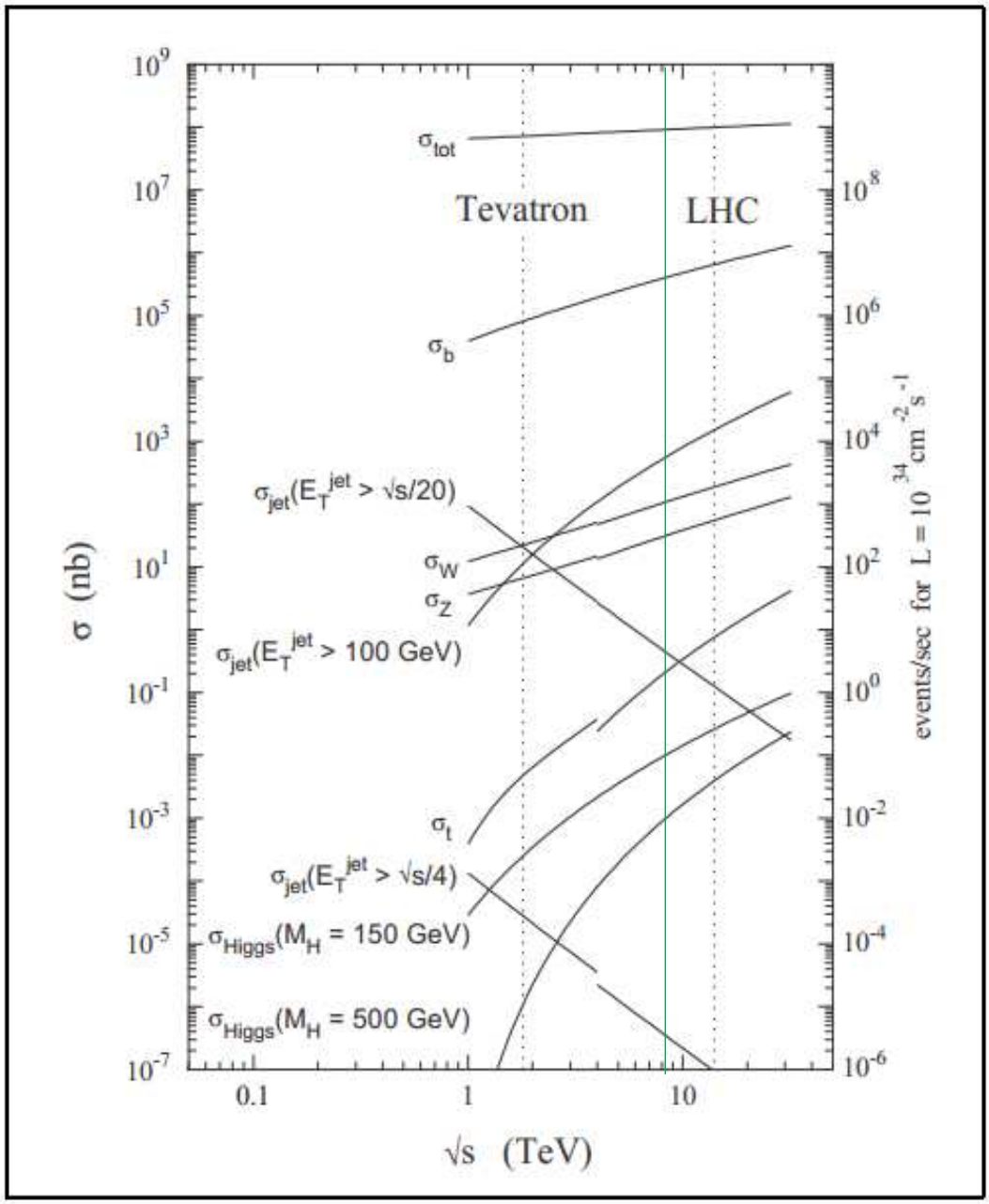

Figure 3.2: Cross-section and rates (for a luminosity of $1 \times 10^{34} cm^{-2} s^{-1}$) for various processes in proton-(anti)proton collisions, as a function of the centre-of-mass energy. The green line, indicates the 8 TeV location. Fig from [46]

decays of bottom and charm quarks hadrons [41]. ALICE, was designed for studying QCD e.g. the strong-interaction part of the Standard-Model (SM). Its main goal is to study strongly interacting matter such as quarks and gluon at extreme values of energy density and temperature resulting from nucleus-nucleus collisions [40].

LHCf, TOTEM and MoEDAL

LHCf experiment is designed to calibrate hadron interaction models used in high-energy cosmic ray physics by measuring the properties of forward neutral particles produced in $p-p$ interactions [42]. The MoEDAL experiment is dedicated to the searches for the Dirac's Magnetic Monopoles and other highly-ionizing Stable Massive Particles (SMPs) [44]. The TOTEM detector is dedicated to the measurement of the total proton-proton cross-sections with a luminosity-independent method and to the study of elastic and diffractive scattering at the LHC [43].

3.1.3 Luminosity of the LHC

Crucial parameters designed for any particle accelerator are the maximum achievable energy and luminosity. High energy in the center-of-mass, is required to allow the production of new, heavy particles. High enough rate of event production and, hence, a sufficiently high number of collisions and subsequently achievable statistical impact of rare processes is equally important for the detection of rare process.

Luminosity

The collision rate $\dot{n}$ for a given physics process of cross section σ is the product of the

luminosity L and the cross section

$$\dot{n} = L\sigma \tag{3.1}$$

Cross sections are usually given in units of barn (symbol b), where one b = $10^{-24} cm^2$. The luminosity of a collider is determined by the particle flux and geometry [47]. For head-on collisions, the instantaneous luminosity is

$$L = \frac{N_1 N_2 n_b f_{rev}}{A} \tag{3.2}$$

where N_1, N_2 are the number of particles per bunch in beam 1 and 2, n_b is the number of bunches, f_{rev} the revolution frequency and A the effective beam overlap cross section at the interaction point. For beams with Gaussian shape of horizontal and vertical r.m.s. beams sizes σ_x, σ_y colliding head on, the effective beam overlap is [48]

$$A = 4\pi\sigma_x\sigma_y \tag{3.3}$$

The main path to high luminosities in the LHC is, first, to use many bunches, nearly 3000, and, second, to reduce the transverse beam size at the interaction points by manipulations of the magnetic focusing system to squeeze beams before they are brought into collisions. Since the bunch intensities and beam sizes vary over time, the instantaneous luminosity is implicitly a function of time. In particle physics, the more relevant value is the integrated luminosity - the measure for the total number of events generated in the collider over a period of time and is defined as

$$\hat{L}(t_{end} - t_{start}) = \int_{t_{start}}^{t_{end}} L(t)dt \tag{3.4}$$

Beam energy

Although the synchrotron radiation from protons at LHC energies becomes noticeable, it is not a limitation on the maximum energy of proton beams. Instead, the limitation is dictated by the maximum bending strength of magnetic field B, needed to guide proton beams in the LHC tunnel [48]. According to this, the maximal proton momentum is

$$P = B \cdot r \tag{3.5}$$

where r the bending LHC radius with the value of $r = 2804$ m, given by the LHC tunnel geometry. Numerically, the maximal momentum is

$$P[GeV/c] = B[T] \cdot r \frac{[m]}{3.336} \tag{3.6}$$

The LHC is equipped with superconducting NbTi dipole magnets operated at superfluid Helium temperature of 1.9 K. This allows for magnetic field approaching 8.3 T and, therefore, maximal proton momentum of up to 7 TeV/c (this corresponds to 14 TeV centre-of-mass energy of colliding protons). This is almost the maximal magnetic field that can be achieved with existing NbTi superconductors [49]. In other words, the LHC parameters for the magnetic field and beam intensity are designed to get the maximum energy and luminosity achievable with the current technology. The comprehensive list of LHC operation parameters can be found in Ref. [48].

3.1.4 The LHC magnet system

The LHC is unique among superconducting synchrotrons, because its operating temperature is below 2 K to maximize the field strength of the superconducting magnets with NbTi windings [49]. Apart from dedicated magnets in the interaction points, the LHC magnets characteristic can be summarized in two types:

1. dipole magnets - required to bend particle trajectories in the LHC ring.

2. quadrupole magnets - required for the stabilization of the particle trajectories and the transverse r.m.s. beam size.

Being placed in the old LEP (previous $e^+ - e^-$ CERN machine) collider's tunnel [50], the LHC has a total length of 27.6 km. This includes 5 km split into 8 straight sections and space for dispersion suppression, and 22 km split into 8 arc sections of continuous curvature, as shown in Figure 3.1. The arc sections are equipped with dipole and quadrupole magnets. The distribution of the arc space between dipole and quadrupole magnets is dictated by the tradeoff between the achievable maximum dipole field and quadrupole gradients and the feasible maximum magnet aperture. This led to the design of rather long dipole magnets (15 m), requiring a slightly curved magnet design with a 5 cm Sagitta, covering in total approximately 80% of the arc sections of the old LEP tunnel [51].

3.1.5 The LHC accelerator chain and proton bunch structure

Before entering the main LHC ring protons or ions require a series of pre-accelerators. The energy of proton gradually rises with each step. It starts from 50 MeV in the first stage in the linear accelerator "LINAC", then it enters to the first circular accelerator, the Proton Synchrotron Booster (PSB), which yields the energy of 1.4 GeV, followed by

Proton Synchrotron (PS) which increases energy up to 25 GeV. Finally, the Super Proton Synchrotron (SPS) increases proton energy up to 450 GeV, which is the injection energy of protons in LHC. The pre-acceleration scheme is shown in Figure 3.3. The more in-depth description of LHC accelerating facilities can be found in Ref. [52]. The particle motion in LHC ring is constrained into longitudinal "buckets" using a radio frequency (RF) systems [53], [54]. The RF-frequency of the LHC is 400 MHz which corresponds to 75 cm wavelength or buckets of 2.5 ns length. The LHC circumference is 35640 RF-wavelengths which would theoretically allow for the same number of proton bunches. Filling all buckets with particles would produce collisions spaced by only 37.5 cm. However, a more realistic bunch spacing for the LHC is one per 10 RF-buckets or 25 ns. In other words, only one of ten buckets is filled with protons (proton bunch) while other nine are empty. It is constrained by the so-called multipactoring effects [55], like the electron-cloud effect [56], [57], and the strength and number of acceptable parasitic long-range collisions in the common vacuum chamber of the two beams. The total beam current is constrained by hardware limitations and collective effects, like multi-bunch instabilities [48].

Although the designed bunch spacing at LHC is 25 ns, it was so far running with minimum bunch spacing of 50 ns, which corresponds to the potential maximum number of 1400 bunches per beam. This is due to beam and vacuum instabilities produced by the electron cloud effect. This effect has been predicted for the LHC [57] and the beam cleaning procedure was done first with bunch spacings of 75 ns (up to April 2011) and then with bunch spacings of 50 ns. Following the successful beam cleaning runs with 50 ns spacing it was decided to keep physics operation at this value of bunch spacing [48]. Since bunch spacing was eventually lower than the designed value, the high integrated luminosity, envisioned at LHC, was attained by increasing the number of protons per bunch ("fatter"

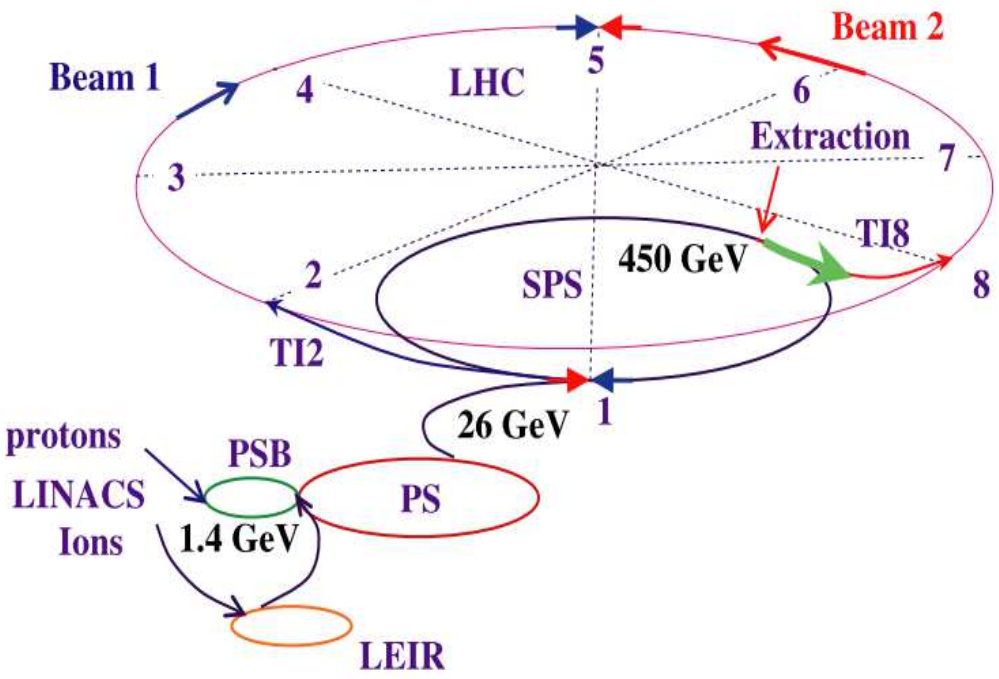

Figure 3.3: Schematic view of the LHC with its injectors. [48]

bunches). The high intensity of the proton bunches, however, results in multiple proton-proton collisions occurring during each crossing of proton bunches, an effect known as "pile-up". Thus, high luminosity was attained at the cost of substantially higher pile-up. The average number of interactions per bunch crossing was about 10 in 2011 and increased to about 20 in 2012. Therefore, we had to adjust our analysis techniques to mitigate the effects of the harsher pile-up environment.

3.2 The ATLAS detector

Description of the ATLAS experiment can be found in [58] and [59], for completeness we will quote some key aspects from this reference. ATLAS (A Toroidal LHC ApparatuS), located at "Point 1" (see [60] for the LHC layout), is one of two (ATLAS and CMS) general purpose detectors at the CERN Large Hadron Collider (LHC). As already stated,

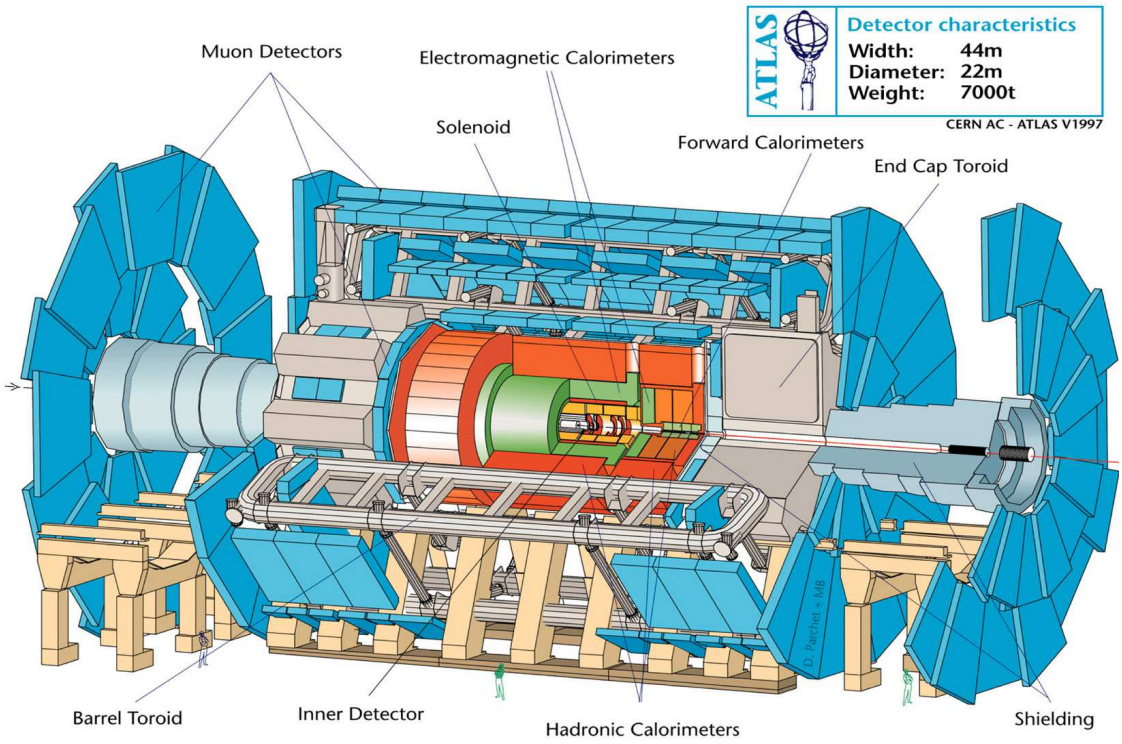

Figure 3.4: The ATLAS Detector. [61]

The LHC was designed to collide two 7 TeV proton beams at a luminosity of 10^{34} cm^{-2}s^{-1}. The design value for the bunch crossing time separation is 25 ns and at full luminosity there will be approximately 22 proton-proton collisions per bunch crossing.

3.2.1 Overview

The ATLAS detector is a cylinder with a total length of 44 m and a radius of 11 m and weighs approximately 7000 tons. It is built concentrically around the LHC beam pipe and installed in the interaction region 1 (IR 1 - see Figure 3.1). Figure 3.4 gives the overview of the experiment and its different sub-detectors. As any modern general-purpose detector in particle physics, ATLAS consists of the following main sub-detectors (see Fig 3.5):

1. **Inner Detector (ID)** - An inner tracking detector immersed in a solenoidal 2 T magnetic field, providing precision measurements of momenta of charged particles

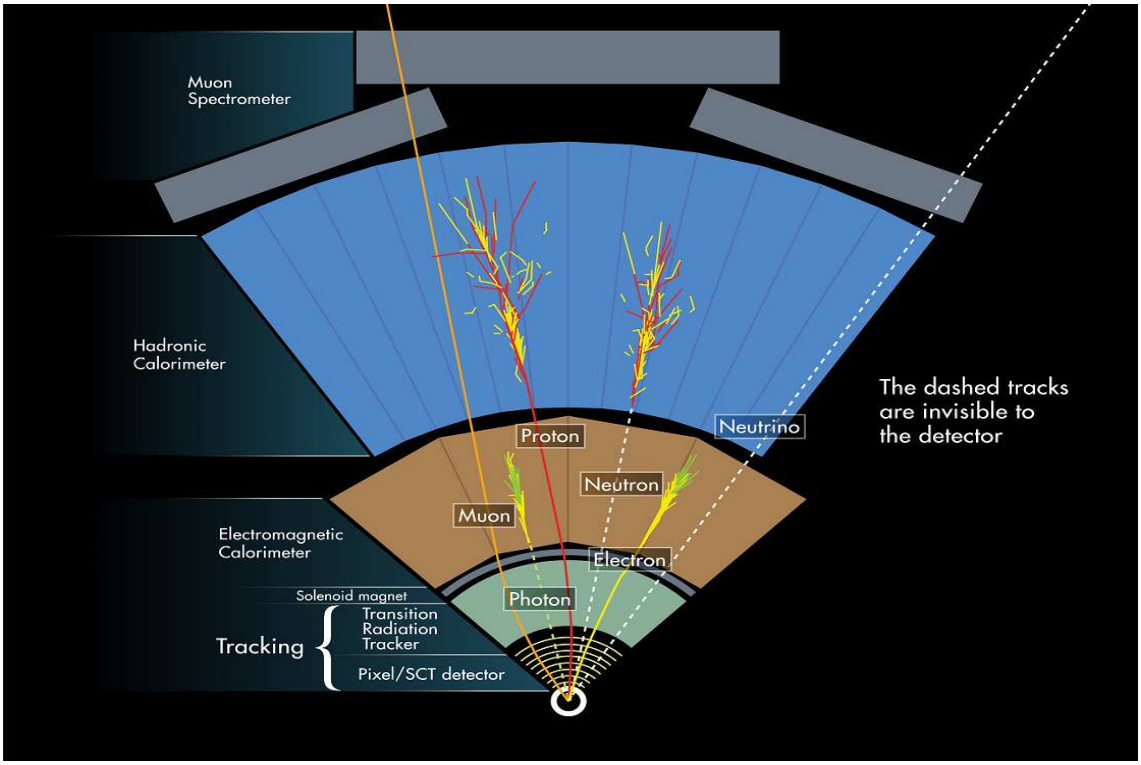

Figure 3.5: A computer generated image representing how ATLAS detects particles. [62]

that originate at (or near) the interaction point [63].

2. **Electromagnetic and Hadronic Calorimeters** - A calorimetry system sensitive to both electromagnetic and hadronic interactions. It provides an accurate measurement of the energy (transverse energy) of particles as well as the reasonable particle identification capabilities [64], [65]. In addition, the cylinder-shaped calorimeters (together with muon system described below) surrounding the interaction axis allow for measuring the missing-transverse momentum i.e. the total momentum in the plane transverse to beam direction, which is carried by the particles that evade detection (like neutrinos).

3. **Muon spectrometer.** The muon detector is immersed in a toroidal magnetic field of approximately 0.5 T (1 T - depending on the region), which provides muon identification and accurate momentum measurements in the wide range of muon momenta [66].

ATLAS detector distinguishes itself from other, similar experiments, in particular from CMS, in two important ways. First, in addition to silicon pixel and silicon strip sensors in the inner detector, ATLAS uses a straw-tube tracker with transition radiation detection capabilities for electron/pion discrimination [67], [68]. Second, the magnet system used for the muon spectrometer is composed of superconducting air-core toroids, rather than a second solenoidal field. An important part of any hadron collider experiment is the trigger system [69]. Composed of both hardware-based and software-based decision making elements, it selects only those collisions that are of potential interest for further analysis. This allows to reduce the initial event rate of about 20 MHz (at the bunch spacing of 50 ns) to about 300 Hz, which can be then saved to disk (tape) for further offline processing.

3.2.2 The ATLAS coordinate system

The ATLAS Coordinate System is a right-handed system with the x-axis pointing to the center of the LHC ring, the z-axis following the beam direction and the y-axis going upwards. In Point 1 , positive z points towards Point 8 with a slope of -1.23%. The azimuthal angle $\phi = 0$ corresponds to the positive x-axis and ϕ increases clock-wise looking into the positive z direction. ϕ is measured in the range $[-\pi, +\pi]$. The polar angle θ is measured from the positive z axis. Pseudorapidity, η, is defined as

$$\eta = -\log\left(\tan\left(\frac{\theta}{2}\right)\right), \tag{3.7}$$

With that, one can then define the transverse momentum (energy), p_T (E_T), as the momentum perpendicular to the LHC beam axis.

In case of massless particles, pseudorapidity is equal to true particle's rapidity (for ex-

ample, electrons can be safely considered as massless at the momentum range relevant to ATLAS detector). For massless particles, $d\eta$ is invariant under the Lorentz-boost transformation along the beam axis. At the same time, for particles moving perpendicular to z-axis, $d\eta$ is equal to $d\theta$. Next, the cone separation is defined as

$$\Delta R = \sqrt{(\Delta\phi)^2 + (\Delta\eta)^2} \tag{3.8}$$

Finally, the transverse momentum, p_T, is defined as a the momentum perpendicular to beam axis

$$p_T = \sqrt{(p_x)^2 + (p_y)^2} \tag{3.9}$$

3.2.3 The ATLAS magnet system

The fundamental choice of magnet configuration at ATLAS has driven the design of the rest of the detector. The magnet system comprises two main parts, cooled with liquid helium, with operating temperature of 4.5 K. The constituents are:

- **Thin superconducting solenoid (central solenoid)** - for momentum measurement in inner detector. Surrounding the inner-detector cavity, it provides momentum measurement of particles in the inner detector by bending their trajectories in the transverse plane in the magnetic field of about 2 T. The solenoid is constructed as a single-layer coil wound with a high-strength Al-stabilised NbTi superconductor. It stretches about 6 m along the z-axis and the inner at the radii of 2.46 m and 2.56 m, respectively.

- **Superconducting toroid** - for momentum measurement in the muon spectrometer.

In ATLAS there are three large superconducting toroids, one barrel and two end-caps, each with eight coils. Arranged with an eight-fold azimuthal symmetry around the calorimeters, they provide the momentum measurement of muons by bending their trajectories in the η-direction. The toroids feature a magnetic field of approximately 0.5 T in the barrel region and 1 T in the end-caps. The conductor and coil-winding technology is the same in the barrel and end-cap toroids. It is based on winding a pure Al-stabilised Nb/Ti/Cu conductor into pancake-shaped coils, followed by vacuum impregnation. The inner and outer diameters of the barrel toroid magnet system are 9.4 m and 20.1 m, respectively, and the magnet system spans 25.3 m along the beam direction.

3.2.4 The ATLAS inner detector

The inner detector (ID), or similarly - inner tracker, consists of three subsystems, two of them are silicon-based tracking detectors, and the third one is based on transition radiation, as shown in Figure 3.6. They are dedicated mostly to measuring the momentum of charged particles (in the transverse-momentum range from 0.1 GeV to several TeV) and determining the location of primary and secondary vertices, via the hits that are produced by charged particles traversing different stations of these sub-detectors (see Figure 3.7). Each subsystem is composed of a barrel and two end-caps (in the forward and backward regions). The inner detector subsystems are:

- **Pixel Detector (Pixels)**. This subsystem is composed of silicon pixel sensors, placed closest to the interaction point with a distance of 50.5 mm from the center of the beam pipe. This detector provides the most accurate position measurements in ATLAS. It has three stations with the outermost one at the distance of 122.5

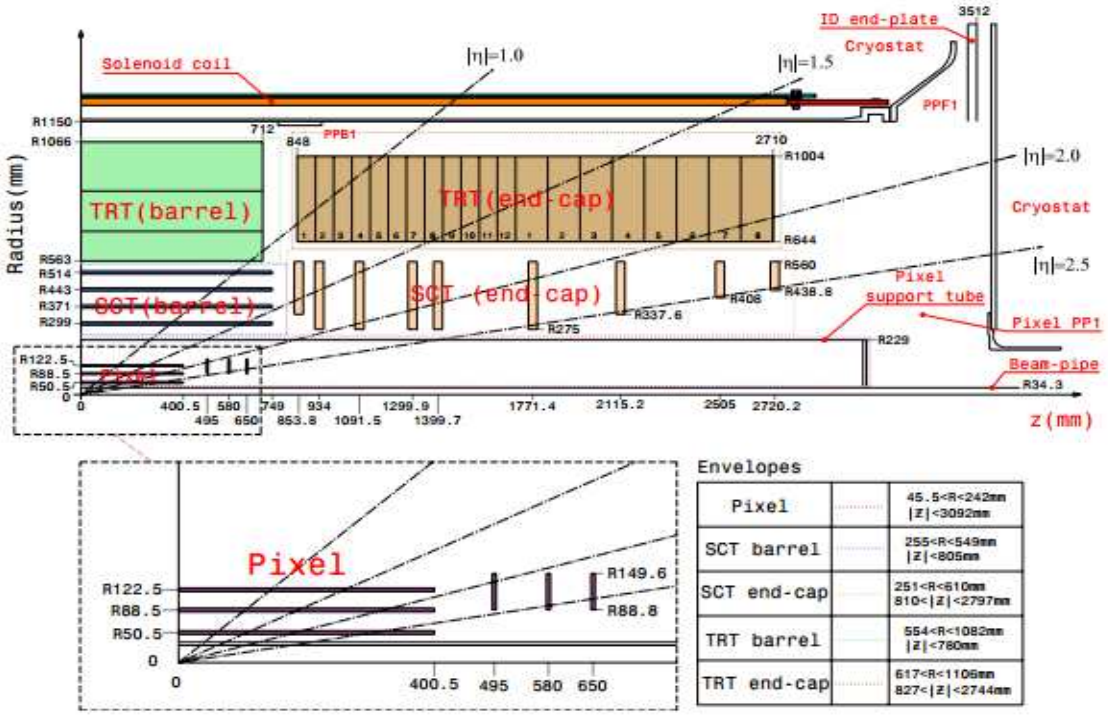

Figure 3.6: Plan view of a quarter-section of the ATLAS inner detector showing each of the major detector elements with its active dimensions and envelopes. [38]

mm from the beam axis. Typically, all tracks in the acceptance of the Pixels get three hits, each with an intrinsic accuracy of $R\Delta\phi \times \Delta z$= 10 × 115 μm in the barrel region [38], [70]].

- **Semi-Conductor Tracker (SCT)**. This subsystem placed outside of the pixels is a silicon microstrip detector. The Semiconductor Tracker is also based on silicon technology, but in the form of strips mounted with a 40 mrad stereo angle. It has four stations in the barrel region with innermost and outermost radii of 299 and 514 mm respectively, providing up to eight hits per tracks. This forms four space-point measurements, each with an intrinsic accuracy in the barrel region of $R\Delta\phi \times \Delta z = 17$ × 580 μm. In the SCT, reconstructed hits are expected whenever a sensor is crossed by a charged particle, regardless of charge, and there is no risk of hits being lost due to saturation [38], [71].

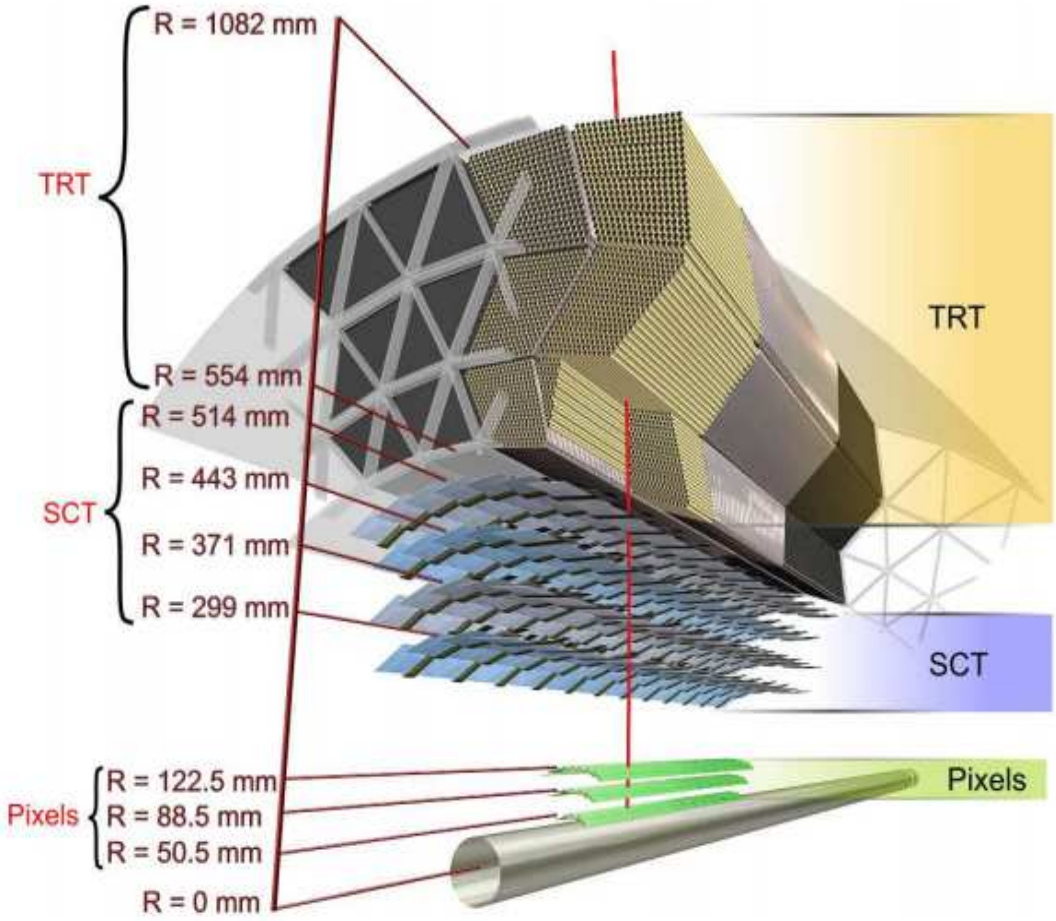

Figure 3.7: Drawing showing the sensors and structural elements traversed by a charged track of 10 GeV p_T in the barrel inner detector ($\eta = 0.3$). The track traverses successively the beryllium beam-pipe, the three cylindrical silicon-pixel layers with individual sensor elements of 50×400 μm^2, the four cylindrical double layers (one axial and one with a stereo angle of 40 mrad) of barrel silicon-microstrip sensors (SCT) of pitch 80 μm, and approximately 36 axial straws of 4 mm diameter contained in the barrel transition-radiation tracker modules within their support structure. [38]

- **Transition Radiation Tracker (TRT)**. Placed at the outermost radii of inner detector, the TRT is composed of many layers of gaseous straw tube elements filled with Xe + CO_2 + O_2 gas mixture, interleaved with transition radiation material. Low-energy transition radiation (TR) photons are absorbed in the Xe-based gas mixture, and yield much larger signal amplitudes than minimum-ionising charged particles. With an average of 36 hits per track, it provides continuous tracking to enhance the pattern recognition of tracks. The TRT straws only provide measurements in the bending plane, with an intrinsic accuracy of $R\Delta\phi = 130$ μm, and no measurements can be made along the straw direction [38], [72].

Silicon-based detectors are used in modern state-of-the-art general-purpose particle detectors for their excellent position resolution, which is typically on the order of microns. The sensors are thin pieces of high-purity doped silicon, which produce electron-hole pairs when traversed by an ionizing particle. An electric field is applied to the sensor to prevent the pairs from recombining, and the subsequent drift and capture of the free charge carriers produces a current pulse that is read out by analog electronics. In ATLAS, there are two silicon-based sub-detectors: An important feature of TRT detector is its capability of identifying particle types through benefiting from the transition radiation mechanism, which results in higher-amplitude signals for particles at high $\beta = \frac{v}{c}$. In the front-end electronics of the TRT, the measured signals are discriminated against two thresholds, classifying the hits as low-threshold (LT) or high-threshold (HT) hits. This allows to discriminate between electrons and charged hadrons [67], [68].

3.2.5 The ATLAS calorimeters

ATLAS has two types of calorimeters - electromagnetic (EM) and hadronic, sensitive to electromagnetic and strong interactions of charged particles with matter. The primary purpose of the calorimeter system is to stop all particles (except muons and neutrinos) emanating from the interaction point and thereby measure their energy and position. These calorimeters span the range $|\eta| < 4.9$ with full $\phi-$symmetry and coverage around the beam axis.

While hadronic calorimeters predominantly measure the energy of hadrons via the strong interaction with the heavy nuclei of the absorbing medium, the electromagnetic calorimeters measure the energy of electrons and photons and contribute to measuring the energy of hadrons in jets via the mechanisms of bremsstrahlung radiation of photons and production of electron-positron pairs (see also Ref. [73]). The overall sketch of ATLAS calorimetry is shown in Figure 3.8 and the η-coverage of each sub-system is given in Table 3.1.

All calorimeters at ATLAS are of the sampling type, i.e. each calorimeter includes, first, dense absorber material (lead, iron, copper or tungsten) to fully absorb incident particles and, second, active material (liquid-argon or plastic scintillations) to produce an output signal proportional to the input energy. The absorbing medium is interleaved with detecting material ("sandwich" design).

Electromagnetic calorimeters

The Electromagnetic calorimeter uses liquid argon as the active detector and lead as the absorber material. When a photon enters the detector, it interacts with the lead plates and produces electron-positron pair.

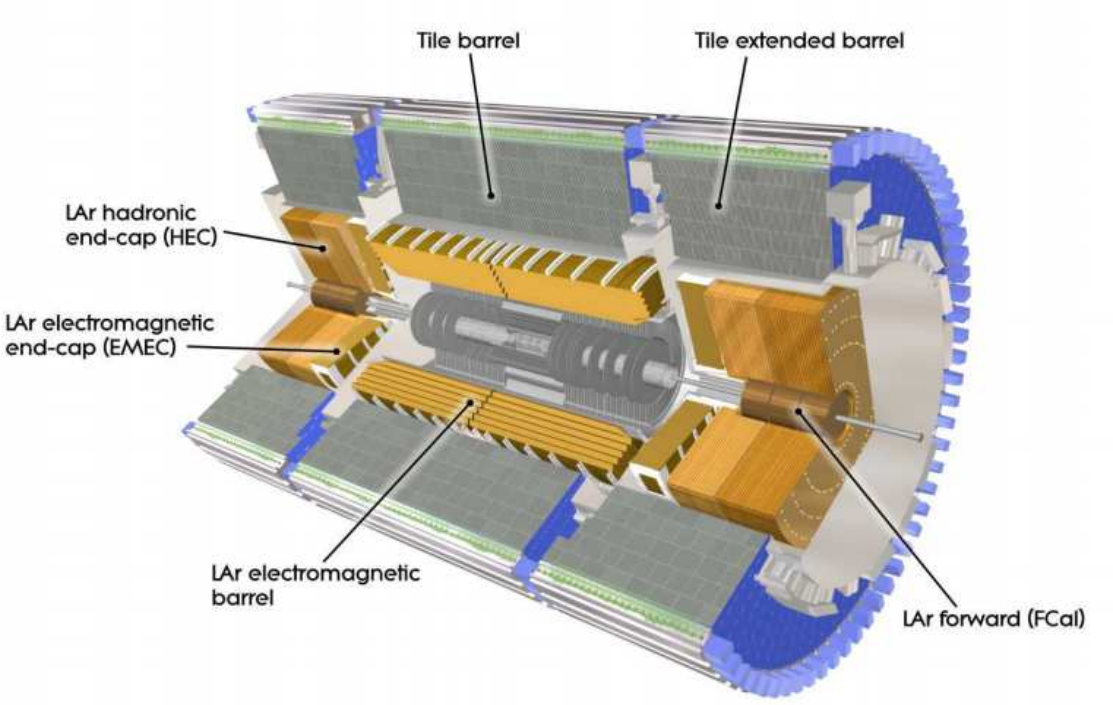

Figure 3.8: Cut-away view of the ATLAS calorimeter system. [38]

The electron and positron continue to interact with the material in the calorimeter, producing Bremsstrahlung photons, which in turn again produce electron-positron pairs, creating a "shower" of electromagnetic activity (see Figure 3.9 - left). These electrons and positrons pass through the active material (liquid argon) and ionize the argon atoms, releasing ionization electrons which are collected as a current by applying an electric field of about 10 kV/cm (see also Ref. [74]). The visible energy is scaled by the sampling fraction to obtain the true deposited energy in both the active material and the absorber. An electron entering the liquid-argon (LAr) calorimeter will undergo the same chain reaction as a photon.

High granularity LAr electromagnetic sampling calorimeters, with excellent energy and position resolution, cover the pseudorapidity range $|\eta| < 3.2$ (the barrel covers $|\eta| < 1.475$ and the two end-caps cover $1.375 < |\eta| < 3.2$).

The electromagnetic calorimeters share the same vacuum vessel with central solenoid

	Barrel	End-cap
EM calorimetere		
	Number of layers and η coverage	
Presampler	1 ; $\|\eta\| < 1.52$	1 ; $1.5 < \|\eta\| < 1.8$
Calorimeter	3 ; $\|\eta\| < 1.35$ 2 ; $1.35 < \|\eta\| < 1.475$	2 ; $1.375 < \|\eta\| < 1.$ 3 ; $1.5 < \|\eta\| < 2.5$ 2 ; $2.5 < \|\eta\| < 3.2$
	Granularity $\Delta\eta \times \Delta\phi$ versus η	
Presampler	0.025×0.1 ; $\|\eta\| < 1{:}52$	0.025×0.1 ; $1.5 < \|\eta\| < 1.8$
Calorimeter 1st layer	$0.025/8 \times 0.1$ $\|\eta\| < 1.40$ 0.025×0.025 ; $1.40 < \|\eta\| < 1.475$	0.050×0.1 ; $1.375 < \|\eta\| < 1.425$ 0.025×0.1 ; $1.425 < \|\eta\| < 1.5$ $0.025/8 \times 0.1$; $1.5 < \|\eta\| < 1.8$ $0.025/6 \times 0.1$; $1.8 < \|\eta\| < 2.0$ $0.025/4 \times 0.1$; $2.0 < \|\eta\| < 2.4$ 0.025×0.1 ; $2.4 < \|\eta\| < 2.5$ 0.1×0.1 ; $2.5 < \|\eta\| < 3.2$
Calorimeter 2nd layer	0.025×0.025 ; $\eta < 1.40$ 0.075×0.025 ; $1.40 < \|\eta\| < 1.475$	0.050×0.025 ; $1.375 < \|\eta\| < 1.425$ 0.025×0.025 ; $1.425 < \|\eta\| < 2.5$ 0.1×0.1 ; $2.5 < \eta < 3.2$
Calorimeter 3rd layer	0.050×0.025 ; $\eta < 1.35$	0.050×0.025 ; $1.5 < \eta < 2.5$
	Number of readout channels	
Presampler	7808	1536 (both sides)
Calorimeter	101760	62208 (both sides)
LAr hadronic end-cap		
η coverage		$1.5 < \eta < 3.2$
Number of layers		4
Granularity $\Delta\eta \times \Delta\phi$		0.1×0.1 ; $1.5 < \|\eta\| < 2.5$ 0.2×0.2 ; $2.5 < \|\eta\| < 3.2$
Readout channels		5632 (both sides)
	textbfLAr forward calorimeter	
η coverage		$3.1 < \|\eta\| < 4.9$
Number of layers		3
Granularity $\Delta x \times \Delta y$ (cm)		FCal1: 3.0×2.6 ; $3.15 < \|\eta\| < 4.30$ FCal1: 4 $\times$ finer $3.10 < \|\eta\| < 3.15$ $4.30 < \|\eta\| < 4.83$ FCal2:3.3×4.2 ; $3.24 < \|\eta\| < 4.50$ FCal2: 4 $\times$finer $3.20 < \|\eta\| < 3.24$ $4.50 < \|\eta\| < 4{:}81$ FCal3:5.4×4.7 $3.32 < \|\eta\| < 4.60$ FCal3: $4 \times 3.29 < \|\eta\| < 3.32$ $4.60 < \|\eta\| < 4.75$
Readout channels		3524 (both sides)
Scintillator tile calorimeter		
	Barrel	Extended barrel
$\|\eta\|$ coverage	$\|\eta\| < 1.0$	$0.8 < \|\eta\| < 1.7$
Number of layers	3	3
Granularity $\Delta\eta \times \Delta\phi$	0.1×0.1	0.1×0.1
Last layer	0.2×0.1	0.2×0.1
Readout channels	5760	4092 (both sides)

Table 3.1: *Main parameters of the calorimeter system, table from [59]*

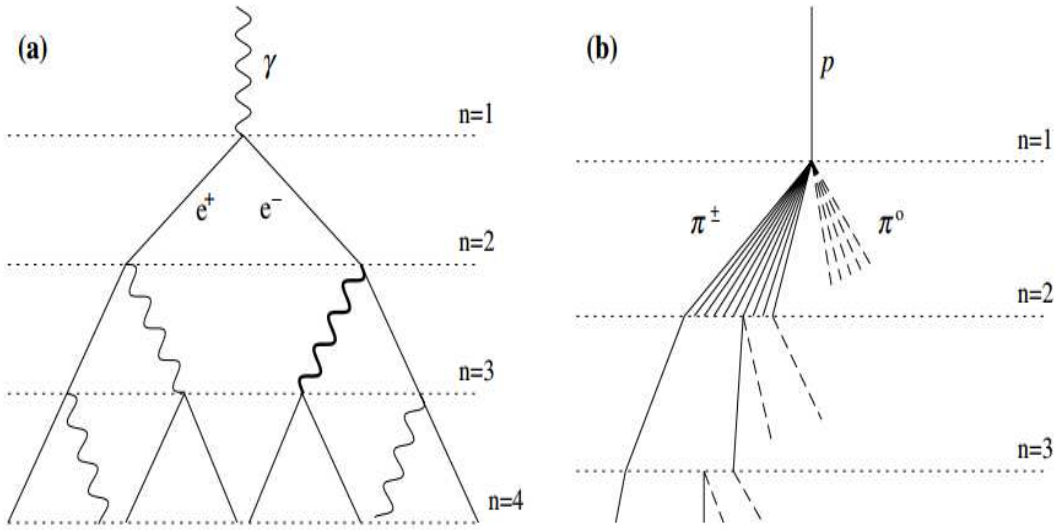

Figure 3.9: Schematic views of (a) an electromagnetic cascade and (b) a hadronic shower. In the hadron shower, dashed lines indicate neutral pions which do not re-interact, but quickly decay, yielding electromagnetic subshowers (not shown). Not all pion lines are shown after the n = 2 level. Neither diagram is to scale. [75]

and are divided into a barrel part and two end-cap components, each housed in their own cryostat, as described below

- **Barrel LAr EM calorimeter (EMB).** The barrel EM calorimeter consists of two identical half-barrels, separated by a small gap (4 mm) at z=0.

- **End-cap LAr EM calorimeter (EMEC).** Each end-cap EM calorimeter is mechanically divided into two coaxial wheels: an outer wheel covering the region 1.375< $|\eta|$ < 2.5, and an inner wheel covering the region 2.5 < $|\eta|$ <3.2.

The total thickness of EM calorimeter is more than 24 radiation lengths (X_0) in the barrel and above 26 X_0[1] in the endcaps. Over the region devoted to precision physics ($|\eta|$ <2.5), the EM calorimeter is segmented in three sections in depth. For the end-cap inner wheel, the calorimeter is segmented in two sections in depth and has a coarser lateral

[1]Electromagnetic radiation length X_0 (nuclear interaction length λ) of the material defines the mean distance over which the the energy of electron (hadron) is reduced by a factor of 1/e as it pass through that material

granularity than for the rest of the acceptance. In the region of $|\eta|$ <1.8, a presampler detector is used to correct for the energy lost by electrons and photons upstream of the calorimeter. The presampler consists of an active LAr layer of thickness 1.1 cm (0.5 cm) in the barrel (endcap) region. The $\eta - \phi$ resolution of EM calorimeter varies depending on the η-region and calorimeter layer and is usually is of the order of 0.025×0.025 (in the second layer of barrel EM calorimeter)

Hadronic calorimeters

The mechanism of hadron interactions with matter differs from that of electrons and photons. Hadrons typically loose their energy through inelastic collisions with the nuclei of absorbing material (see Figure 3.9 - right). However, the principle of operation of hadronic calorimeters is essentially the similar to the electromagnetic one, i.e. charged particles are produced in the absorber medium and detected in the active material (plastic scintillator or liquid argon) [76]. The main difference is that the nuclear interaction length λ is larger than electromagnetic radiation length X_0. Hence the absorbing part of hadronic calorimeter needs to be denser (deeper). It should be noted also that a sizeable fraction of the energy deposited in a hadronic shower is electromagnetic - from production and decay of neutral pions ($\pi^0 \to \gamma\gamma$). The ATLAS hadronic calorimeter system comprises the following parts:

The hadronic calorimetry in the range $|\eta| < 1.7$ is provided by a scintillating-tile calorimeter, which is separated into a large barrel ($|\eta| < 1.0$) and two smaller extended barrel cylinders, one on either side of the central barrel ($0.8 < |\eta| < 1.7$). In the end-caps ($|\eta| > 1.5$), LAr hadronic calorimeters match the outer $|\eta|$ limits of the end-cap electromagnetic calorimeters. The LAr forward calorimeters provide both electromagnetic and

hadronic energy measurements, and extend the coverage to $|\eta| < 4.9$. The granularity of the hadronic calorimeter is varying between $\Delta\eta \times \Delta\phi = 0.1 \times 0.1$ for the barrel Scintillator tile calorimeter and the LAr hadronic end-cap, up to $\Delta x \times \Delta y = 5.4 \times 4.7$ cm in the LAr forward calorimeter.

- **Tile hadronic calorimeter (TileCal).** It uses steel as the absorber and scintillating tiles as the active material. The tile calorimeter is placed directly outside the EM calorimeter envelope. Its barrel covers the region $|\eta| < 1.0$, and its two extended barrels the range $0.8 < |\eta| < 1.7$. The total detector thickness at the outer edge of the tile-instrumented region is 9.7 λ at η =0.

- **LAr end-cap hadronic calorimeter (HEC).** This uses copper as an absorber material. The copper plates are interleaved with LAr gaps, providing the active medium for this calorimeter. It consists of two independent wheels per end-cap, located directly behind the end-cap electromagnetic calorimeter and sharing the same LAr cryostats.

- **Forward LAr hadronic calorimeter (FCal).** FCal consists of three modules in each end-cap: the first one uses copper as the absorber and is optimized for electromagnetic measurements, while the other two, made of tungsten, measure predominantly the energy of hadronic interactions. Each module consists of a metal matrix, with regularly spaced longitudinal channels filled with the electrode structure consisting of concentric rods and tubes parallel to the beam axis. The LAr in the gap between the rod and the tube is the sensitive medium. The depth of FCal is approximately 10 λ and, similarly to EMEC and HEC, it is integrated into the end-cap cryostats.

3.2.6 The ATLAS muon spectrometer

The Muon spectrometer consists of one barrel and two endcap air-core toroidal magnets, each consisting of eight superconducting coils arranged symmetrically in azimuth around the calorimeter. Three layers of precision tracking chambers, consisting of drift tubes and cathode strip chambers, allow precise Muon momentum measurement up to $|\eta| = 2.7$. Resistive plate and thin-gap chambers provide muon triggering capability up to $|\eta| = 2.4$.

Precision muon detectors

The precision-tracking muon detectors are MDT and CSC chambers. MDT chambers consist of three to eight layers of drift tubes, operated at an absolute pressure of 3 bar, which achieve an average resolution of 80 μm per tube, or about 35 μm per chamber. The overall layout of the MDTs is projective: the layer dimensions and the chamber sizes increase in proportion of their distance from the interaction point. The CSC detectors are multiwire proportional chambers with cathode planes segmented into strips in orthogonal directions. The purpose of the precision-tracking chambers is to determine the coordinate of the track in the bending plane (η). The CSC chambers provide also the ϕ coordinate, while there is no measurement of ϕ performed in MDT detectors. After matching of the MDT and trigger chamber hits in the bending plane, the trigger chambers coordinate in the non-bending plane is adopted as the second coordinate of the MDT measurement. This method assumes that in any MDT/trigger chamber pair a maximum of one track per event be present, since with two or more tracks the η and ϕ hits cannot be combined in an unambiguous way. Simulations have shown that the probability of a track in the muon spectrometer with $p_T > 6$ GeV is about 6×10^{-3} per beam-crossing, corresponding to

about 1.5×10^{-5} per chamber [38]. Assuming uncorrelated tracks, this leads to a negligible probability to find more than one track in any MDT/trigger chamber pair. When correlated close-by muon tracks do occur, caused for example by two-body-decays of low-mass particles, the ambiguity in η and ϕ-assignment is resolved by matching the muon track candidates with tracks from the inner detector

Trigger muon detectors

An essential design criterion of the muon system was the capability to trigger on muon tracks. The precision-tracking chambers have therefore been complemented by a system of fast trigger chambers capable of delivering track information within a few tens of nanoseconds after the passage of the particle. Both chamber types deliver signals with a spread of 15 - 25 ns, thus providing the ability to tag the beam-crossing. The trigger chambers measure both coordinates of the track, one in the bending (η) plane and one in the non-bending (ϕ) plane.

The trigger system covers the pseudorapidity range $|\eta|$ <2.4. Resistive Plate Chambers (RPC) are used in the barrel and Thin Gap Chambers (TGC) [2] in the end-cap regions. Apart from triggering, these detectors serve also for providing bunch-crossing identification, and for measuring the muon coordinate in the direction orthogonal to that determined by the precision-tracking chambers (ϕ-coordinate).

Alignment of muon detectors

[2]TGC are Israeli technology built in collaboration of groups from Israel, Japan and China. Build in Israel (at Weizmann Institute) and China, and were tested at the cosmic testbenches at my physics group within Tel Aviv University and at the Technion.

The overall performance over the large areas involved, particularly at the highest momenta, depends on the alignment of the muon chambers with respect to each other and with respect to the overall detector. The accuracy of the stand-alone muon momentum measurement (without employing track information from the inner detector) necessitates a precision of 30 μm on the relative alignment of chambers both within each projective tower and between consecutive layers in immediately adjacent towers. The accuracy required for the relative positioning of non-adjacent towers to obtain adequate mass resolution for multi-muon final states, lies in the few millimetre range [38].

The stringent requirements on the relative alignment of the muon chamber layers are met by the combination of precision mechanical-assembly techniques and optical alignment systems both within and between muon chambers, as reported in Refs. [77], [78].

3.2.7 The ATLAS trigger and data acquisition system

At nominal LHC running, bunches of protons collide inside ATLAS every 25 ns (75-50 ns in 2011 and 50 ns in 2012 data-taking periods). Neither the data acquisition system nor the resources for doing offline analysis are capable of handling such amounts of data. Therefore, a trigger system is required to select only the most interesting events to be written to disk and analyzed further offline. At ATLAS, a three-level trigger system [79] serves this purpose.

The general scheme of ATLAS trigger system is shown in Figure 3.10. The trigger system is composed of three consecutive levels. The level-1 trigger is based on custom-built hardware that processes coarse detector information to reduce the event rate to a design value of at most 75 kHz. This is followed by two software-based trigger levels, level-2 and

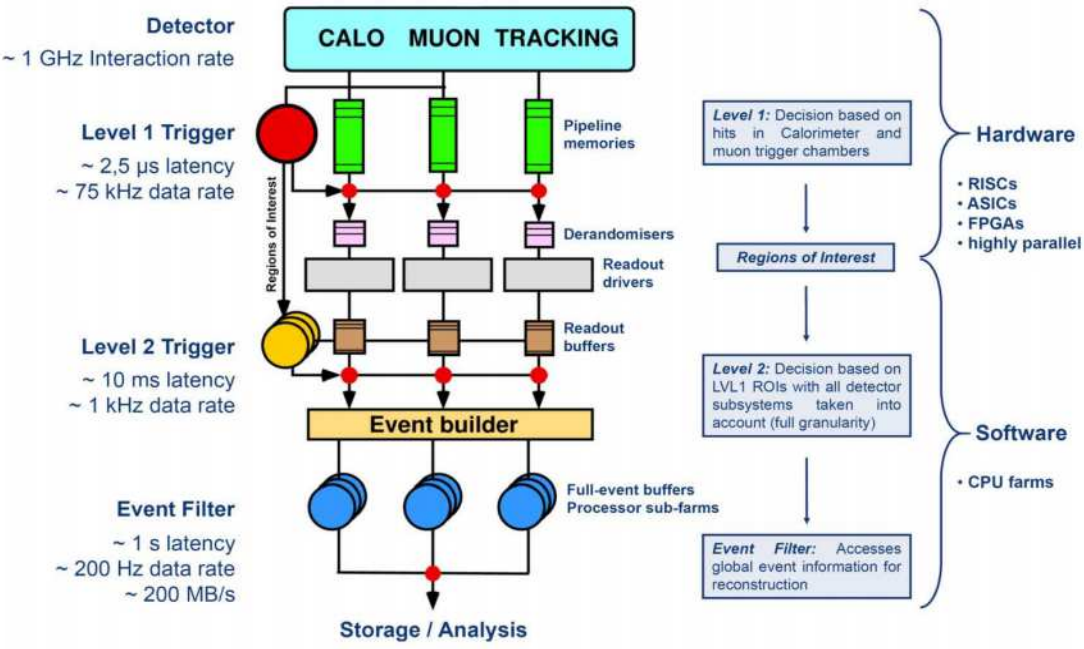

Figure 3.10: Block diagram of the trigger/DAQ system. On the left side the typical collision and the data equivalent at the different stages of triggering are shown, while in the middle section the different components of the trigger system are shown schematically [38]. The right side of the graphic gives a short summary of the operations and the technologies used at the respective level. Fig from [80]

the event filter, which together reduce the event rate to a few hundred Hz which is recorded for analysis.

Level 1 Trigger (L1)

The L1 trigger searches for high transverse-momentum muons, electrons, photons, jets, and τ -leptons decaying into hadrons, as well as large missing and total transverse momentum (see Figure 3.11). Its selection is based on information from a calorimeter and muon detectors. High transverse-momentum muons are identified using trigger chambers in the barrel and end-cap regions of the spectrometer. Calorimeter selections are based on reduced-granularity information from all the calorimeters. Results from the L1 muon and calorimeter triggers are processed by the central trigger processor, which implements a trig-

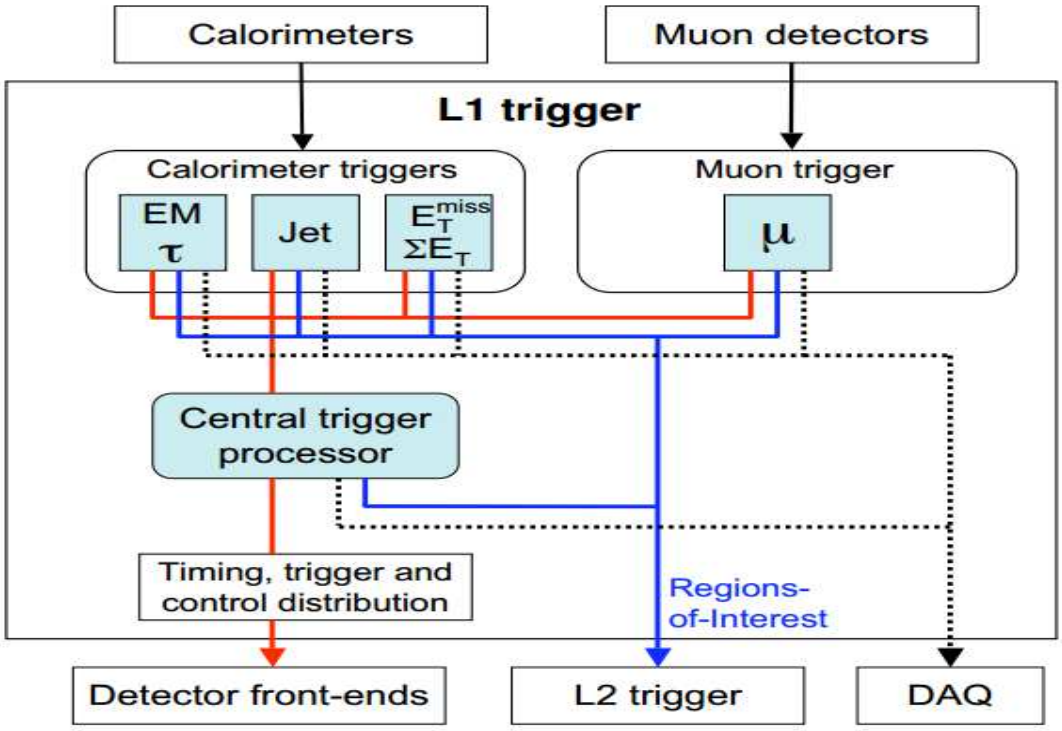

Figure 3.11: Block diagram of the L1 trigger. The overall L1 accept decision is made by the central trigger processor, taking input from calorimeter and muon trigger results. The paths to the detector front-ends, L2 trigger, and data acquisition system are shown from left to right in red, blue and black, respectively. [38]

ger "menu" made up of combinations of trigger selections. In each event, the L1 trigger also defines one or more Regions-of-Interest (RoI), i.e. the geographical coordinates in η and ϕ, of those regions within the detector where its selection process has identified interesting features. The RoI data include information on the type of feature identified and the criteria passed, e.g. a threshold. This information is subsequently used by the high-level trigger.

High-level trigger (HLT)

The L2 selection is seeded by the RoI information provided by the L1 trigger over a dedicated data path. L2 selections use, at full granularity and precision, all the available detector data within the RoI's. The L2 menus are designed to reduce the trigger rate to

approximately 3.5 kHz, with an event processing time of about 40 ms, averaged over all events. The final stage of the event selection is carried out by the event filter,

Trigger menus and data streams

Data for events selected by the trigger system are written to inclusive data streams based on the trigger type. There are four primary physics streams, Egamma (electrons and photons), Muons, JetTauEtmiss (jets, b-jets, τ -leptons, and high missing transverse momentum), MinBias (strong interactions with small transverse momentum transfer), plus several additional calibration streams. Some overlap exists between streams, for example, the highest overlap is observed between Egamma and JetTauEtmiss streams - up to 15% [81]. The highest rates of recorded events are in the JetTauEtmiss, Egamma and Muons streams.

The trigger system is configured via a trigger menu which defines trigger chains - a set of selection criteria that start from a L1 trigger and specify a sequence of reconstruction and selection steps for the specific trigger signatures required in the trigger chain. A trigger chain is often referred to simply as a trigger. Some triggers are prescaled - that is, only some fraction of events fired by the trigger are eventually recorded to permanent data storages.

Readout drivers and data acquisition system

The data are recorded to permanent storages as follows. After an event is accepted by the L1 trigger, the data from the pipe-lines are transferred off the detector to the readout

drivers (ROD's). Digitised signals are formatted as RAW data prior to being transferred to the data-acquisition (DAQ) system. The first stage of the DAQ, the readout system, receives and temporarily stores the data in local buffers. It is subsequently solicited by the L2 trigger for the event data associated to RoI's. Those events selected by the L2 trigger are then transferred to the event-building system and subsequently to the event filter for final selection. Events selected by the event filter are moved to permanent storage at the CERN computing center and another (so-called Tier-1) center in the worldwide computing GRID (WLCG). There are 10 Tier-1 centers total.

Chapter 4

Data analysis

The second part of my Ph.d was to conduct a search for new particles decaying into a $t\bar{t}$ pairs within the ATLAS detector. The analysis work was done in a collaborative effort with several groups within the ATLAS Exotics Physics group.

4.1 Benchmark Models

While $t\bar{t}$ resonance searches are relevant for many extension of the SM that leads to an enhanced top quark pair production rate at large $t\bar{t}$ invariant mass, it was agreed in ATLAS to interpret the result within two specific benchmark models: The leptophobic topcolor Z' boson [82] represents an example of a narrow resonance, where the experimental resolution dominates the width of the reconstructed mass peak. The Tevatron searches have set a 95% confidence level (CL) limit on the mass of the leptophobic topcolor Z' boson [83] at $m_{Z'}$ $>$ 900 GeV [12]. The second benchmark model envisages a Kaluza-Klein (KK) excitation of the gluon g_{KK}, as predicted in models with warped extra dimensions [84], [85]. For the choice of parameters of Lillie et al. [86] used here, the KK gluon manifests itself as a

relatively broad resonance ($\Gamma\ m = 15.3\%$) with a branching fraction BR ($g_{KK} \to t\bar{t}$) = 92.5%.

4.2 Physics objects

This analysis makes use of jet, electron, muon and missing transverse momentum objects reconstructed using the detector. Furthermore, b-tagging information is used for jets

4.2.1 Jets

Two types of jets are used in this analysis:

- **small-R** jets are reconstructed using the inclusive anti-kt jet algorithm [87], as implemented in Fastjet 2.4.2p5 [88], with radius parameter R=0.4 and using the *E-scheme* for cluster recombination. Locally calibrated topoclusters are used as inputs to the algorithm. The calibration scheme used for these jets, employing pile-up subtraction and based on *in-situ* methods, is described in detail in Ref. [89].

- **large-R** jets are reconstructed using the inclusive anti-kt jet algorithm, as implemented in Fastjet 2.4.2p5, with radius parameter R=1.0 and using the *E-scheme* for cluster recombination. Jet trimming [90] is applied, with parameters $f_{cut} = 0.05$, and Rsub = 0.3, to mitigate the effects of in- time pile-up. Locally calibrated topoclusters are used as inputs to the algorithm. The uncertainties on the jet calibrations are derived using the same methodology as was used before the the ATLAS 7 TeV data analysis [91] but with values updated using 2012 data.

A cut on the Jet vertex Fraction[1] ($|JVF| > 0.5$) is used to reduce the effect of in-time

[1]JVF is Jet Vertex Fraction and is the fraction of tracks associated with the jet that come from the

pile-up. This does not form part of the jet object definitions per-se, but is used in muon-jet overlap removal criteria as discussed in section 4.2.3. No b-tagging of large-R jets is done, b-tagging is applied to small-R jets, using the MV1 [92] algorithm. The working point chosen is the 70% working point, corresponding to a cut on the MV1 weight > 0.772.

4.2.2 Muons

Muons are selected according to recommendations of the ATLAS Muon Combined Performance (MCP) group [93] using the so called muid algorithm as follows:

- Muons are required to have a reconstructed track both in the Muon detector and in the Inner Detector
- The pseudorapidity must lie with the range $|\eta| < 2.5$
- The transverse momentum, p_T , must be greater than 25 GeV
- The tracks must pass the MCP ID track quality cuts
- The longitudinal impact parameter relative to the primary vertex must be less than 2 mm

Muons are furthermore, required to be isolated as discussed in Ref. [89].

4.2.3 Overlap removal between jets, muons and electrons

Since the physics objects are generally built out of calorimeter deposits and associated tracks, some overlap of physics objects is possible. Overlap removal is achieved with the following procedure:

primary vertex, it is defined and explained in section 4.3.1

- Remove muons with ΔR(l, j) < 0.1 to a small-R jet with $p_T > 25$ GeV and $|JVF|$ > 0.5. These muons are likely to come from non-prompt sources.

- Remove any jet that uses an electron cluster: the nearest (smallest distance in the η - Φ plane, ΔR(l, j)) positive-energy jet to an electron object is removed, so long as it lies within ΔR(l, j) < 0.2 .

- Remove electrons with ΔR(l, j) < 0.4 to any remaining small-R jet with $p_T > 25$ GeV.

Note that the muon cut is looser than in other ATLAS top analyses. This is because high-mass signal events can give leptons from W decays very close to the b-jet. Reducing the cut for electrons was not yet done because in that case the nearby electron can bias the jet kinematics and also because electron ID performance is not well-understood in the presence of close-by jets.

4.2.4 Missing transverse momentum

The MET RefFinal AntiKt4LCTopoJets tightpp definition is used for the missing transverse momentum, E_T^{miss}. This is computed using calibrated cells belonging to identified high-p_T objects in the following order: electrons, photons, jets and muons (denoted as RefEle, RefGamma, RefJet, RefMuon terms) by replacing the initial cell energies with the modified refined calibration. Cells belonging to multiple objects are resolved using the first association in order to avoid double counting. Low-p_T jets ($10 < p_T < 20$ GeV) are grouped into the SoftJet term. The total muon contribution to the final E_T^{miss} calibration is the sum of the RefMuon term, which uses cells of non-isolated muons, and E_T^{miss} calculated from combined muon tracks and the cells of isolated muons (MuonTotal term). All remaining

cells not belonging to any high-p_T objects are also included separately (CellOut term). The final calibrated E_T^{miss} is denoted as RefFinal. RefEle uses cells with cluster corrections at the EM scale. RefJet term uses cells calibrated using the locally calibrated topo clusters (LC+Jet Energy Scale (JES)) scheme. SoftJet term is calibrated using the local hadron (LocHad) based scheme. The SofJets and CellOut terms are collectively referred to as SoftTerms. The total sum is then:

$$E_{x,y}^{miss} = E_{x,y}^{RefElec} + E_{x,y}^{RefPhoton} + E_{x,y}^{RefJet} + E_{x,y}^{RefSoftJet} + E_{x,y}^{RefMuon} + E_{x,y}^{CellOut}, \quad (4.1)$$

and the magnitude is given by

$$E_{x,y}^{miss} = \sqrt{(E_x^{miss})^2 + \left(E_y^{miss}\right)^2}. \quad (4.2)$$

4.3 Event reconstruction

In this section the reconstruction of the $t\bar{t}$ invariant mass is discussed, for the resolved and boosted selections. For both the resolved and the boosted selections, the longitudinal component of the neutrino momentum, p_z, is computed by imposing an on-shell W mass constraint on the lepton + E_T^{miss} system, assuming that the majority of the missing transverse momentum stems from the neutrino and that the neutrino and the charged lepton are the decay products of the W boson. This yields a quadratic equation when solving for the neutrino p_z component. If only one real solution to p_z exists, this is used. If two real solutions exist, the solution with the smallest $|p_z|$ is chosen or both are tested, depending on the reconstruction algorithm. In events where no real solution is found, the E_T^{miss} is

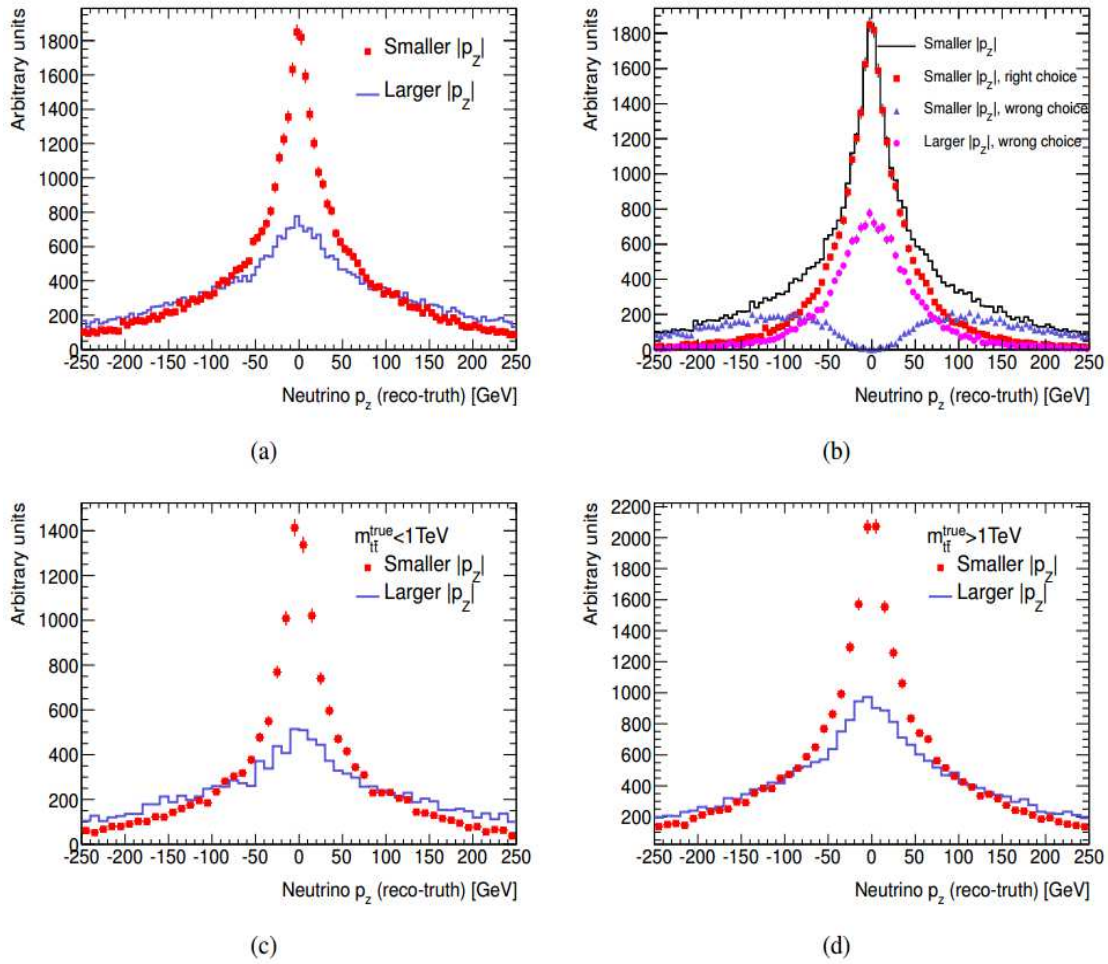

Figure 4.1: Neutrino momentum resolution from the imposition of the W boson mass constraint: a) comparison of the p_z resolution for the smaller and larger solution in the case of two solutions to the quadratic equation. Tails in a) come from events where the solution with the smallest $|p_z|$ is not the optimal choice (i.e. the solution with the largest $|p_z|$ was closest to the true neutrino's p_z) as shown in b). c-d) demonstrate the validity of the choice does not depend on the invariant mass of the $t\bar{t}$ system

rescaled and rotated, applying the minimum variation necessary to find exactly one real solution [94]. This procedure is justified since mis-measurement of the missing transverse momentum is the most likely explanation for a lack of solution to the p_z equation, assuming that the lepton indeed comes from a W decay. The neutrino momentum resolution obtained is shown in Figure 4.1 and 4.2.

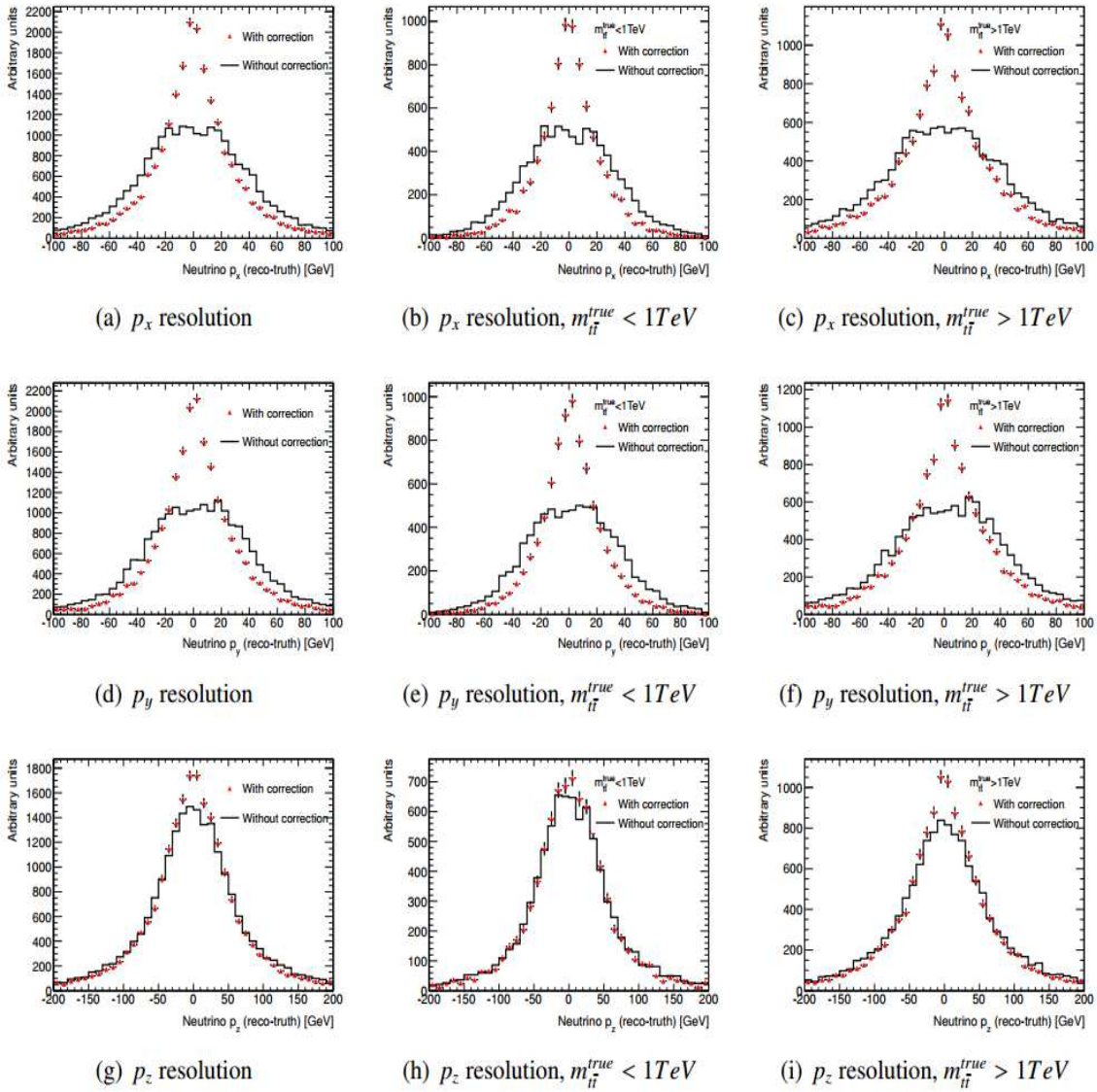

(a) p_x resolution (b) p_x resolution, $m_{t\bar{t}}^{true} < 1TeV$ (c) p_x resolution, $m_{t\bar{t}}^{true} > 1TeV$

(d) p_y resolution (e) p_y resolution, $m_{t\bar{t}}^{true} < 1TeV$ (f) p_y resolution, $m_{t\bar{t}}^{true} > 1TeV$

(g) p_z resolution (h) p_z resolution, $m_{t\bar{t}}^{true} < 1TeV$ (i) p_z resolution, $m_{t\bar{t}}^{true} > 1TeV$

Figure 4.2: Neutrino momentum resolution from the imposition of the W boson mass constraint in the case of a negative discriminant. a,d,g) p_x , p_y and p_z resolution where only the real part of the solution is taken ("Without correction") and the E_T^{miss} is adjusted to get a null discriminant ("With correction"). The two last columns demonstrate the choice of the method does not depend on the invariant mass of the $t\bar{t}$ system.

4.3.1 Resolved selection

Two methods are used to reconstruct the $t\bar{t}$ pair invariant mass in the resolved topologies. The aim of both methods is to identify the jets originating from the top decays among all jets with $p_T > 25GeV$, $|\eta| < 2.5$ and $|JVF| > 0.5$. where JVF is the Jet Vertex Fraction (JVF) defined as the sum p_T of all matched-tracks from a given vertex divided by the total jet matched track P_T:

$$JVF(jet_i, vertex_j) = \frac{\sum_k p_T\left(track_k^{jet_i}, vertex_i\right)}{\sum_n \sum_\rho p_T\left(track_\rho^{jet_i}, vertex_n\right)} \tag{4.3}$$

when JVF is -1, no matching tracks were found, 0 when its a pileup jet and 1 for signal jets.

4.3.1.1 Hardest jets after dRmin cut

The simplest approach, in which no attempt is made to reconstruct the individual top quark four-momenta is to assume the four highest p_T jets come from the $t\bar{t}$ pair decay and to combine them with the charged lepton and the neutrino, choosing the smallest $|p_z|$ solution if there are two real ones, to reconstruct $m_{t\bar{t}}$.

However this method suffers from long, non-gaussian tails in the mass resolution due to the use of a jet from initial or final state radiation instead of one of the jets directly produced in a top quark decay. To reduce this contribution, the *dRmin* algorithm considers the four leading jets, and excludes a jet if its angular distance to the lepton or closest jet satisfies $\Delta R_{min} > 2.5$ - $0.015 \times m_j$, where m_j is the jet's mass (If more then one jet satisfies this condition, the jet with the largest ΔR_{min} is excluded). If a jet has been discarded and more than three jets remain, the procedure is iterated. $m_{t\bar{t}}$ is then reconstructed

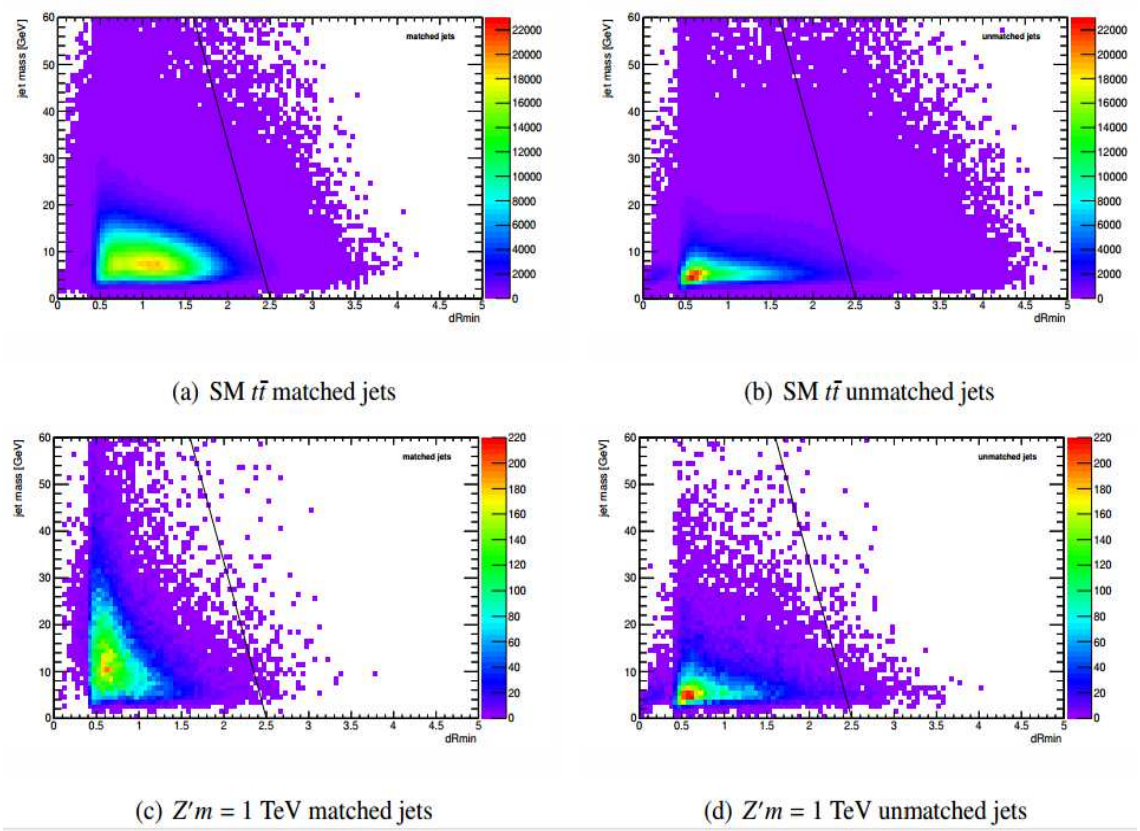

(a) SM $t\bar{t}$ matched jets (b) SM $t\bar{t}$ unmatched jets

(c) $Z'm$ = 1 TeV matched jets (d) $Z'm$ = 1 TeV unmatched jets

Figure 4.3: Correlation between the angular separation to the closest jet and jet mass in SM $t\bar{t}$ (upper row) and a leptophobic topcolor $Z\prime$ with a mass of 1 TeV (bottom row) for jets matched (left column) and not matched (right row) to top quark decay products. Jets to the right of the black line are rejected. The absolute color scale is the same in both plots.

from the lepton, the neutrino and the leading four jets (or three jets if only three remain). This cut removes jets that are "far" from the rest of the activity in the event. Figure 4.3 illustrates the correlation between the angular separation to the closest jet and jet mass for both jets matched and not matched to top quark decay products. While in SM $t\bar{t}$ events a few percent of the jets are discarded by the *dRmin* requirement, which rejects mostly unmatched jets, higher mass resonances are mostly reconstructed using the four hardest jets with a negligible effect from the *dRmin* cut.

If one of the jets has mass $m_j > 60GeV$, it is combined with the jet closest to it to form the hadronic top quark candidate, and the other top quark is formed by combining the reconstructed leptonic W boson candidate with the jet closest to it. The reconstructed

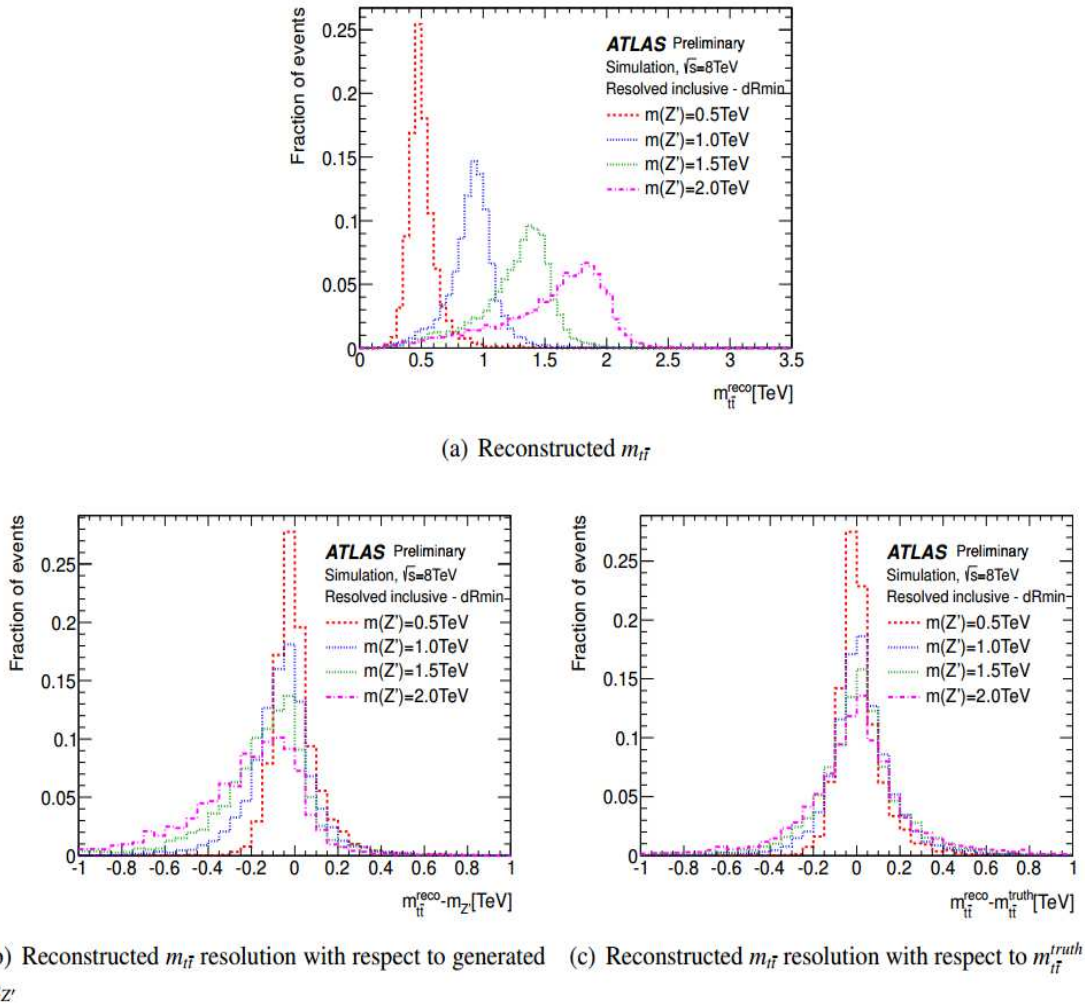

(a) Reconstructed $m_{t\bar{t}}$

(b) Reconstructed $m_{t\bar{t}}$ resolution with respect to generated $m_{Z'}$

(c) Reconstructed $m_{t\bar{t}}$ resolution with respect to $m_{t\bar{t}}^{truth}$

Figure 4.4: Reconstructed $m_{t\bar{t}}$ resolution with respect to generated m_Z.

invariant masses and corresponding resolutions obtained with this algorithm for four different resonance masses: $m = 0.5, 1.0, 1.5$ and $2.0\ TeV$ are shown in Figure 4.4. The tail down to $-0.5\ TeV$ for the highest mass point in Figure 4.4(b) is due to radiation from top quarks, that reduces the invariant mass of the top-quark decays, as shown in Figure 4.7.

4.3.1.2 χ^2 algorithm

To increase the efficiency of selecting the jets produced by top quark decays, a χ^2 is constructed using the constraints from expected top quark and W boson masses :

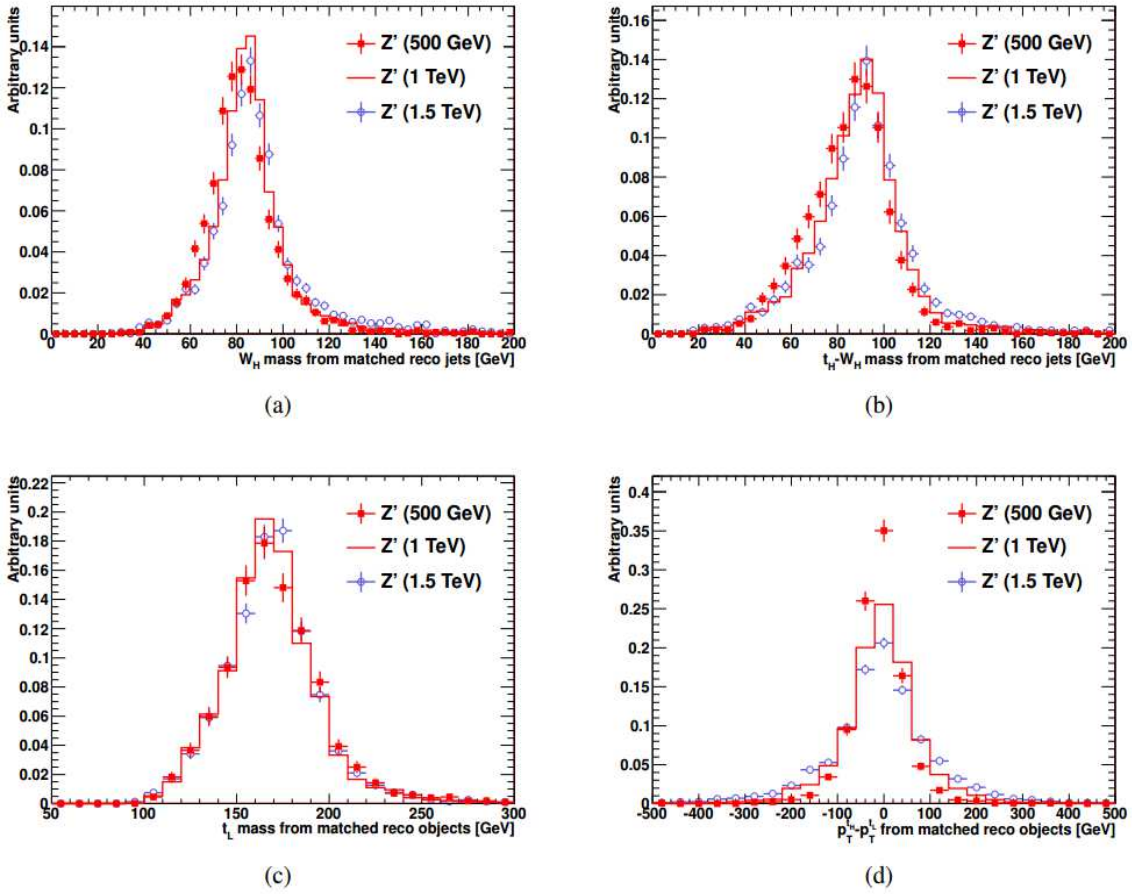

Figure 4.5: Mass of hadronic W (a), hadronic top quark (b), leptonic top quark (c) and $p_T^{t_H} - p_T^{t_L}$, from the decay products at the reconstructed level, for a low (500 GeV), intermediate (1 TeV) and high mass (1.5 TeV) $Z\prime$ samples.

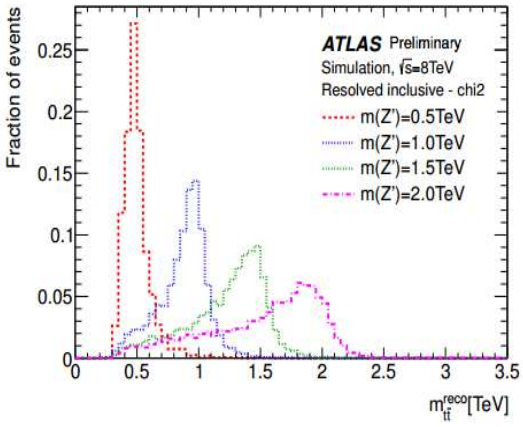

(a) Reconstructed $m_{t\bar{t}}$

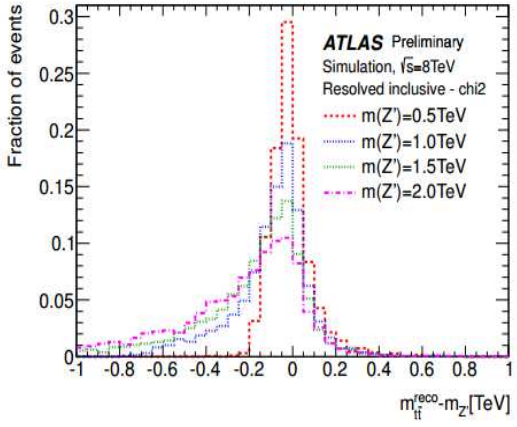

(b) Reconstructed $m_{t\bar{t}}$ resolution with respect to generated $m_{Z'}$

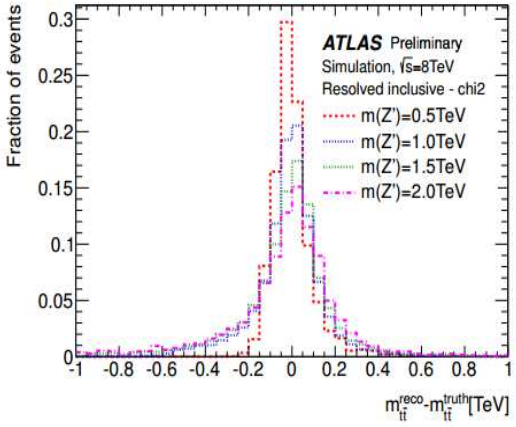

(c) Reconstructed $m_{t\bar{t}}$ resolution with respect to $m_{t\bar{t}}^{truth}$

Figure 4.6: Reconstructed (a) $t\bar{t}$ pair invariant mass using the χ^2 method for four $Z\prime$ masses: $m_{Z\prime} = 0.5$, 1.0, 1.5 and 2.0TeV, and (b,c) corresponding mass resolutions. Both reconstructable and non-reconstructable events are included.

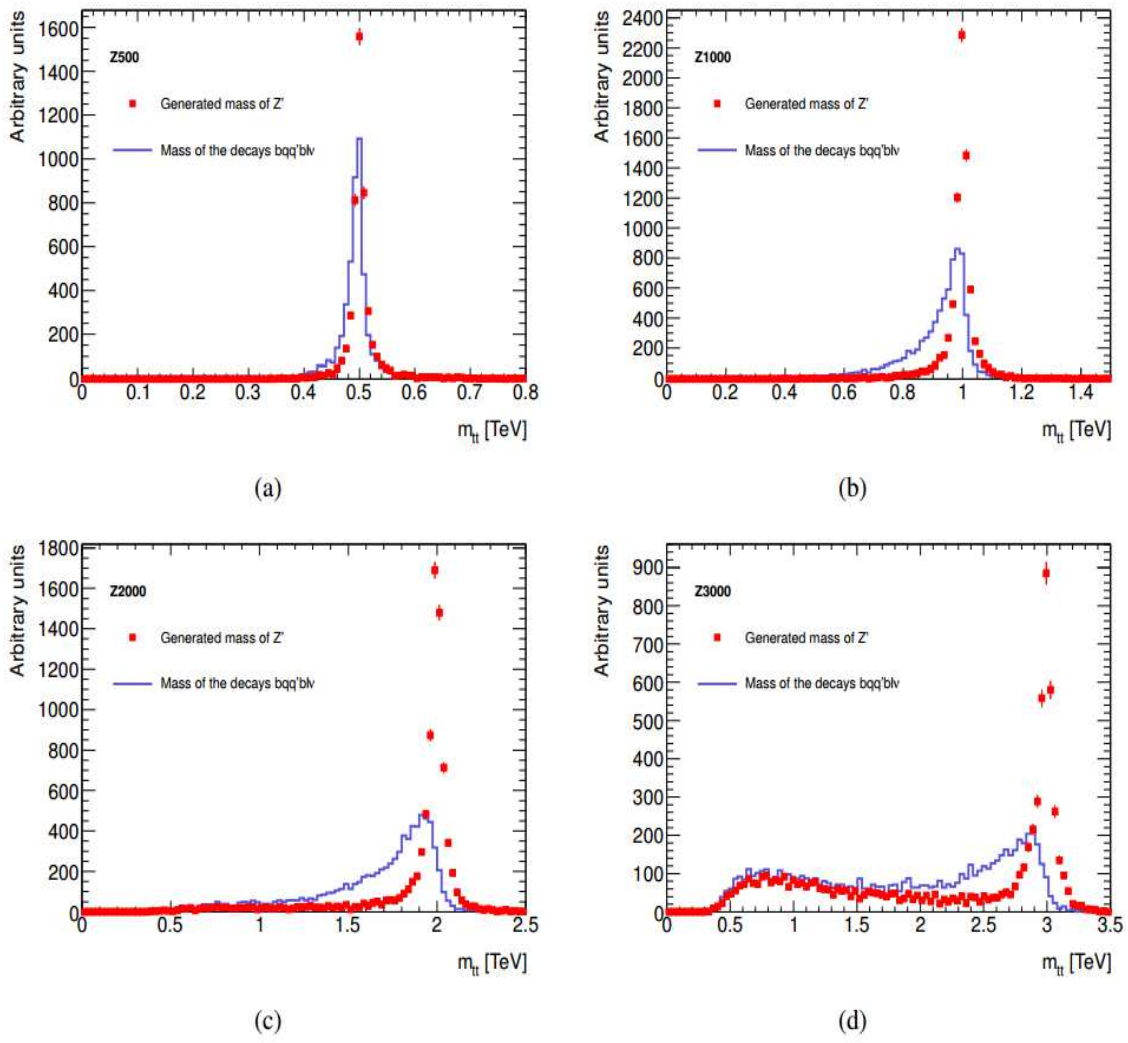

Figure 4.7: Generated $Z\prime$ masses and invariant mass of the decays of the top quarks at the partonic level, for four boson masses: $m_{Z\prime}$ = (a) 1.0, (b) 1.5, (c) 2.0 and (d) 3.0TeV. For the highest mass point, the shape of the generated $m_{Z\prime}$ has a bump at lower mass, because of a combination of off-shell-production suppression and enhancement via the lower- x PDF distributions at 8 TeV of center-of-mass

$$\chi^2 = \left[\frac{m_{jj} - m_W}{\sigma_W}\right]^2 + \left[\frac{m_{jjb} - m_{jj} - m_{th-W}}{\sigma_{th-W}}\right]^2 + \left[\frac{m_{jlv} - m_{tl}}{\sigma_{tl}}\right]^2 + \\ + \left[\frac{(P_{T,jjb} - P_{T,jlv}) - (P_{T,th} - P_{T,tl})}{\sigma_{\Delta P_T}}\right]^2 \tag{4.4}$$

The first term is the constraint from the hadronically decaying W boson. The second term corresponds to the hadronically decaying top quark, but since m_{jj} and m_{jjb} are heavily correlated the hadronically decaying W-boson was subtracted to decouple this term from the previous one. The third term represents the semileptonically decaying top quark, and the last term constrains the top quark transverse momenta to be similar, as expected for a resonance decay. The parameter values are determined from reconstructed MC events in which the right combination is identified from the MC truth information. This is done on a mix of $Z\prime$ samples of masses from 0.5 to 2 TeV, as we want to optimize the algorithm for a search in this range. Figure 4.5 illustrates how the parameters can vary over the full range of interest for the resolved analysis. The values of the parameters are: m_W = 83.3 GeV, m_{th-W} = 91.1 GeV, m_{tl} = 168.2 GeV, σ_W = 10.8 GeV, σ_{th-w} = 14.2 GeV, σ_{tl} = 20.6, $p_{T,th} - p_{T,tl} = -8.7$ GeV and $\sigma_{\Delta p_T}$ 55.0 GeV. In this analysis, all possible jet permutations are tried and only the permutation with the lowest χ^2 is used. This selects the correct combination in approximately 65% of reconstructable events. (Note that in this case, if there are two solutions for the neutrino's longitudinal momentum, both solutions are tried.) If one of the jets has mass $m_j > 60$ GeV, the χ^2 is changed to be:

$$\chi^2 = \left[\frac{m_{jj} - m_{jj}^{th}}{\sigma_{jj}^{th}}\right]^2 + \left[\frac{m_{jlv} - m_{jlv}^{tl}}{\sigma_{jlv}^{tl}}\right]^2 + \left[\frac{(P_{T,jj} - P_{T,jlv}) - (P_{T,th} - P_{T,tl})}{\sigma_{\Delta P_T}}\right]^2 \tag{4.5}$$

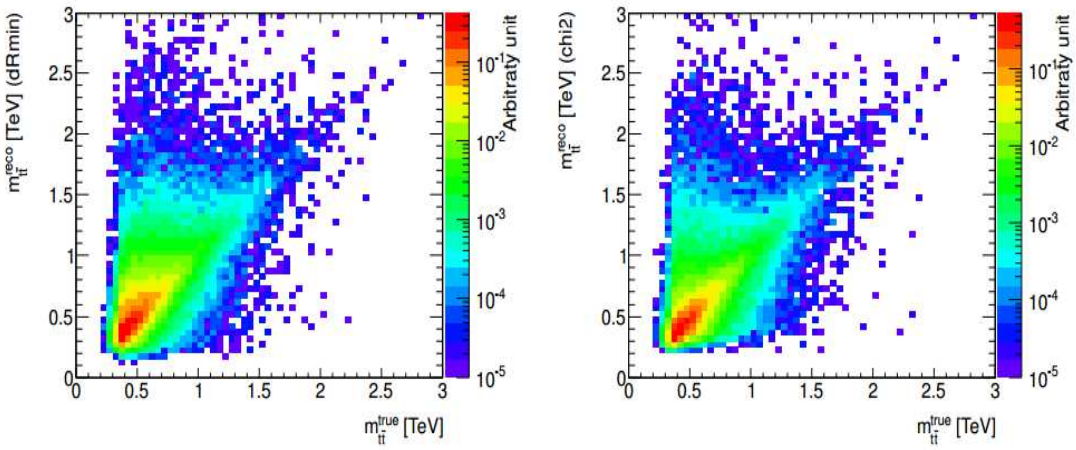

(a) Reconstructed versus true $t\bar{t}$ pair invariant mass, dRmin (b) Reconstructed versus true $t\bar{t}$ pair invariant mass, χ^2

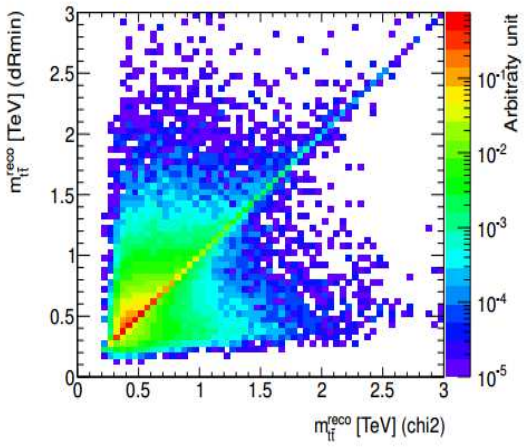

(c) Reconstructed $t\bar{t}$ pair invariant mass, dRmin versus χ^2

Figure 4.8: Reconstructed versus true $t\bar{t}$ pair invariant mass using the dRmin (a) and χ^2 (b) methods for SM $t\bar{t}$ production, and comparison of the two methods (c). Both reconstructable and non-reconstructable events are included.

where the $m_{jj} - m_{jj}^{th}$ term allows the merger of either both quarks from W boson decay, or one quark from W boson decay with the b quark from top quark decay. The values of m_{jj} and m_{jj}^{th} are determined from simulation to be 173.5 GeV, 16.3 GeV respectively. Figure 4.6 shows the reconstructed boson masses for four mass values together with the corresponding mass resolution. The reconstructed mass is shown as a function of true mass in Figure. 4.8.

4.3.1.3 Performance of reconstruction algorithms

In Figure. 4.8 the reconstructed $t\bar{t}$ pair invariant mass is shown as a function of the true mass for SM $t\bar{t}$ production, for the χ^2 (Figure 4.8(a)) and $dRmin$ (Figure 4.8(b)) methods. Figure 4.8(c) shows the correlation between the two methods. In the final result, χ^2 is used as it leads to slightly better expected limits, especially for low mass signals.

4.3.2 Boosted selection

After the event selection in the boosted channel, the selected objects are

- One neutrino, constructed from the E_T^{miss} and the solution of the quadratic equation described in Section 4.3,
- One charged lepton,
- The selected small-R jet identified as the jet from the leptonic top decay,
- One large-R jet, containing the decay products of the hadronically decaying top.

The invariant mass of the $t\bar{t}$ event is computed as the invariant mass of the four reconstructed objects: the neutrino, the charged lepton, the small-R jet and the large-R jet. There is no ambiguity in assignments of the objects to the original top quarks. The reconstructed spectra and resolution for $Z\prime$ samples with masses of 1.0, 1.5, 2.0 and 3.0 TeV are shown in Figure 4.9.

4.4 Background estimation

In this section, background estimation with partly and fully data-driven methods is discussed.

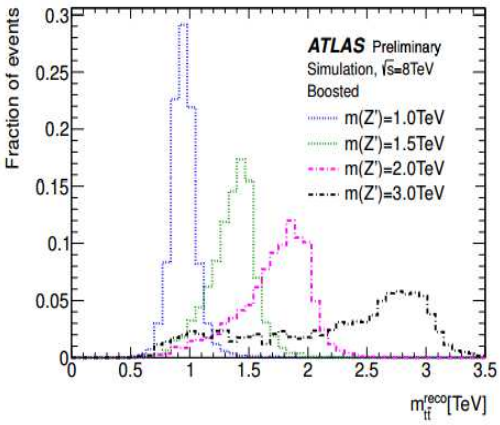

(a) Reconstructed $m_{t\bar{t}}$

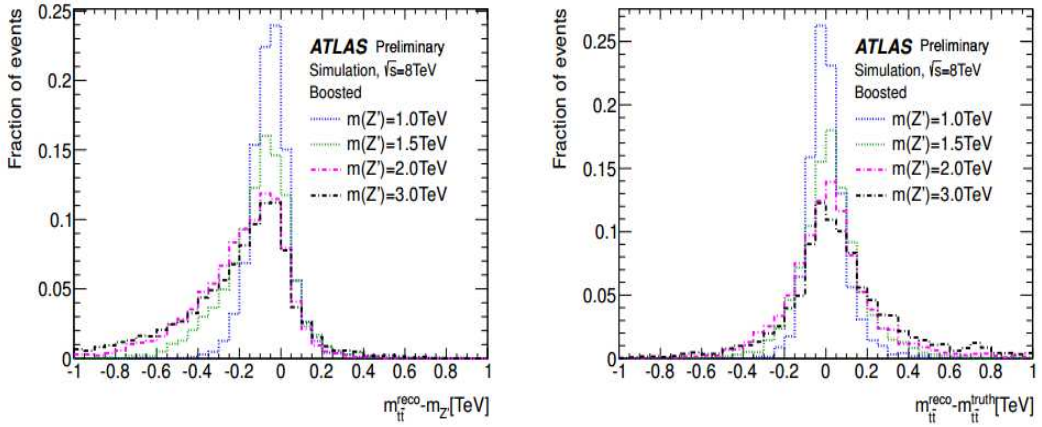

(b) Reconstructed $m_{t\bar{t}}$ resolution with respect to generated $m_{Z'}$

(c) Reconstructed $m_{t\bar{t}}$ resolution with respect to $m_{t\bar{t}}^{truth}$

Figure 4.9: (a) Reconstructed $t\bar{t}$ invariant mass using the boosted selection for four $Z\prime$ masses: m = 1.0, 1.5, 2.0 and 3.0 GeV and (b,c) corresponding mass resolutions.

4.4.1 Background from W+jets

The expected background from W+jets is estimated using ALPGEN MC samples, determining the total normalization and the flavor fractions with data-driven methods. The default scale factors (SF) cannot be blindly used since this analysis uses different selections (mini-isolation for the electron, boosted topologies, ...). However standard ATLAS approaches [89] are used to derive the SF.

4.4.1.1 W+jets normalization in resolved selection

For the W+jets normalization in the resolved selection, the recommended procedure from [89] is used with the object definitions and cuts specific to this analysis. The heavy flavor fractions are extracted from a W+jets dominated region, using all signal selection cuts except b-tagging and jet requirements, and then requiring exactly two jets. Based on the b-jet multiplicity distribution, separated by lepton charge, the SF's are derived for each heavy flavor component. These are then extrapolated into higher-jet-multiplicity bins, keeping the relative ratio between the SF's and the overall normalization unchanged. The overall normalization is then obtain by a different method, exploiting the fact that the W charge-asymmetry in W+jet production is predicted with better precision than the overall normalization, while other major backgrounds (SM $t\bar{t}$ and multi-jet) are charge-symmetric. The total number of W+jets events in data, $N_{W+} + N_{W-}$, can be estimated from the observed charge asymmetry in data and the predicted charge asymmetry in W+jets events from MC simulation:

$$N_{W+} + NW- = \frac{r_{MC}+1}{r_{MC}-1}\,(D_{corr+} - D_{corr-}) \tag{4.6}$$

Jet bin	F_{bb},F_{cc}	F_c	F_{ll}	Normalization factor
$3ex$	1.46 ± 0.39	0.94 ± 0.44	0.90	0.87 ± 0.16
$4in$	1.40 ± 0.37	0.90 ± 0.43	0.87	0.89 ± 0.16

Table 4.1: *Scale factors for the W+jets samples, electron channel.*

Jet bin	F_{bb},F_{cc}	F_c	F_{ll}	Normalization factor
$3ex$	1.60 ± 0.40	0.87 ± 0.33	0.89	0.96 ± 0.13
$4in$	1.52 ± 0.38	0.83 ± 0.31	0.85	0.95 ± 0.15

Table 4.2: *Scale factors for the W+jets samples, muon channel.*

where r_{MC} is the ratio, from MC, of W+jets events with a positive lepton to those with a negative lepton. $D_{corr+(-)}$ is the number of observed events with a positive (negative) lepton, with the prediction for charge asymmetric events (single top, diboson) subtracted. The SF's thus obtained are listed in Tables 4.1 and 4.2, for exclusive 3-jets and inclusive 4-jets bins respectively. The uncertainties are estimated based on statistical uncertainties, MC systematics, detector resolution, reconstruction and identification efficiency uncertainties. For the heavy flavor scale factors, the uncertainties quoted in the tables represent the variation of $b\bar{b}$, $c\bar{c}$ and c components. The SFs (including normalization) are then recalculated following the same procedure, with three combinations as:

- WHFC0: Both $b\bar{b}$, $c\bar{c}$ and c components are varied by their uncertainties with full correlation, while keeping light-flavor component unchanged.
- WHFC3: The $b\bar{b}$ and $c\bar{c}$ components are varied together
- WHFC4: Only the c component is varied

All the three variants are considered as W+jets uncertainties in the limit setting.

The normalization SF's from Cambridge Aachen (CA) method are generally consistent with unity within their uncertainties. Figures 4.10 and 4.11 show the data/MC agreement

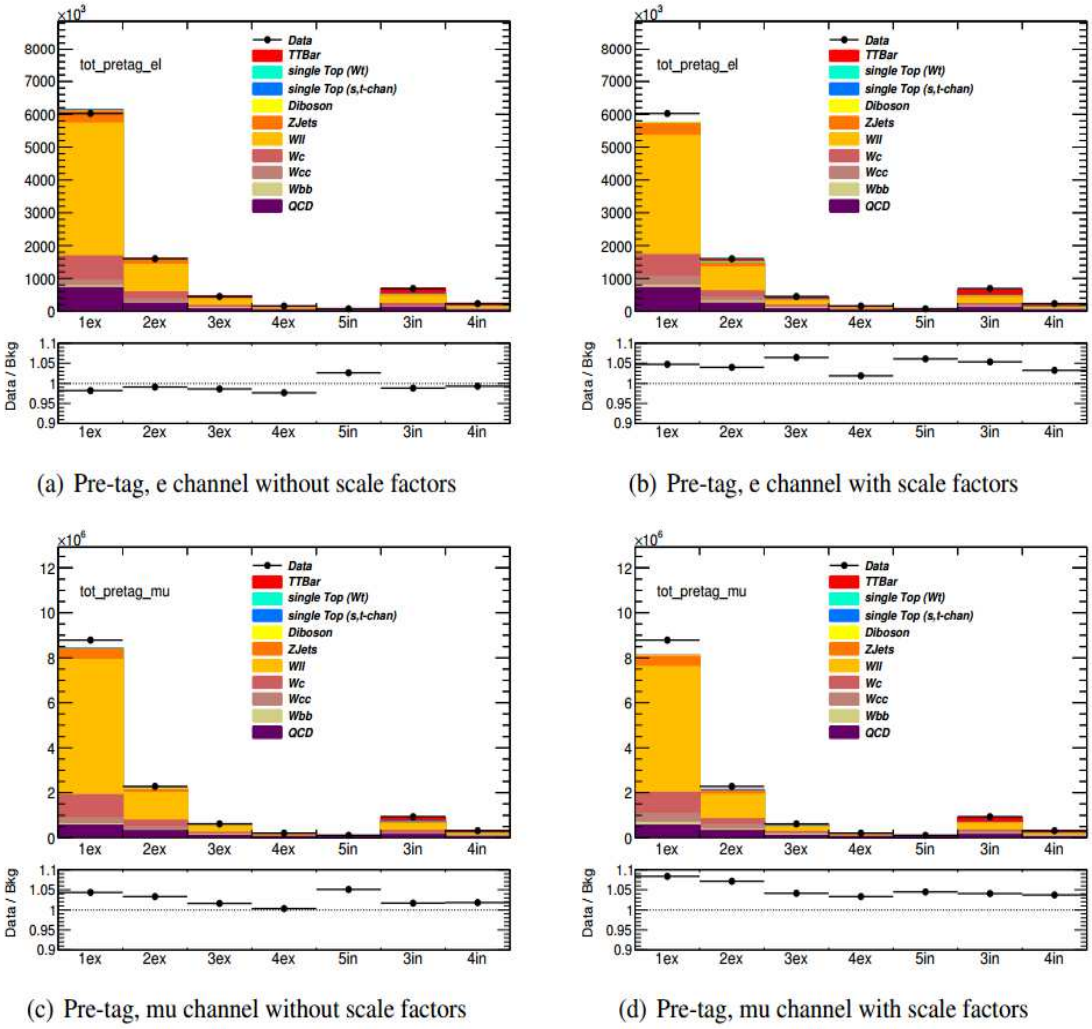

(a) Pre-tag, e channel without scale factors

(b) Pre-tag, e channel with scale factors

(c) Pre-tag, mu channel without scale factors

(d) Pre-tag, mu channel with scale factors

Figure 4.10: Number of events before b-tagging in various jet multiplicity bins, before (left) and after (right) applying the SF's for the W+jets background.

before and after applying the W+jets scale factors, for events both with and without the requirement of a b-jet. Although the general agreement is not improved by the nominal SFs, the method does provide a good constraint on the systematics due to the cancellation of many factors.

4.4.1.2 W+jets normalization in boosted selection

The heavy flavor SF's (of four jets inclusive) derived above are used for boosted selection as well. The charge-asymmetry method is used again to derive normalization SF's in this

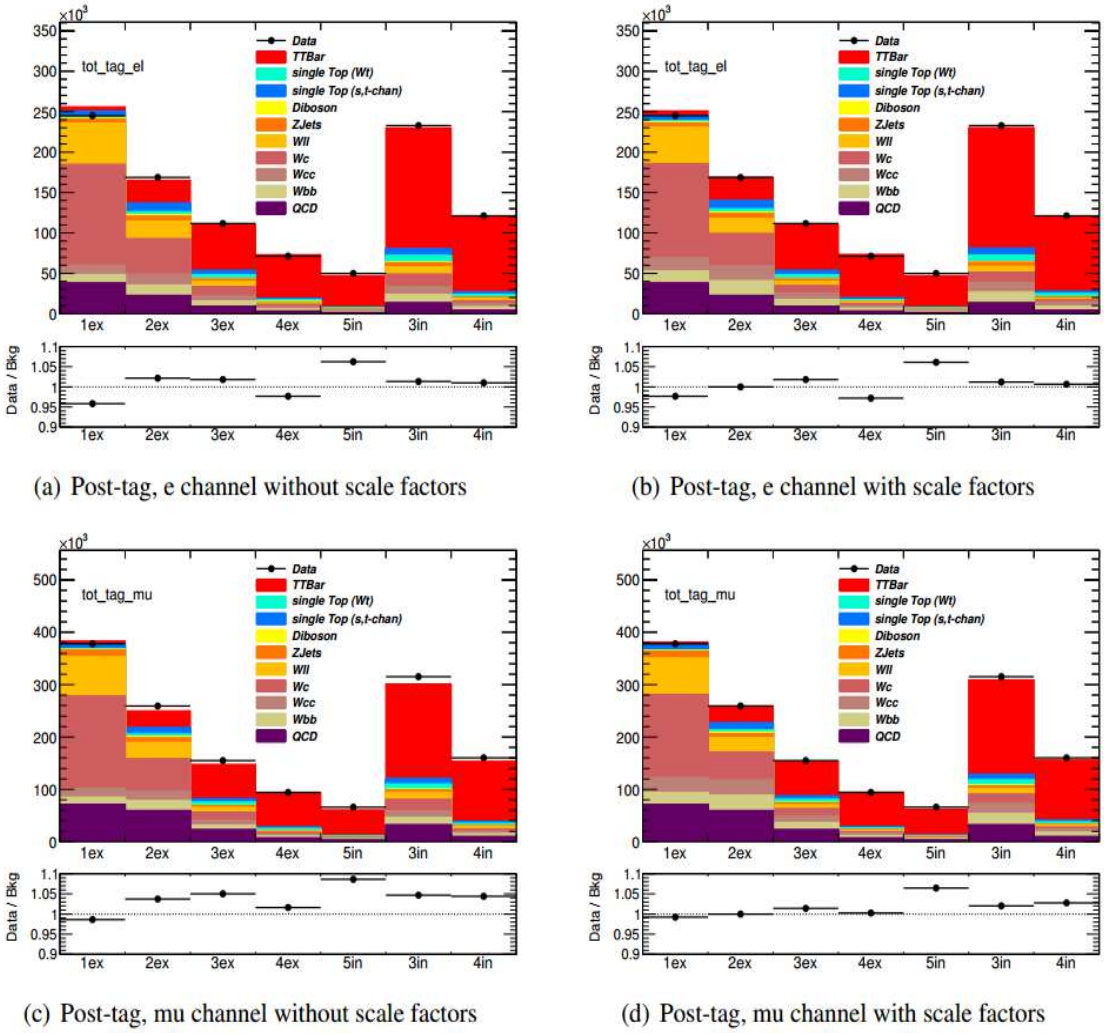

(a) Post-tag, e channel without scale factors

(b) Post-tag, e channel with scale factors

(c) Post-tag, mu channel without scale factors

(d) Post-tag, mu channel with scale factors

Figure 4.11: Number of events after b-tagging in various jet multiplicity bins, before (left) and after (right) applying the scale factors for the various flavor contributions of the W+jets background.

new kinematic region. The signal region event yield after the boosted selection is too small for a reliable evaluation of the appropriate SF's, so a normalization region is used. To enhance the W+jets content in such normalization region, the b-tagging, $\Delta\phi\,(jet, l) > 2.3$, jet mass and $\sqrt{d_{12}}$ requirements are not applied. The p_T cut on the jet with $R = 1$ is kept as 300 GeV.

The SF's for the electron (muon) channel is $0.65 \pm 0.14 (0.81 \pm 0.13)$. The uncertainties include statistical uncertainties, systematics from heavy-flavor fractions, MC uncertainties, as well as other resolution, reconstruction and identification efficiency uncertainties.

4.4.2 Background from non-prompt lepton sources

The simulation of the background from sources of non-prompt leptons (mainly QCD multijet production) suffers from large systematic and statistical uncertainties and this background must hence be estimated directly from data. This is achieved by investigating the phase space regions with leptons of lower reconstruction quality. Such regions are generally more populated by QCD multijet events. The event topology and kinematic criteria are chosen to resemble the definition of our signal region, in order to reduce potential systematic uncertainties. A so-called matrix method is used to disentangle the mixture of non-prompt leptons found in the multijet background, and prompt leptons originating from the W/Z bosons. As a crosscheck, template based methods are used to evaluate the precision of the estimation. Both estimates are computed for the two selections. The matrix method is used as the nominal QCD estimation.

4.4.2.1 The matrix method

The matrix method first requires a definition of a "loose" lepton, which is achieved by loosening certain signal selection cuts on the leptons to enhance the fraction of multijet events. The efficiency ϵ is defined as the probability that a loose lepton from prompt sources (W or Z bosons) passes the tighter signal selection. The false-identification rate f denotes the probability that a non-prompt lepton from multijets production passes the same selection.

With f and ϵ derived from data or validated with data, the QCD background in the signal region is estimated with data events which pass all of the signal selection, except that the loose lepton definition is used. This sample contains both events from prompt-lepton sources and QCD multijet events.

The total number of loose leptons, N_L can be defined as

$$N_L = N_{prompt} + N_{QCD} \tag{4.7}$$

Among them, those events with tight leptons should be composed as

$$N_T = \epsilon \times N_{prompt} + f \times N_{QCD} \tag{4.8}$$

Solving these two equations for N_{prompt} and N_{QCD}, makes it possible to estimate the QCD contribution to the signal region as

$$f \times N_{QCD} = \frac{(\epsilon - 1)\, f}{(\epsilon - f)} N_T + \frac{\epsilon f}{(\epsilon - f)} N_A \tag{4.9}$$

N_T is the number of events with a tight lepton, and N_A is the number of events with

	electrons	muons
loose	mediumPP AND conversion rejection(*)	all quality cuts except isolation
tight	tightPP AND isolated	isolated

Table 4.3: *Definitions of the loose leptons used for the matrix method QCD estimation. The tight selections are given for reference. The suffix "PP" stands for PlusPlus and is used to differentiate from the set of cuts used for the ATLAS analysis in 2010.*

anti-tight lepton (i.e. a loose lepton which failed the tight cuts).

In addition to predicting the overall QCD yields in our signal region, the method can also be used to estimate the kinematic distributions of the QCD background. A weight can be calculated for each event in the aforementioned sample, using Eq. 4.9, with (N_T, N_A) = (0, 1) or (1,0). So long as any dependency the f and the ϵ have on the variable is sufficiently characterised by the chosen parametrisation, the weighted sample will give the corresponding distribution of the QCD contribution

The definitions of the loose leptons are given in Table 4.3.

The loose leptons from the QCD multijet process have a small probability to pass the tight definition. This false-identification f , is measured (Figures 4.12(c,d,e) and 4.13(d,e,f)) from data with QCD-enhanced control samples, denoted as Control Region 0 (CR0), defined with the following set of cuts:

- $CR0_{resolved}$:
  - $E_T^{miss} < 30$ GeV AND $M_T < 30$ GeV, (electron channel)
  - $E_T^{miss} < 20$ GeV AND $E_T^{miss}+M_T < 60$ GeV, (muon channel)
  - and $|d0sig^2| > 4$ for the muon, $|d0sig| > 2.5$ for the electron.
- $CR0_{boosted}$:

[2] d0sig is d_0 impact parameter divided by the standard error of d_0

- $E_T^{miss} < 60$ GeV AND $M_T < 60$ GeV, (electron channel)
- $E_T^{miss} < 60$ GeV AND $E_T^{miss} + M_T < 60$ GeV, (muon channel)
- and $|d0sig| > 4$ for the muon, $|d0sig| > 2.5$ for the electron.

To keep this measurement compatible with the f in the signal region, the same event topology as our signal selections was required. This includes the kinematic requirement on the selected objects, and the angular separations between them. The leptons were only required to pass the loose cuts, to enable a study of the false-ID rate.

The efficiencies ϵ (one for each lepton flavor, and for boosted/resolved selections respectively) are measured from simulated SM samples with the same process mixture as found in the signal region, using the standard selections except the lepton criteria, which are "loose". The efficiency is equal to the fraction of reconstructed loose leptons (matched to the true lepton from the W decay to ensure they are not fake leptons) that pass the tight cuts, see Figures 4.12(a,b) and 4.13(a,b). It has been validated in data that this efficiency is well-modelled in MC [89]. Systematic uncertainties on the matrix method estimation were studied by varying the definition of loose leptons, changing the selection used to form the control region and testing alternative parameter isations of the efficiency and the fake rate. In general, a 50% overall uncertainty on the QCD yields was found to be conservative enough for all considered factors. In addition, the modeling of the $M_{t\bar{t}}$ shape from multi-jets contribution is validated using the QCD-enriched CR0. A very good description of the $t\bar{t}$ invariant mass $M_{t\bar{t}}$ for the tight-lepton events is obtained (Figure 4.14), which indicates that the parametrization of efficiency and fake rate is sufficient to provide a good shape prediction.

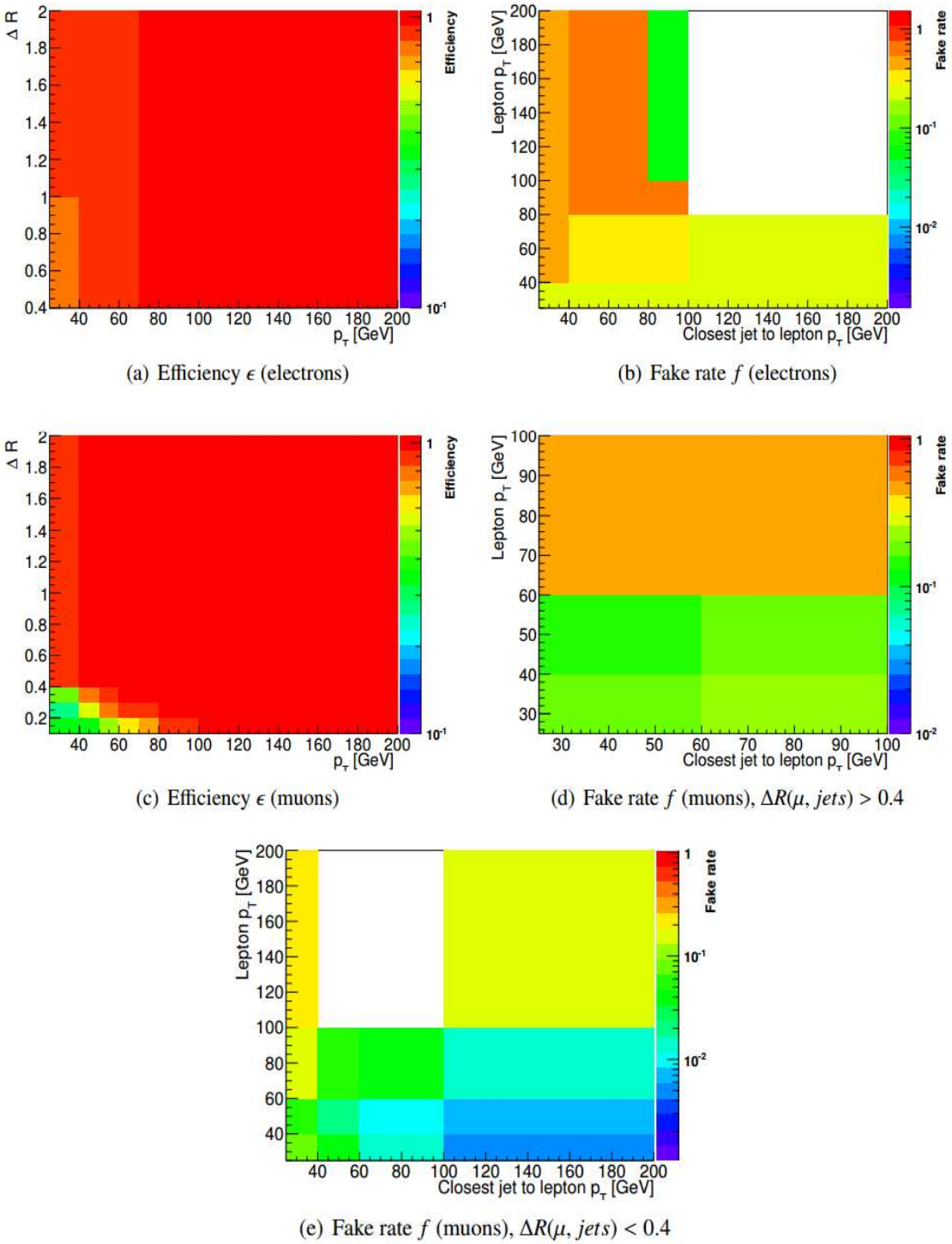

(a) Efficiency ϵ (electrons)

(b) Fake rate f (electrons)

(c) Efficiency ϵ (muons)

(d) Fake rate f (muons), $\Delta R(\mu, jets) > 0.4$

(e) Fake rate f (muons), $\Delta R(\mu, jets) < 0.4$

Figure 4.12: (a, c) Efficiencies ϵ for loose prompt leptons to be identified as tight and (b, d, e) fake rates f for the fake loose leptons to be identified as tight, as a function of the lepton p_T for the resolved selection.

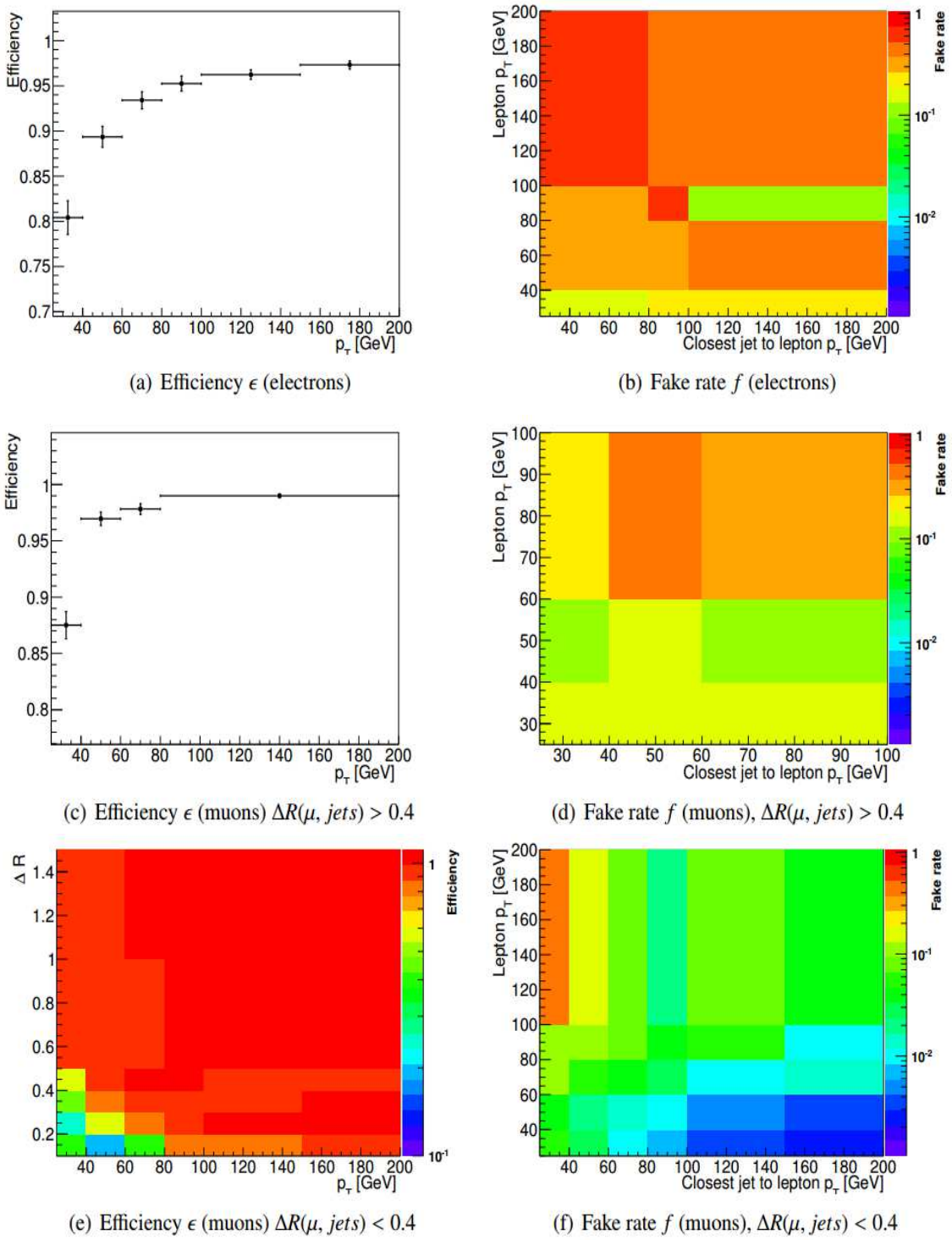

(a) Efficiency ϵ (electrons)

(b) Fake rate f (electrons)

(c) Efficiency ϵ (muons) $\Delta R(\mu, jets) > 0.4$

(d) Fake rate f (muons), $\Delta R(\mu, jets) > 0.4$

(e) Efficiency ϵ (muons) $\Delta R(\mu, jets) < 0.4$

(f) Fake rate f (muons), $\Delta R(\mu, jets) < 0.4$

Figure 4.13: (a, c, e) Efficiencies ϵ for loose prompt leptons to be identified as tight and (b, d, f) fake rates f for the fake loose leptons to be identified as tight, as a function of the lepton p_T for the boosted selection

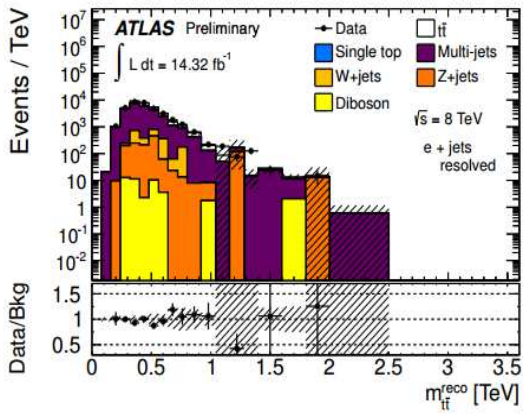

(a) $m_{t\bar{t}}$ in QCD control region (resolved *dRmin*, *e*)

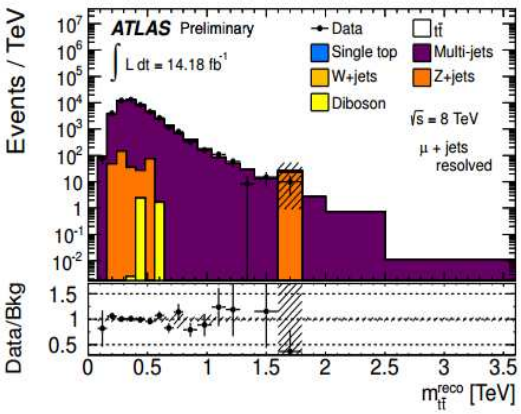

(b) $m_{t\bar{t}}$ in QCD control region (resolved *dRmin*, μ)

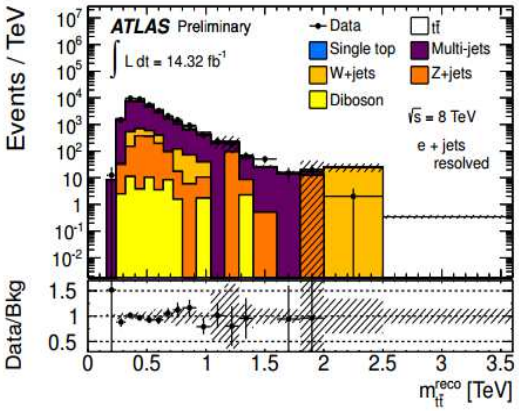

(c) $m_{t\bar{t}}$ in QCD control region (resolved χ^2, *e*)

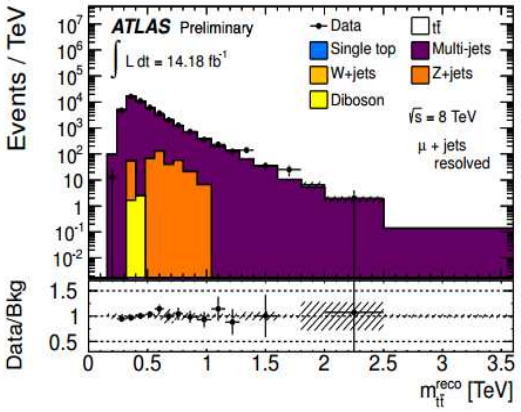

(d) $m_{t\bar{t}}$ in QCD control region (resolved χ^2, μ)

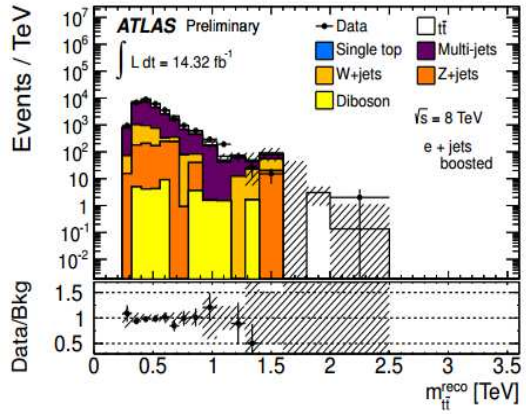

(e) $m_{t\bar{t}}$ in QCD control region (boosted, *e*)

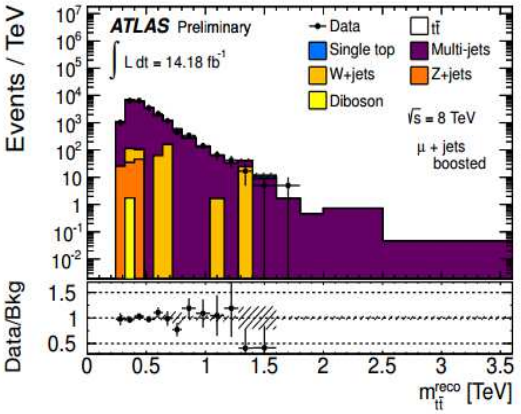

(f) $m_{t\bar{t}}$ in QCD control region (boosted, μ)

Figure 4.14: Reconstructed $M_{t\bar{t}}$ in the Matrix Method QCD control regions for the resolved *dRmin*(a, b), resolved χ^2 (c,d), and the boosted (e, f) selections, with lepton passing the tight selection

4.4.2.2 The antimuon method

The anti-muon method, described in more detail in Ref [89]. is used to cross check the matrix method (MM) background estimate [3]. This is a fully data-driven method in which a minimal set of lepton quality cuts are modified or inverted in order to obtain a sample enriched with non-prompt lepton events, with similar characteristics to those passing the normal event selection. The lepton quality cuts that are changed are:

- No cut on z_0 is applied for the lepton
- $etcone/p_T > 0.03$
- mini-isolation$/P_T^l < 0.1$
- The muon is non-isolated.
- The muon energy loss is < 6 GeV

No special requirements are made on the trigger. The template obtained from this selection, together with MC templates for the various SM processes, are fitted to the data M_T distributions (made for the signal selection without cutting on E_{miss}^T or M_T). The distributions of M_T after the fitting are shown in Figure 4.15, for both ≥ 0 b-tags and ≥ 1 b-tags. The resulting SF's is then used to normalize the antimuon template events in the signal region for final prediction. The kinematic distributions predicted from the template are validated in a QCD-enriched sub-sample, by applying all resolved signal selection with an extra cut on $|d0sig| > 5$. Figure 4.16 compares data to background estimation in different kinematic variable, while Figure 4.17 shows the predicted $M_{t\bar{t}}$ distributions. In general the model gives a good prediction.

[3] The identical method to the reference is used, taking into -account our different lepton isolation and overlap-removal cuts.

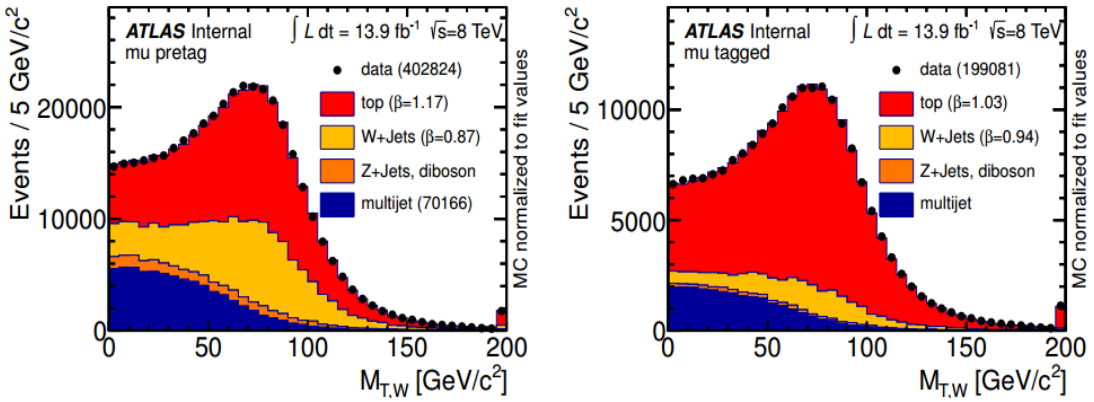

(a) M_{T} in $\geq 0b$-jets Antimuon CR (resolved, *mu*) (b) M_{T} in $\geq 1b$-jets Antimuon CR (resolved, *mu*)

Figure 4.15: Distributions used in the fit to extract normalisation of the anti-muon templates for $(a, c) \geq 0$ b-jets and $(b, d) \geq 1$ b-jets.

For the time being the anti-muon serves as a cross-check to the matrix method in the resolved muon channel, as shown in Figure 4.18. The agreement over $M_{t\bar{t}}$ is within the expected systematic uncertainty.

4.5 Comparison of data and background expectations

After the event selection, 280251 data events pass the resolved selection and 5122 the boosted. 4589 events pass both selection criteria. The event yields are listed in Table 4.4.

It can be seen from Table 4.4 that almost 60 times as many events pass the resolved selection as the boosted (280251 vs 5122) which reflects the nature of the falling mass spectrum of the top quark pairs. For both selections, $t\bar{t}$ is the dominating background, consisting of around 75% (85%) of the total background in the resolved (boosted) selection. The sub-leading backgrounds are W+jets, QCD and single top for both selections.

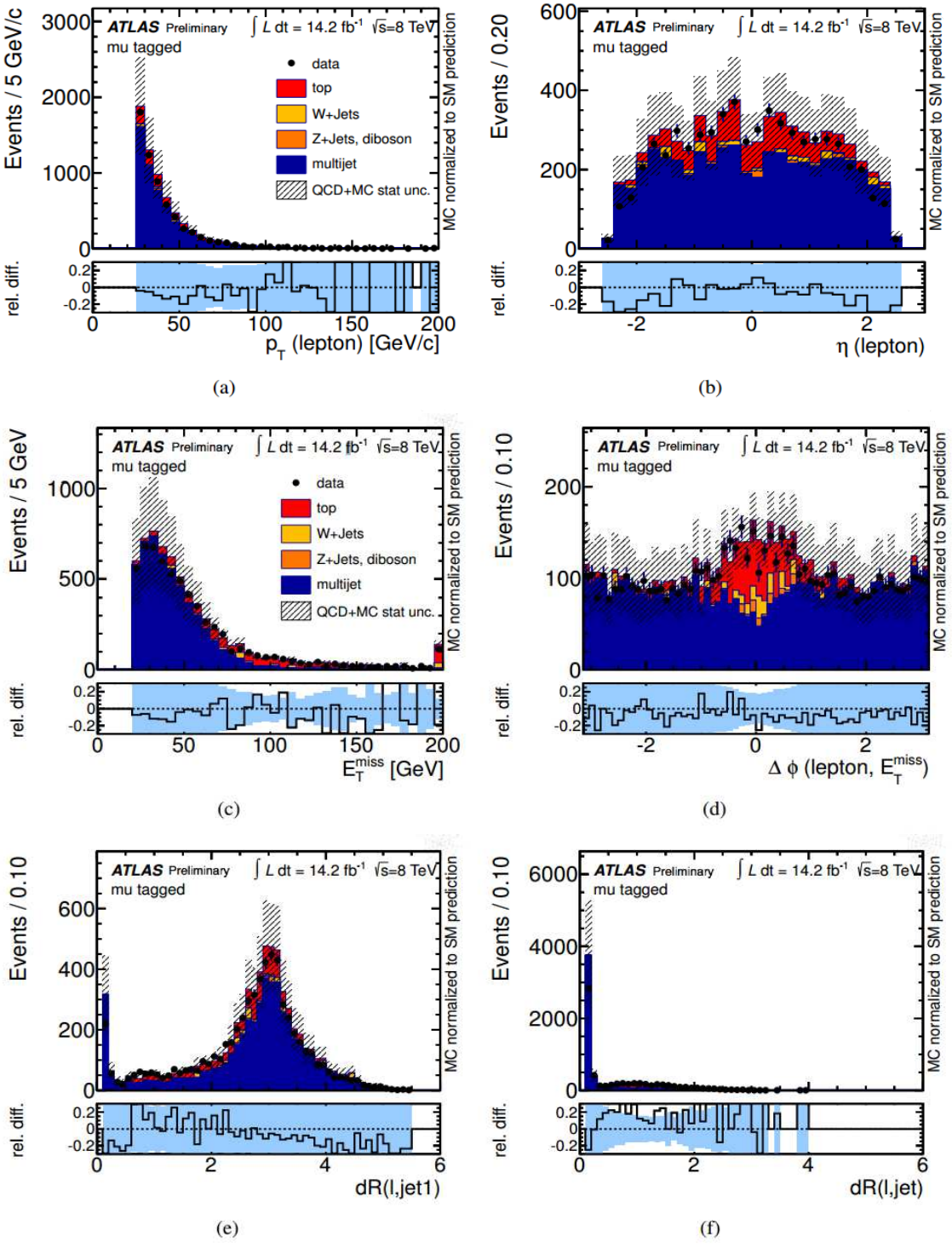

Figure 4.16: Distributions in the QCD-enriched region, with resolved muon selection and an extra cut $|d0sig| > 5$. (a) p_T of the lepton, (b) η of the lepton, (c) the E_T^{miss} (d) $\Delta\phi$ between the muon and the E_T^{miss}, (e) ΔR between the lepton and the leading jet, and (f) ΔR between the lepton and closest jet.

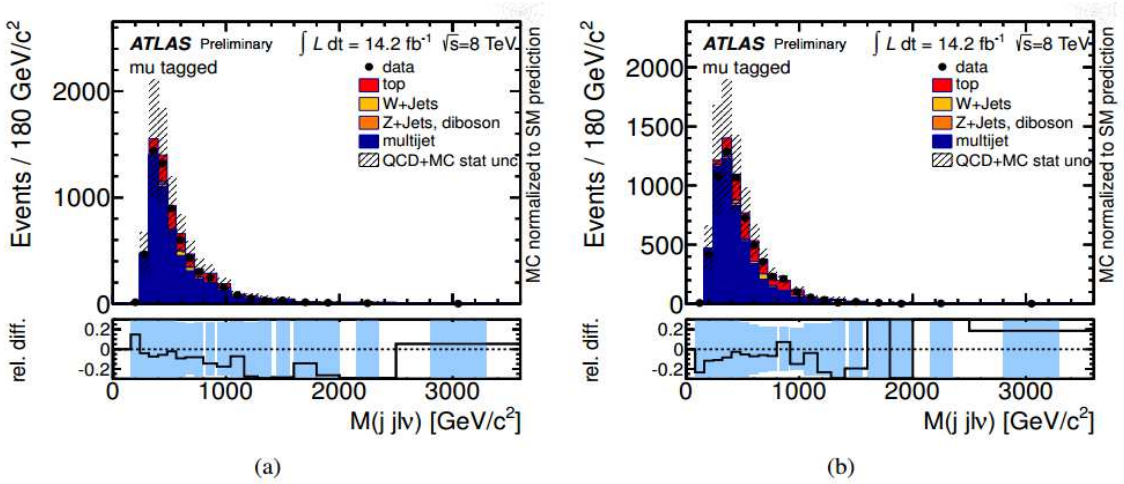

Figure 4.17: Comparison between anti-muon and MM estimation of the non-prompt background in the resolved selection, $dRmin$, μ channel..

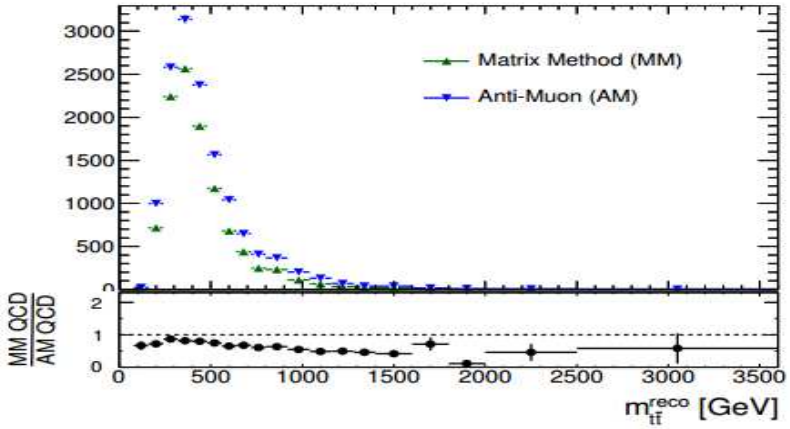

Figure 4.18: Comparison between anti-muon and MM estimation of the non-prompt background in the resolved selection, $dRmin$, μ-channel.

4.5.1 Resolved Selection

The data is compared to expectations for the resolved selection in Figures 4.19-4.26. The comparisons are shown for lepton kinematics in Figures 4.19 and 4.20, E_T^{miss} in Figure 4.21 and M_T in Figure 4.22. The jet multiplicity is shown in Figure 4.23, the distance ΔR between the lepton and the closest jet is shown in Figure 4.24. Finally the kinematics of the jets are shown in Figures 4.25 and 4.26. In general, the agreement between data and expectation is satisfactory.

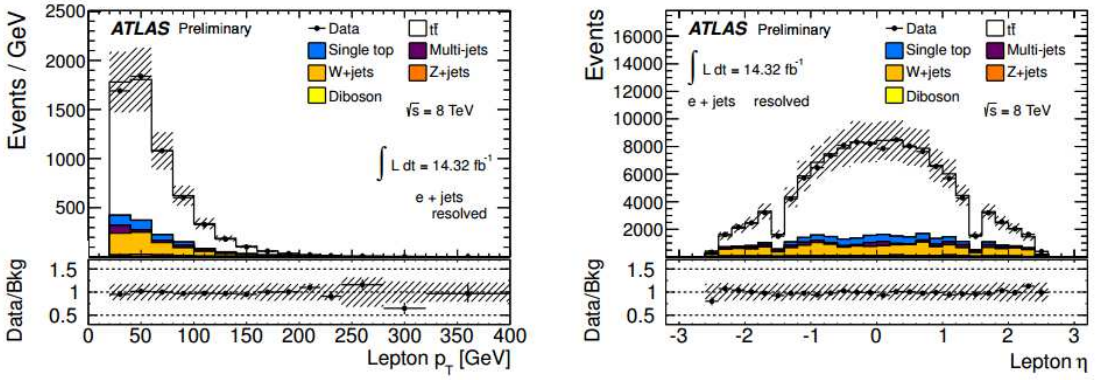

(a) (b)

Figure 4.19: Lepton kinematics in the resolved selection, electron channel. In this and all subsequent figures the shaded band indicates the total systematic uncertainty on the MC from all systematics used later in the limit setting.

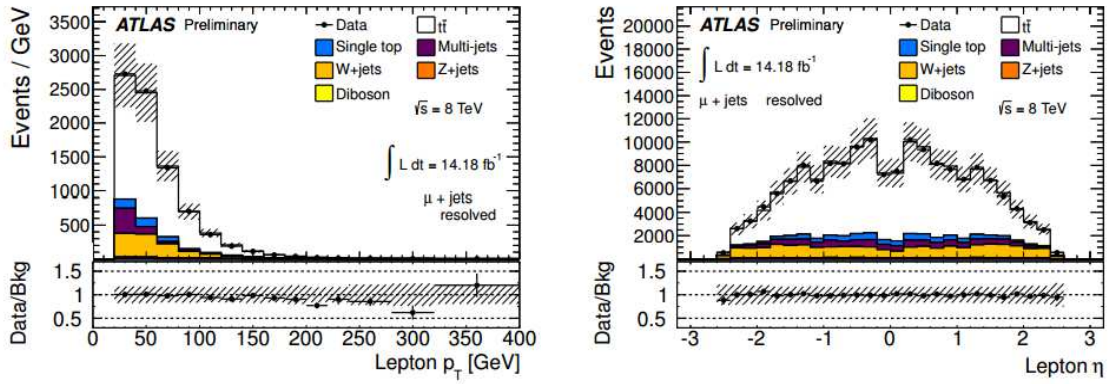

(a) (b)

Figure 4.20: Lepton kinematics in the resolved selection, muon channel.

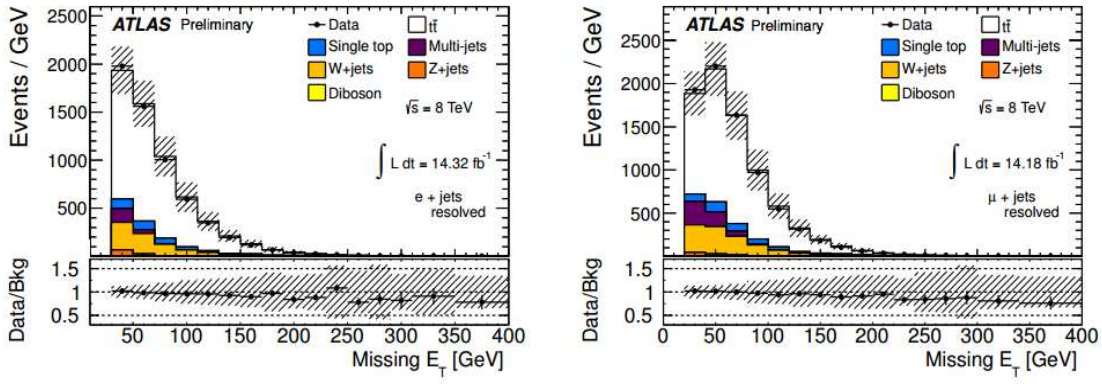

(a) Electron channel (b) Muon channel

Figure 4.21: Missing transverse momentum in the resolved selection.

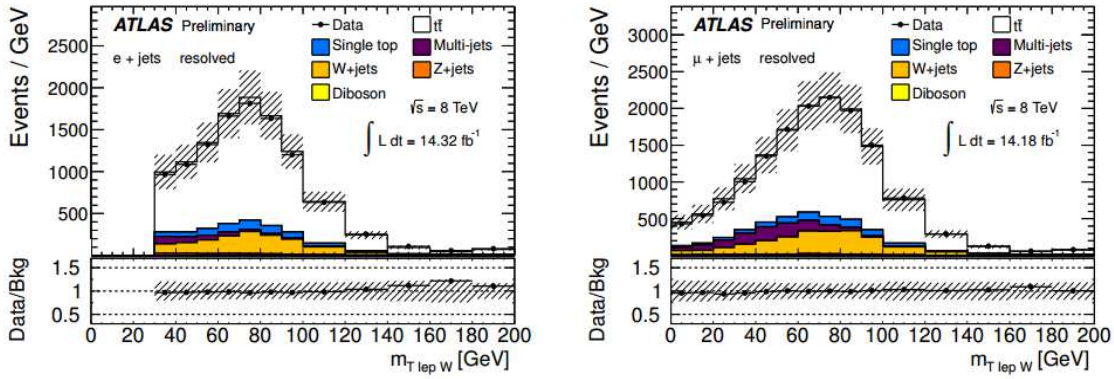

(a) Electron channel (b) Muon channel

Figure 4.22: Transverse mass in the resolved selection.

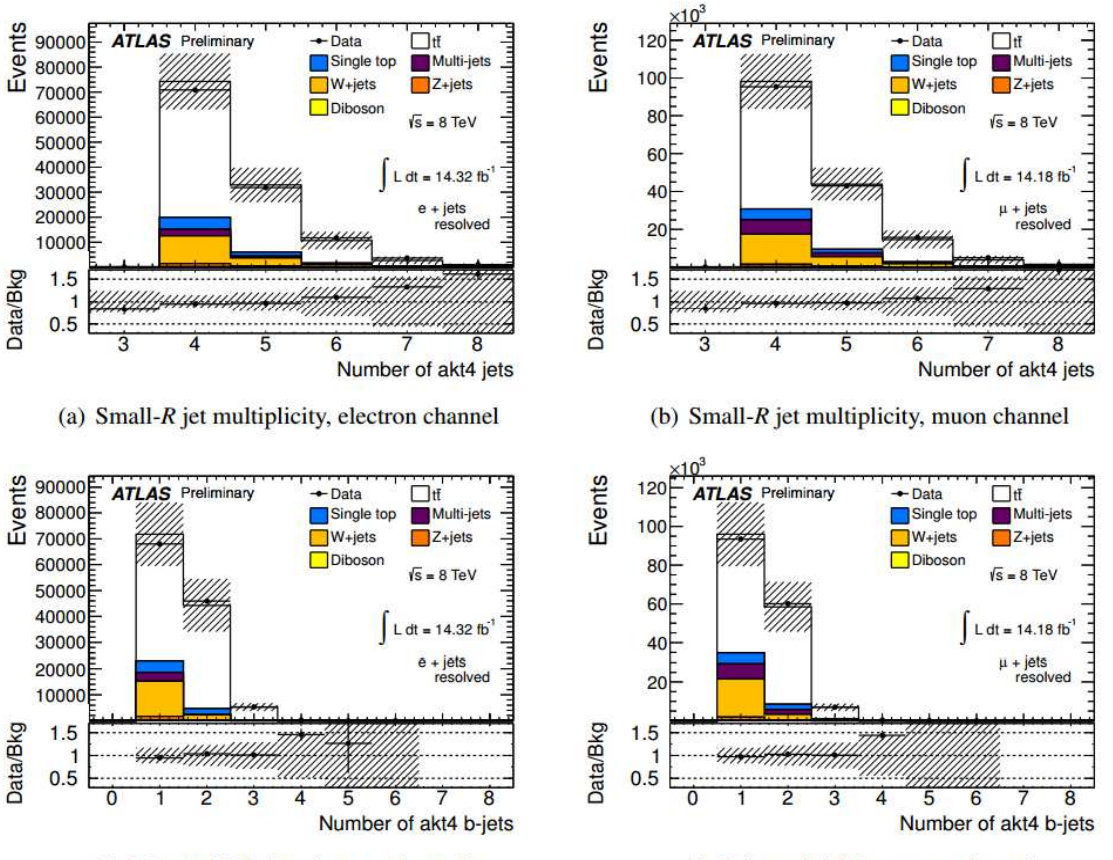

(a) Small-R jet multiplicity, electron channel (b) Small-R jet multiplicity, muon channel

(c) b-jet multiplicity, electron channel (d) b-jet multiplicity, muon channel

Figure 4.23: Small-R jet and b-jet multiplicity, resolved selection.

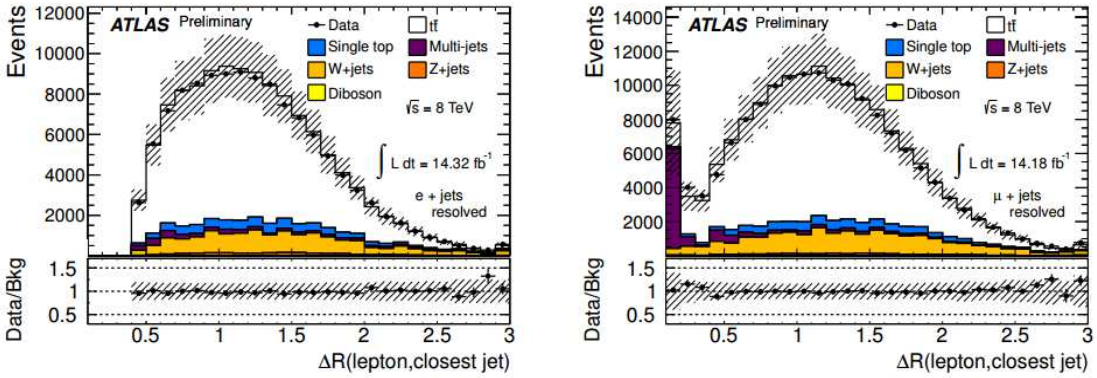

(a) Electron channel (b) Muon channel

Figure 4.24: Distance between the lepton and the closest jet, resolved selection.

	Resolved selection		
Type	e+ jets	μ+ jets	sum
$t\bar{t}$	93371 ± 14872	117664 ± 18811	211035 ± 33462
Single top	6762 ± 836	8405 ± 1123	15167 ± 1927
QCD e	3678 ± 1839	0.0 ± 0.0	3678 ± 1839
QCD μ	0.0 ± 0.0	10443 ± 5221	10443 ± 5221
W + jets	15624 ±	4159 23024 ± 5849	38648 ± 9925
Z + jets	1787 ± 421	1787 ± 382	3574 ± 799
Di-bosons	226 ± 45	319 ± 59	545 ± 103
Total	121447 ± 17230	161641 ± 22606	283088 ± 39146
Data	119490	160878	280251

	Boosted selection		
Type	e+jets	μ+ jets	sum
$t\bar{t}$	2076 ± 485	2785 ± 643	4861 ± 1122
Single top	71 ± 15	105 ± 22	176 ± 34
QCD e	39 ± 19	0.0 ± 0.0	39 ± 19
QCD μ	0.0 ± 0.0	32 ± 16	32 ± 16
W + jets	167 ± 63	309 ± 87	476 ± 141
Z + jets	18 ± 11	33 ± 8	52 ± 15
Di-bosons	2.0 ± 0.8	1.5 ± 1.4	3.5 ± 1.8
Total	2373 ± 541	3266 ± 700	5639 ± 1234
Data	2177	2945	5122

Table 4.4: *Selected data events and expected background yields after the full resolved or boosted selection. The associated systematic uncertainties on the yields are also shown.*

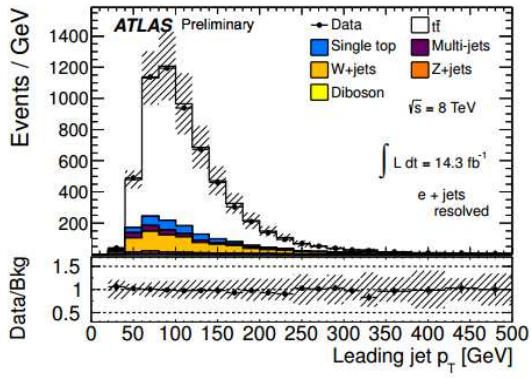

(a) Leading jet p_T, electron channel

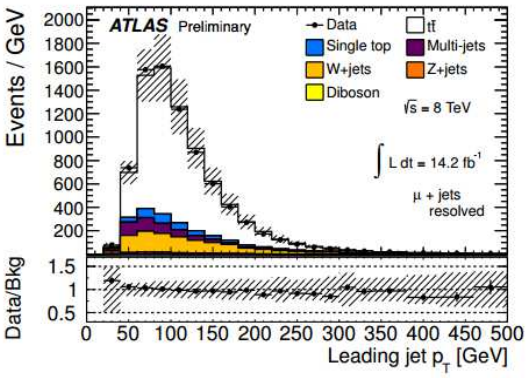

(b) Leading jet p_T, muon channel

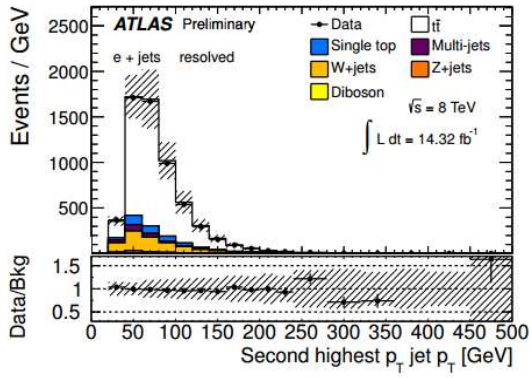

(c) Second jet p_T, electron channel

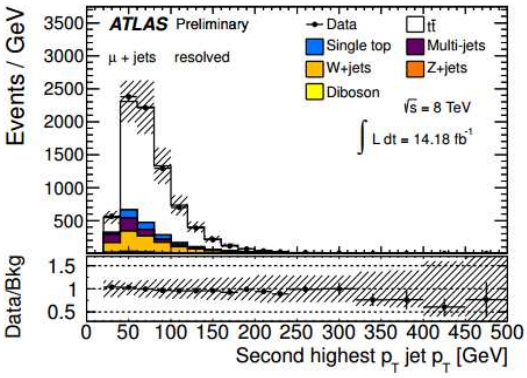

(d) Second jet p_T, muon channel

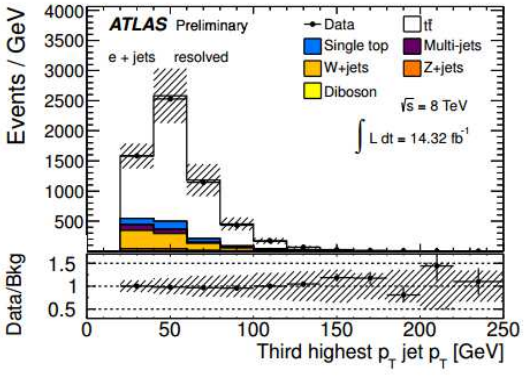

(e) Third jet p_T, electron channel

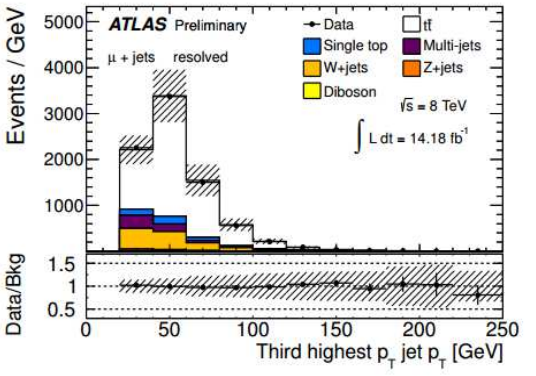

(f) Third jet p_T, muon channel

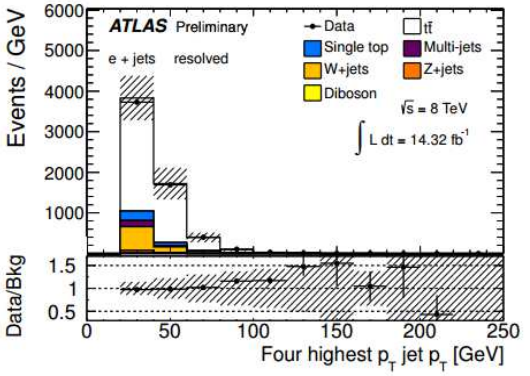

(g) Fourth jet p_T, electron channel

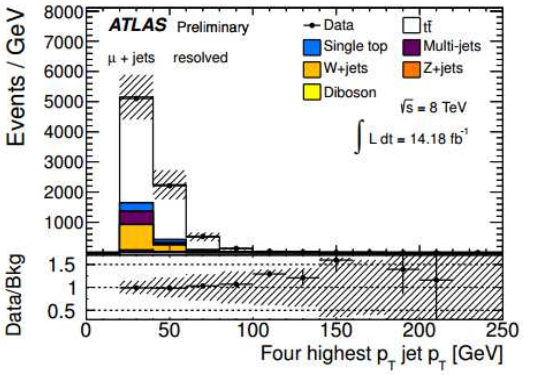

(h) Fourth jet p_T, muon channel

Figure 4.25: Small-R jet p_T, resolved selection.

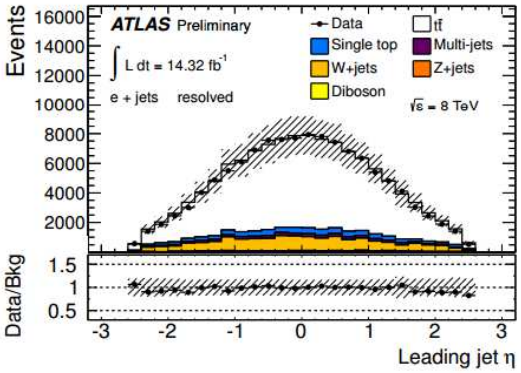

(a) Leading jet η, electron channel

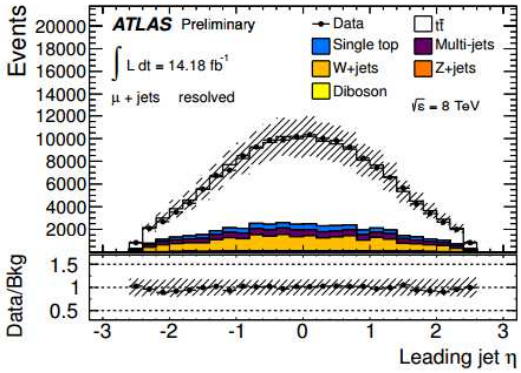

(b) Leading jet η, muon channel

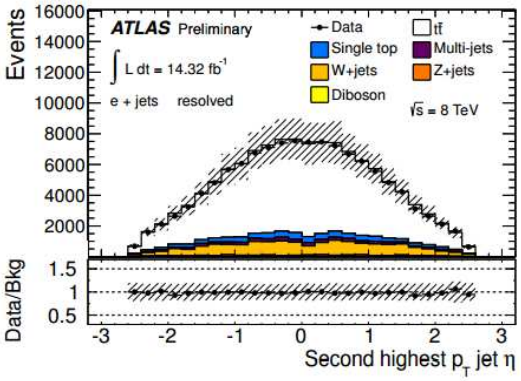

(c) Second jet η, electron channel

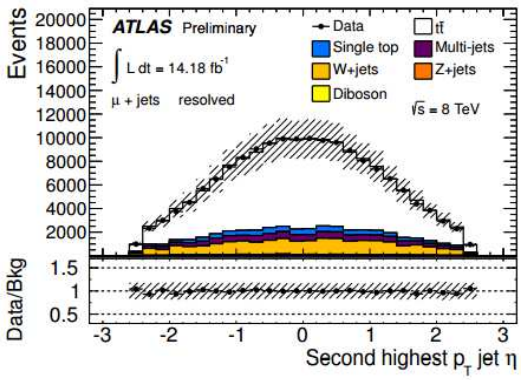

(d) Second jet η, muon channel

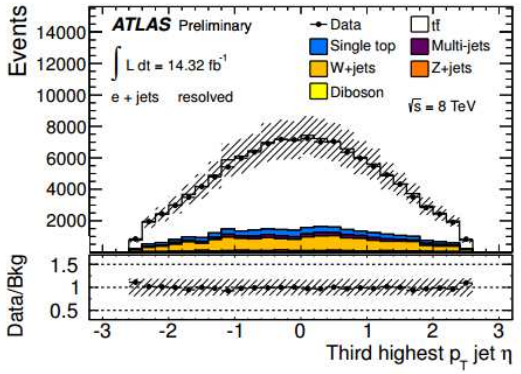

(e) Third jet η, electron channel

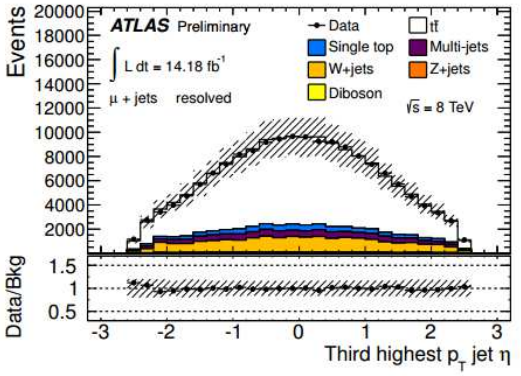

(f) Third jet η, muon channel

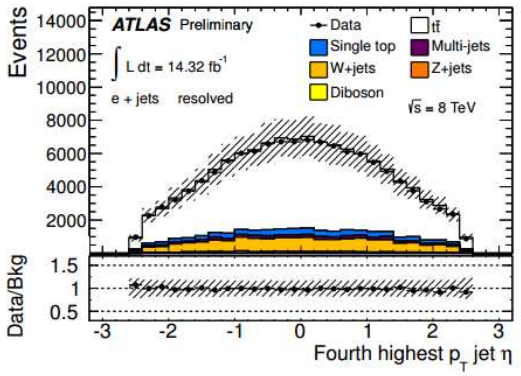

(g) Fourth jet η, electron channel

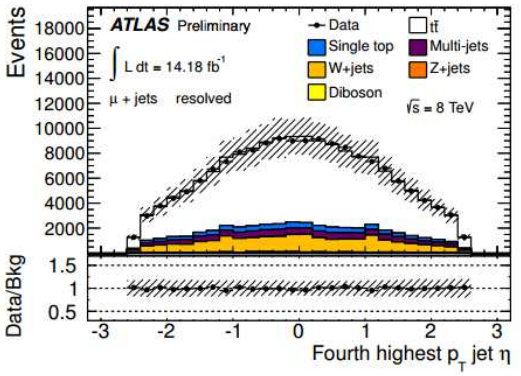

(h) Fourth jet η, muon channel

Figure 4.26: Small-R jet η, resolved selection.

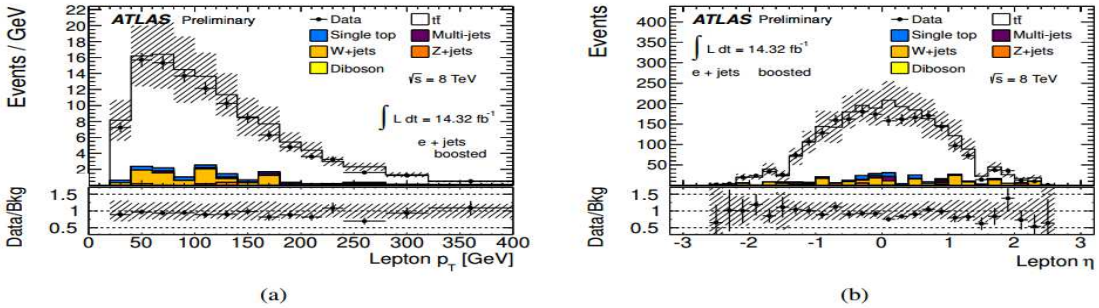

(a) (b)

Figure 4.27: Lepton kinematics in the boosted selection, electron channel.

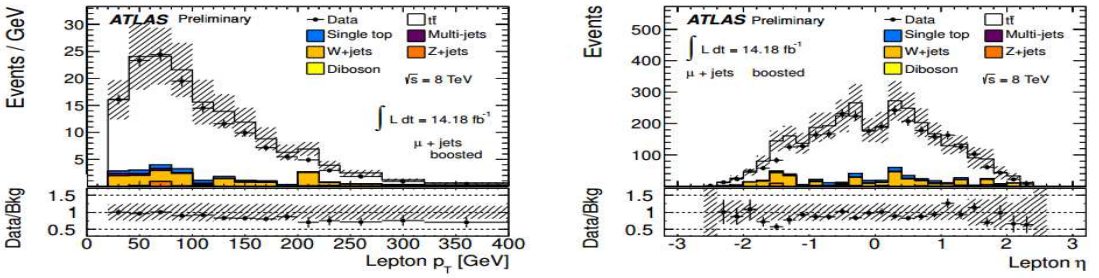

(a) (b)

Figure 4.28: Lepton kinematics in the boosted selection, muon channel.

4.5.2 Boosted Selection

The data is compared to expectations for the boosted selection in Figures 4.27-4.35. The comparisons are shown for lepton kinematics in Figures 4.27 and 4.28, E_T^{miss} in Figure 4.29 and M_T in Figure 4.30. Furthermore, the reconstructed top mass is shown in Figure 4.31 and jet multiplicity in Figure 4.32. The distance ΔR between the lepton and the closest jet is shown in Figure 4.33. Finally the kinematics of the jets are shown in Figure 4.34 and $\sqrt{d12}$ for the large-R jet in Figure 4.35. In general, the agreement in shapes between the data and expectation is satisfactory, however there is a deficit of around 10% in data with respect to the expectations

4.6 Systematic uncertainties

The many sources of systematic uncertainties in this analysis are described in this section.

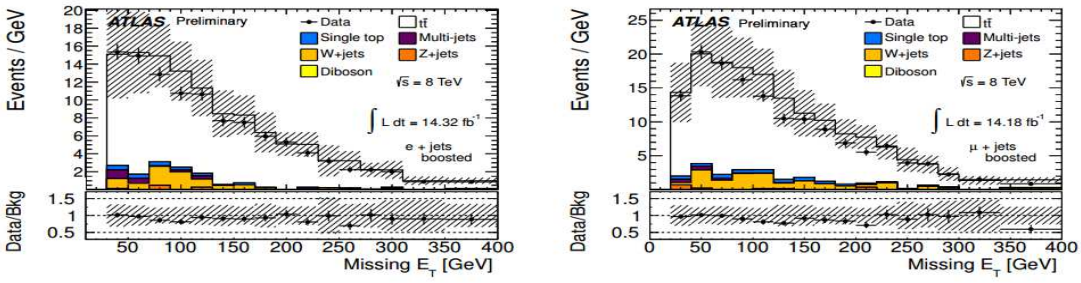

(a) Electron channel (b) Muon channel

Figure 4.29: Missing transverse momentum in the boosted selection.

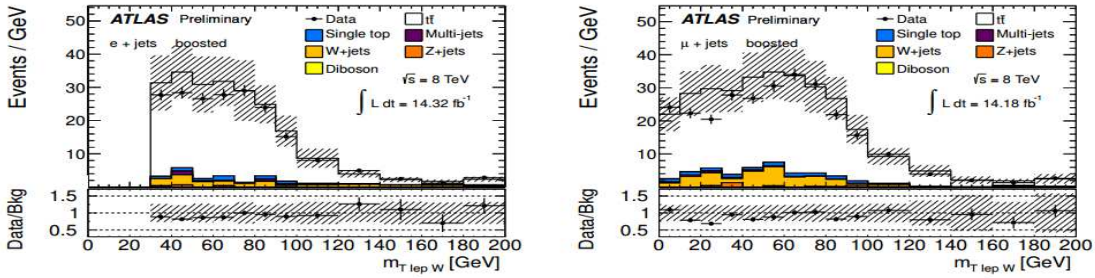

(a) Electron channel (b) Muon channel

Figure 4.30: Transverse mass in the boosted selection.

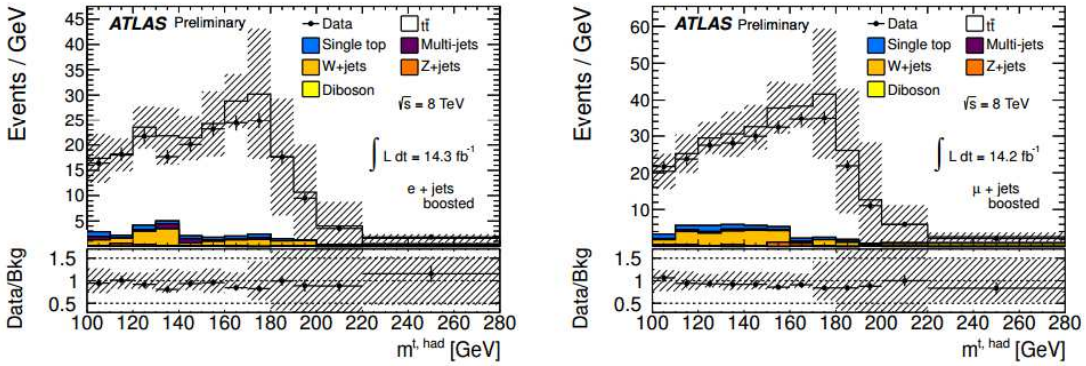

(a) Mass of the hadronically decaying top, electron channel (b) Mass of the hadronically decaying top, muon channel

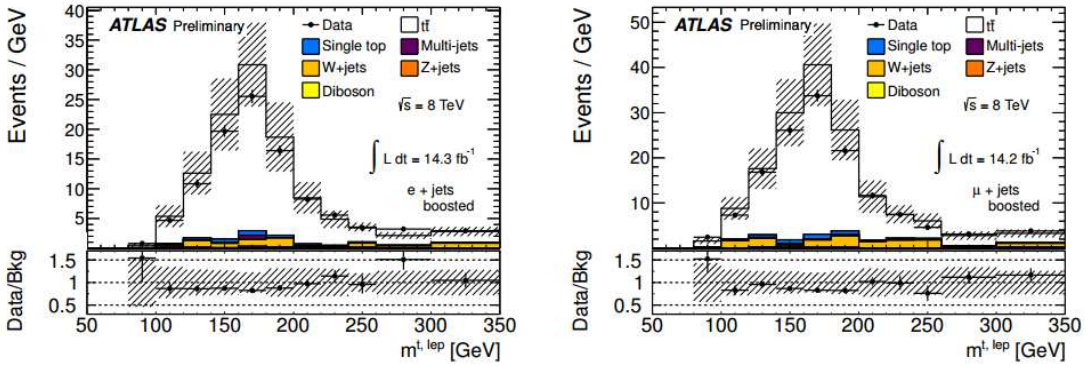

(c) Mass of the leptonically decaying top, electron channel (d) Mass of the leptonically decaying top, muon channel

Figure 4.31: Reconstructed top mass in the boosted selection.

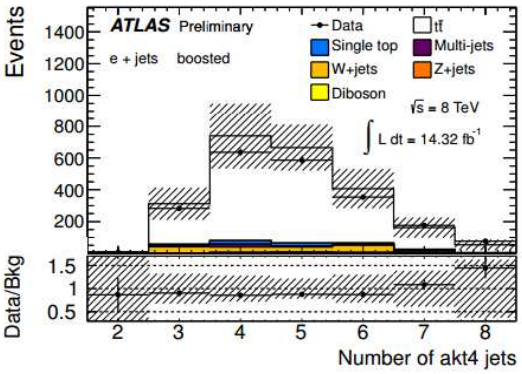

(a) Small-R jet multiplicity, electron channel

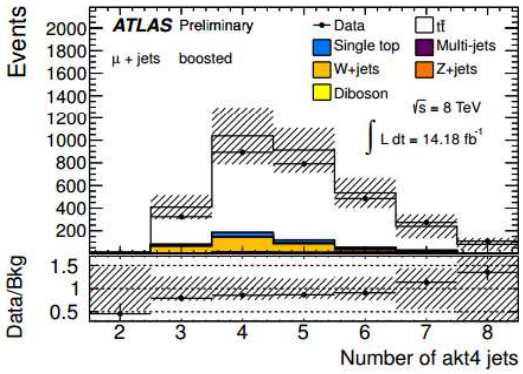

(b) Small-R jet multiplicity, muon channel

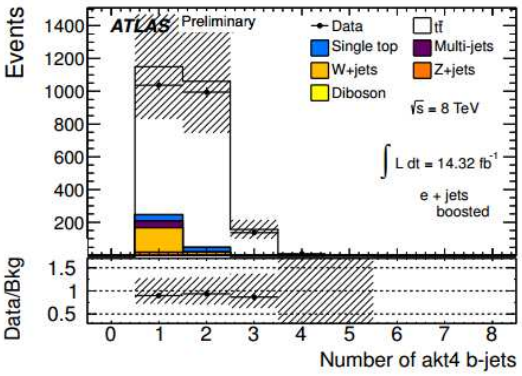

(c) b-jet multiplicity, electron channel

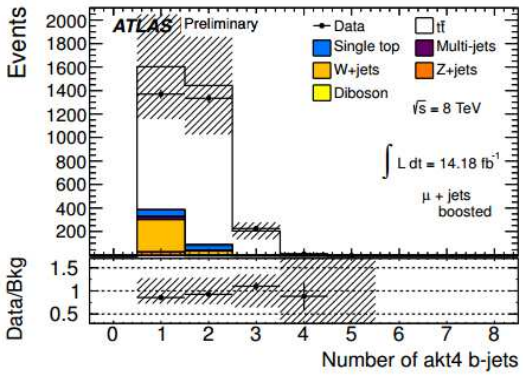

(d) b-jet multiplicity, muon channel

Figure 4.32: Small-R jet and b-jet multiplicity, boosted selection.

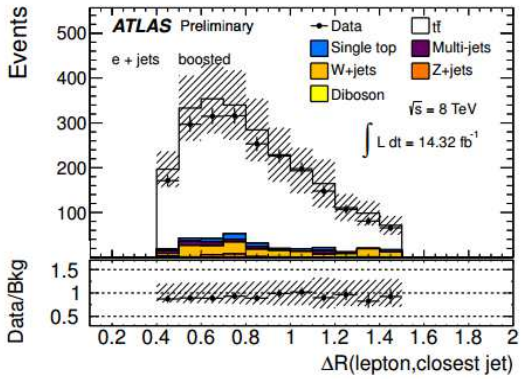

(a) Electron channel

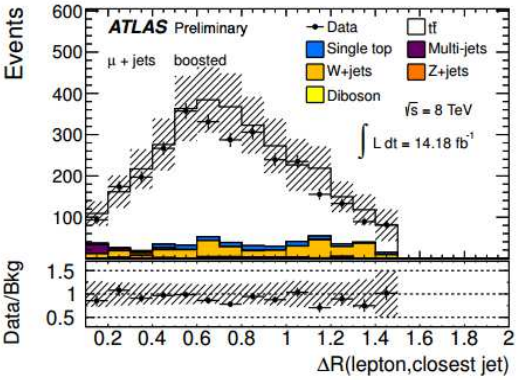

(b) Muon channel

Figure 4.33: Distance between the lepton and the closest small-R jet, boosted selection.

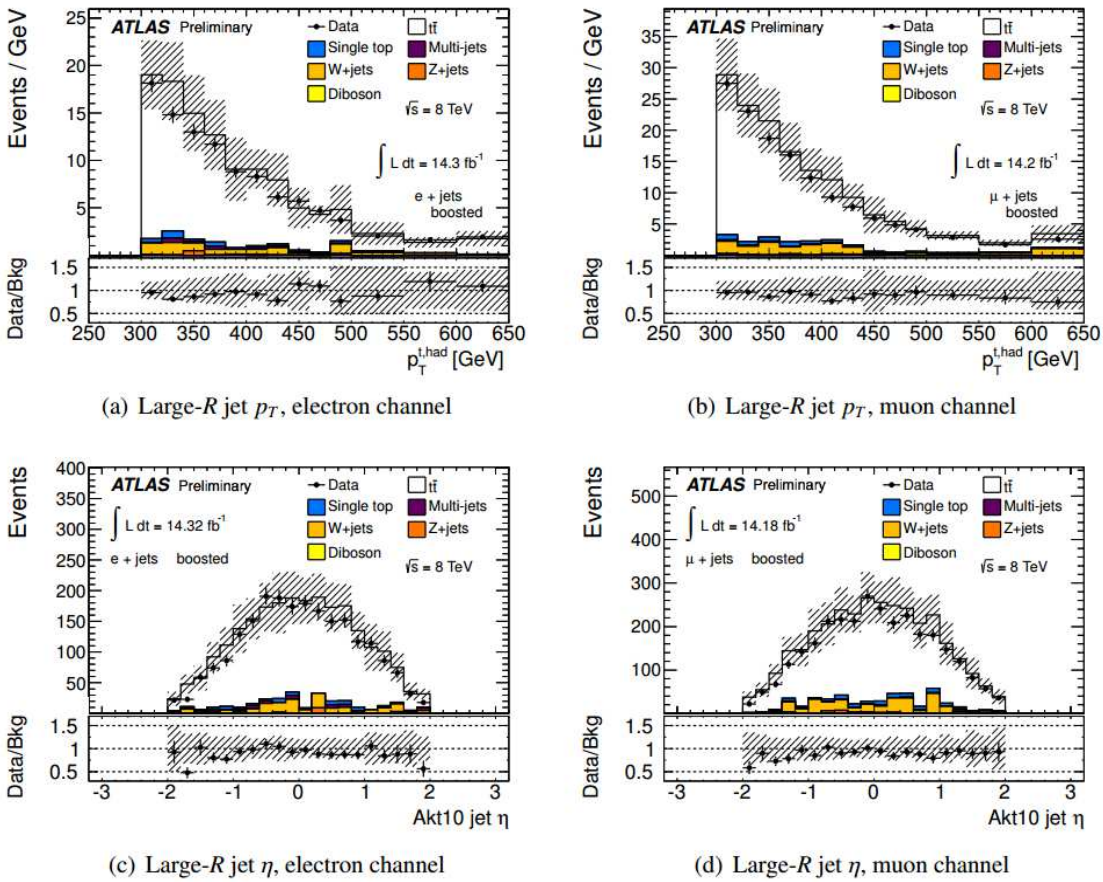

(a) Large-R jet p_T, electron channel

(b) Large-R jet p_T, muon channel

(c) Large-R jet η, electron channel

(d) Large-R jet η, muon channel

Figure 4.34: Jet kinematics, boosted selection.

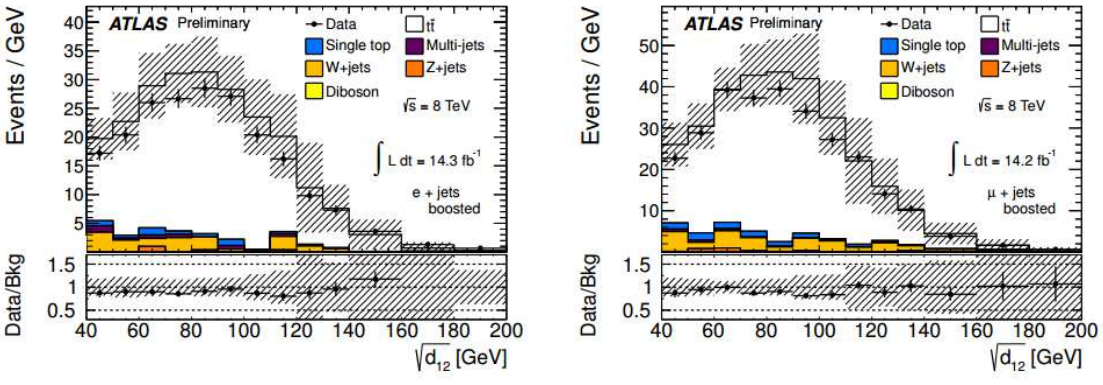

(a) Electron channel

(b) Muon channel

Figure 4.35: Large-R jet $\sqrt{d12}$ in the boosted selection

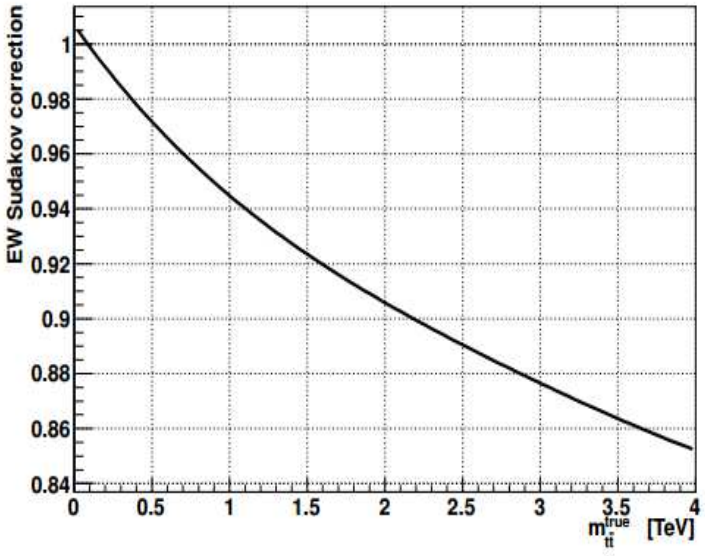

Figure 4.36: Scale factors for the electroweak virtual corrections (Sudakov corrections) as function of the true $t\bar{t}$ mass

4.7 General systematic effects

For the full 2012 data set, the total uncertainty in the luminosity is 3.6%, which is applied as a constant shift to each simulated sub-background (except the data-driven ones, i.e. multi-jets and W+jets) [95].

4.8 Systematic uncertainties in the background estimations

4.8.1 Common uncertainties

PDF Uncertainties PDF uncertainties are evaluated for all backgrounds, except for the fully data- driven non-prompt background. The uncertainties are evaluated according to the PDF4LHC recommendation [96] : combining the 68% Confidence Level (C.L.) uncertainties on the CT10, MSTW2008NLO and NNPDF2.3 [97] PDF sets. The PDF

sets used from the CTEQ and NNPDF families are newer than those in the PDF4LHC recommendation: the CT10 PDF set incoroporates the HERA combined data [98] and the NNPDF2.3 set incorporates an improved heavy-quark scheme and LHC data. A subtlety about the way these PDF uncertainties are applied lies in the treatment of the sample normalisation. In general the MC sample normalisation is derived from data or higher-order calculations and so, to avoid double counting effects on the overall normalisation, the number of events before any cuts is kept fixed when applying PDF reweighting.

4.8.2 Uncertainties affecting only $t\bar{t}$

Overall normalization The dominant normalization uncertainty on the total background is the $t\bar{t}$ cross section uncertainty of 11%. The uncertainty has been calculated at approximate Next to Next to Leading Order (NNLO) in QCD with Hathor 1.2 [99] using the MSTW2008 90% C.L. NNLO PDF sets [89] and PDF+α_S uncertainties accord- ing to the MSTW prescription [100]. Furthermore, variations from changing the top mass by $\pm$1.0 GeV are added in quadrature to the uncertainty for this analysis. These uncertainties are then added in quadrature to the normalization and factorization scale uncertainty and cross-checked (and found to be consistent) with the NLO+NNLL calculation of Ref. [101].

High-order Effect Electroweak virtual corrections (Sudakov corrections) for the true $t\bar{t}$ mass dependent scale factors are estimated as given by Manohar et al. [102]. The corrections are modeled using a parametrisation of the corrections as a function of $m_{t\bar{t}}$ provided by Manohar (Figure 4.36).

The shifted spectra are used as the one standard deviation benchmark point of this effect. Since these corrections are only the virtual corrections and it is assumed that the total correction (including the real part) is smaller, they are not used as a correction to

the central value, but as an upper limit on the possible size of the (absolute value of the) correction, and hence treated as a systematic uncertainty.

The possible variation in the shape of the $t\bar{t}$ mass spectrum from higher order QCD corrections is accounted for by applying a $m_{t\bar{t}}$ dependent weight. This weight is obtained varying the renormalization and factorization scales by a factor of two in $MC@NLO$ and fixing the normalization before cuts to be the same as the nominal scale choice. The resulting uncertainties range from 10% of the $t\bar{t}$ background at low $m_{t\bar{t}}$ to 20% at masses beyond a few TeV, we use the generation uncertainty described below.

Generation uncertainties The choice of NLO $t\bar{t}$ generator can affect the result, this possible systematic uncertainty is considered by comparing the generators $MC@NLO$ and Powheg, both using Herwig for the parton showering. The parton showering and fragmentation uncertainty is estimated through the variation of Powheg samples when the parton showering is done with PYTHIA and Herwig, respectively.

Top mass uncertainty The uncertainty on the shape of the $m_{t\bar{t}}$ distribution from the value of the top-quark mass is evaluated by comparing the shapes of samples generated with top masses of 170 and 175 GeV using $MC@NLO$ and dividing the difference by 4.0 (to approximate a 1.25 GeV uncertainty). The cross-section of the samples is treated as being the same as the nominal mass to avoid double counting the contribution of the top mass to the normalization uncertainty.

QCD I/FSR The initial- and final state QCD radiation (ISR/FSR) uncertainty is estimated as follows. AcerMC plus PYTHIA Monte Carlo samples were generated with up and down variations of the PYTHIA ISR and FSR parameters, consistent with an ATLAS measurement of $t\bar{t}$ production with a veto on additional central jet activity [103].

The 1σ up and down variations in bin i is found by computing

$$\Delta^i_{ISR/FSR} = \frac{|y^i_{up} - y^i_{down}|}{2} \frac{y^i_{nominal}}{\left(y^i_{up} - y^i_{down}\right)/2} \tag{4.10}$$

where y^i is the event yield in bin i, indexes up and down refer to the up and down variation of ISR/FSR in this bin and $y_{nominal}$ is the nominal event count as obtained from the $MC@NLO$ sample. The $\Delta_{ISR/FSR}$ variations are applied to the nominal $MC@NLO$ sample to obtain the final varied sample.

4.8.3 Uncertainties affecting only W+jets

Normalisation The normalization uncertainty on the W+jets samples stem from the uncertainty of the scale factor, which 0.89 ± 0.16 (0.95 ± 0.15) for resolved e+jets (mu+jets) and 0.65 ± 0.14 (0.81 ± 0.13) for the boosted e+jets (mu+jets), as described in Section 7.1. The normalization is based on the charge asymmetry method, which itself introduces an additional uncertainty, that is calculated through the variation of the jet energy scale, the PDF and the MC generator, after which the change in r_{MC} in Eq. 4.6 is evaluated.

Heavy Flavour content Since both the boosted and the resolved selections apply b-tagging, the heavy flavour content matters for the result, and this is not always well modeled in the simulation. The uncertainty in this modeling is taken into account through four different variations of the relative amounts of $b\bar{b}$, c and light quarks in the final state. These variations are labeled "W heavy flavor N" in Tables 4.6 and 4.7 , with N an integer between zero to three. Effect 0 models the anti-correlation between the $b\bar{b}$ and c fractions, 1 checks the overall heavy flavor versus light flavor ratio, and 2 and 3 model the relative fractions of $b\bar{b}$ and c in the 3- and 4-jet bins, respectively.

Scale and MLM matching parameter variation In addition, two shape-changing effects are considered, both correspond to parameter changes in the ALPGEN generator. They can be modeled through the variation of the relative yield of the subsamples with various number of partons. "iqopt3" varies the functional form of the factorization and renormalization scale in ALPGEN, and "ptjmin10" sets the minimum p_T of the parton in ALPGEN to 10 GeV, instead of the nominal 15 GeV. Since the normalization of the W+jets sample is data-driven, these spectra are normalized to the nominal yield times the SF's, so that only the shape change is considered. Currently we use a reweighting derived for 7 TeV analyses, no update to the official top WG prescription exists for 8 TeV.

4.8.4 Uncertainties affecting other electroweak backgrounds

The systematic uncertainties of the other electroweak backgrounds, Z+jets, single top and di-bosons, are estimated with flat scalings of the spectra, by ±48% for the Z+jets, ±7.7% for the single top, 9 and 34% for the di-boson sample, respectively. This follows the recommendations given in Ref. [104], derived from the theoretical uncertainties on the inclusive cross sections plus an extra uncertainty of 24% for each jet (anti-kt R = 0.4) that does not stem directly from a $V \to qq$ decay.

4.8.5 Uncertainties affecting the reconstructed objects

The prescription used to estimate the JES uncertainty for R = 0.4 jets is given in Ref. [105]. This tool provides the JES uncertainty for jets in multi-jet environments. It includes terms accounting for flavor composition, flavor response, close-by jets and b-JES effects.

For the boosted analysis, this procedure is expanded to include anti-kt R = 1.0 jets. This is done by simultaneously smearing the JES, mass and $\sqrt{d_{12}}$ d12 variables for these

jets according to the prescription in [106], updated in [36] using the tool described in [107].

The prescription used to estimate the Jet Energy Resolution (JER) uncertainty is given in Ref. [108]. The energy resolution can only be varied "up" (worsening of the resolution). As input to the limit setting code, a "down" shift histogram is created by symmetrizing with respect to the nominal distribution. If bin i has an x% shift in the smeared histogram, then bin i in the symmetrized "down" histogram has a -x% shift with respect to the nominal bin value.

The efficiency in the jet reconstruction in the simulation is modeled by randomly omitting a small fraction of the jets from the simulated samples. The fraction dropped ranges between 2 and 7%, depending on the pseudorapidity of the jet. This generally has a negligible effect on the background yield.

The E_T^{miss} resolution is affected by the modeling of the reconstruction of low-energetic (soft) jets and energy in clusters that are not associated with any object (cell-out). These two systematic uncertainties are fully correlated. The uncertainty originating from the pile-up modeling is covered by a 6.6% constant shift, in accordance with the recommendations.

The lepton reconstruction is connected to many sources of systematic uncertainties. We have considered the trigger SF's uncertainties, the trigger efficiency, the reconstruction efficiency and the resolution given in Ref. [89]. The dominant systematic uncertainty comes from the difference in result between the Z and the more energetic $t\bar{t}$ events, which are the bulk of the selected events. In the e+jets channel, this difference is evaluated comparing results from a di-lepton $t\bar{t}$ sample. In the μ+jets channel, this approach can not be used, since non-isolated muons are too loosely selected to give a pure $t\bar{t}$ sample. Instead the systematic uncertainty is evaluated using the deviation between the result from an inclusive Z+jets sample and on a sample of Z plus at least three jets. This systematic uncertainty is

p_T dependent and smaller than 0.8% (0.7%) for the e+jets (μ+jets) channel. An additional systematic uncertainty is derived by changing the window size from 5 GeV to 20 GeV (impact lower than 0.3% and 0.15% for the μ+jets and e+jets channels, respectively).

The prescription for implementing the b-tagging uncertainty recommended by the ATLAS performance b-group has been followed. Invariant mass spectra variations were produced by simultaneously varying the b-jet efficiency (and inefficiency) SF's in all p_T, η bins by 1σ. Additional mass spectra variations were also produced for the c-jet efficiency (and inefficiency) and mis-tag rate efficiency (and inefficiency). These mass spectra were then used as three separate up and down variations in the limit setting procedure. One modification is that for true b-jets and c-jets, the uncertainties were increased in the $p_T >$ 200 GeV jet bins by introducing an additional term in quadrature to the uncertainties in the last $140 < p_T < 200$ GeV bin (b-jets) and the last-but-one $90 < p_T < 140$ GeV bin (c-jets). The additional uncertainties are listed in Table 4.5.

jet-p_T [GeV]	200-300	300-500	800-1200	
b SF	0.11	0.12	0.33	0.27
c SF	0.16	0.17	0.27	0.30
mistag SF	-	-	-	0.58

Table 4.5: *Additional b-tagging SF uncertainties for high-p_T jets.*

4.8.6 Summary of the impact of the systematic uncertainties

In Tables 4.6 and 4.7, the shifts caused by each systematic effect on the total background yield, as well as on the individual sub-backgrounds and one benchmark signal are given, for the resolved and the boosted selections respectively.

Systematic effect	tot.bgr	$t\bar{t}$	sing.top	W+jets	multi-jet	Z+jets	Di-bosons	$Z\prime$ 1.5 TeV
Luminosity	2.9	3.6	3.6	0.0	0.0	3.6	3.6	3.6
ISR/FSR	0.2	0.2	0.0	0.0	0.0	0.0	0.0	0.0
PDF	2.9	2.9	5.1	3.0	0.0	4.4	2.0	4.6
$t\bar{t}$ norm	7.6	10.2	0.0	0.0	0.0	0.0	0.0	0.0
$t\bar{t}$ generator	1.5	2.0	0.0	0.0	0.0	0.0	0.0	0.0
W+jets norm	2.1	0.0	0.0	15.4	0.0	0.0	0.0	0.0
W shape ptjmin10	0.0	0.0	0.0	0.0	0.0	0.0	0.0	0.0
W shape iqopt3	0.0	0.0	0.0	0.0	0.0	0.0	0.0	0.0
W+jets $b\bar{b}$ + $c\bar{c}$ + c vs. light	0.8	0.0	0.0	6.1	0.0	0.0	0.0	0.0
W+jets $b\bar{b}$+25%	0.2	0.0	0.0	1.7	0.0	0.0	0.0	0.0
W+jets c+25%	1.1	0.0	0.0	7.7	0.0	0.0	0.0	0.0
Multi-jets norm, e+jets	0.6	0.0	0.0	0.0	13.0	0.0	0.0	0.0
Multi-jets norm, μ+jets	1.8	0.0	0.0	0.0	37.0	0.0	0.0	0.0
JES0	5.7	4.9	7.7	11.1	0.0	12.0	11.4	2.1
JES1	2.0	1.7	3.0	3.6	0.0	5.6	4.2	0.7
BoostedJES0	0.3	0.3	0.1	0.2	0.0	0.2	0.1	3.6
BoostedJES1	0.0	0.0	0.0	0.0	0.0	0.0	0.0	2.0
BoostedJES2	0.0	0.0	0.0	0.0	0.0	0.1	0.0	0.1
JER0	1.6	0.2	2.4	8.2	0.0	11.1	9.2	0.2
JER1	0.2	0.1	0.1	0.4	0.0	3.1	0.4	0.3
JER2	0.0	0.0	0.0	0.1	0.0	0.1	0.0	0.1
Parton shower	4.5	6.1	0.0	0.0	0.0	0.0	0.0	0.0
Jet vertex fraction	1.7	1.7	1.7	2.6	0.0	2.6	2.2	2.3
c-tag	1.4	0.3	0.4	7.6	0.0	5.6	8.8	0.3
Mistag	0.7	0.2	0.3	4.0	0.0	4.6	3.3	0.3
b-tag	4.3	4.9	5.7	2.4	0.0	3.1	1.9	1.8
Electron scale factor	1.0	1.1	1.1	1.0	0.0	1.2	1.0	1.1
Muon scale factor	1.5	1.5	1.5	1.6	0.0	1.4	1.6	1.5
EW Sudakov	2.2	2.9	0.0	0.0	0.0	0.0	0.0	0.0
topmass	1.8	2.4	0.0	0.0	0.0	0.0	0.0	0.0

Table 4.6: *Resolved selection - Impact of the various systematic effects on the background yield and on the estimated yield of a $Z\prime$ with m = 1.5 TeV. The shift is given in percent of the nominal value. Only the systematic uncertainties that enter in the limit calculation are displayed.*

Systematic effect	tot.bgr	$t\bar{t}$	sing.top	W+jets	multi-jet	Z+jets	Di-bosons	$Z\prime$ 1.5 TeV
Luminosity	3.3	3.6	3.6	0.0	0.0	3.6	3.6	3.6
ISR/FSR	0.7	0.8	0.0	0.0	0.0	0.0	0.0	0.0
PDF	5.8	5.8	7.2	6.3	0.0	8.7	6.6	2.9
$t\bar{t}$ norm	8.8	10.2	0.0	0.0	0.0	0.0	0.0	0.0
$t\bar{t}$ generator	1.6	1.9	0.0	0.0	0.0	0.0	0.0	0.0
W+jets norm	1.0	0.0	0.0	12.2	0.0	0.0	0.0	0.0
W shape ptjmin10	0.0	0.0	0.0	0.0	0.0	0.0	0.0	0.0
W shape iqopt3	0.0	0.0	0.0	0.0	0.0	0.0	0.0	0.0
W+jets $b\bar{b}$ + $c\bar{c}$ + c vs. light	1.0	0.0	0.0	12.4	0.0	0.0	0.0	0.0
W+jets $b\bar{b}$+25%	0.4	0.0	0.0	5.2	0.0	0.0	0.0	0.0
W+jets c+25%	0.6	0.0	0.0	7.1	0.0	0.0	0.0	0.0
Multi-jets norm, e+jets	0.3	0.0	0.0	0.0	27.5	0.0	0.0	0.0
Multi-jets norm, μ+jets	0.3	0.0	0.0	0.0	22.5	0.0	0.0	0.0
JES0	0.7	0.6	1.5	1.3	0.0	3.0	0.9	0.5
JES1	0.2	0.4	0.5	0.6	0.0	2.5	3.9	0.2
BoostedJES0	16.4	16.8	16.7	13.9	0.0	16.6	32.8	2.9
BoostedJES1	0.5	0.4	0.6	0.9	0.0	0.0	0.0	1.6
BoostedJES2	0.1	0.1	0.1	0.0	0.0	6.3	0.0	0.1
JER0	0.6	0.2	2.0	9.4	0.0	10.6	13.3	0.6
JER1	0.1	0.2	0.0	0.3	0.0	6.1	0.0	0.1
JER2	0.1	0.1	1.5	0.9	0.0	1.9	9.0	0.2
Parton shower	4.1	4.7	0.0	0.0	0.0	0.0	0.0	0.0
Jet vertex fraction	2.1	2.1	2.1	2.0	0.0	2.7	2.1	2.4
c-tag	0.7	0.2	0.1	6.3	0.0	0.4	10.4	0.9
Mistag	0.7	0.2	0.0	6.0	0.0	0.1	2.1	0.1
b-tag	3.4	3.4	2.8	4.3	0.0	0.8	0.7	5.9
Electron scale factor	1.0	1.0	1.0	0.8	0.0	0.8	1.4	1.0
Muon scale factor	1.6	1.6	1.6	1.7	0.0	1.7	1.2	1.6
EW Sudakov	4.4	5.1	0.0	0.0	0.0	0.0	0.0	0.0
topmass	1.3	1.5	0.0	0.0	0.0	0.0	0.0	0.0

Table 4.7: *Boosted selection - Impact of the various systematic effects on the background yield and on the estimated yield of a $Z\prime$ with m = 1.5 TeV. The shift is given in percent of the nominal value. Only the systematic uncertainties that enter in the limit calculation are displayed.*

Chapter 5

Results

The results are evaluated in two steps: first the compatibility with the SM-only hypothesis is evaluated, and then, in the absence of deviations, upper cross section limits for the two generic signal types are computed.

After the reconstruction of the $t\bar{t}$ mass spectrum, the data and simulation distributions are compared to search for hints of new physics in the form of bumps or dips in the spectrum. The reconstructed $t\bar{t}$ mass spectra are shown in Figure 5.1, for interest the sum of the spectra for all channels are shown in Figure 5.2. The search procedure is done systematically with BumpHunter [109], a hypothesis testing tool that searches for local data excesses or deficits compared to the expected background. With BumpHunter, the trial factors are automatically correctly taken into account.

Using BumpHunter, data and the expected background are compared in sliding windows of variable size, with a minimum width of two bins. For each spectrum, the Poisson probability of the most prominent bump or dip (i.e. the smallest probability) is saved. In each window i, the data count is d_i, the background yield is b_i and the Poisson probability $\mathrm{P}(d_i, b_i)$ is defined as

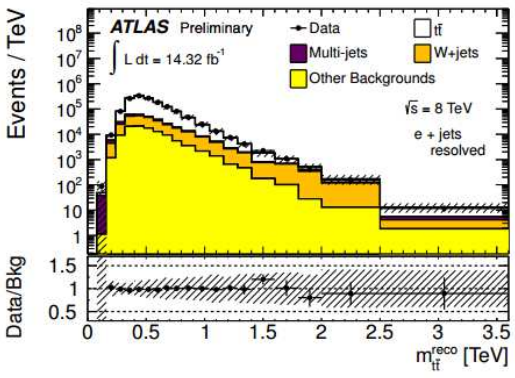

(a) Electron channel, resolved selection (*dRmin*)

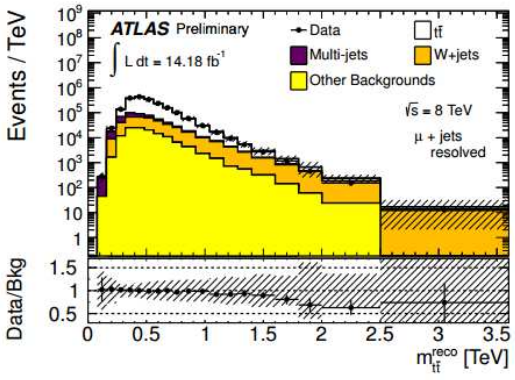

(b) Muon channel, resolved selection (*dRmin*)

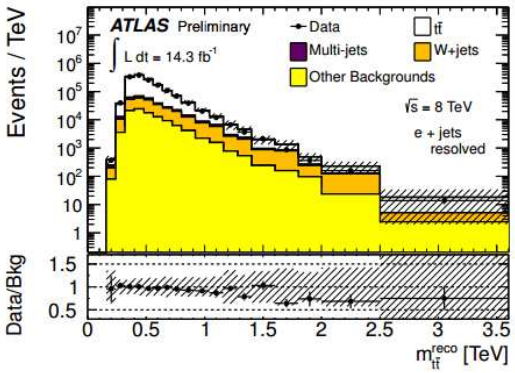

(c) Electron channel, resolved selection (χ^2)

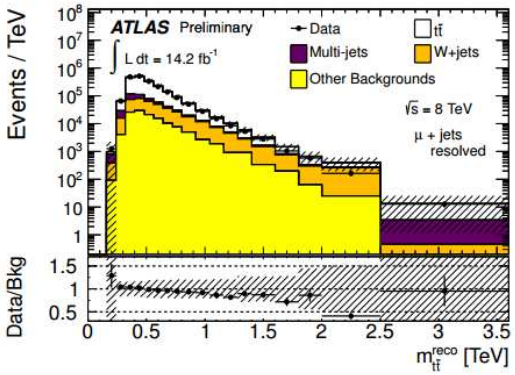

(d) Muon channel, resolved selection (χ^2)

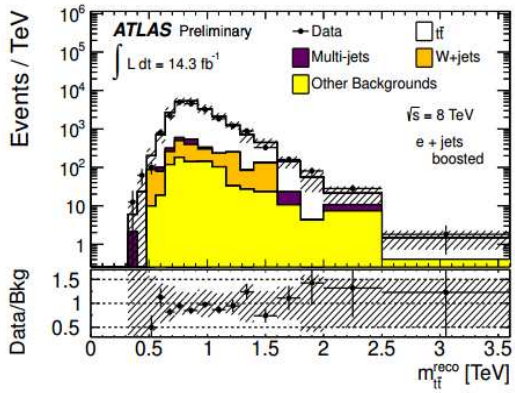

(e) Electron channel, boosted selection

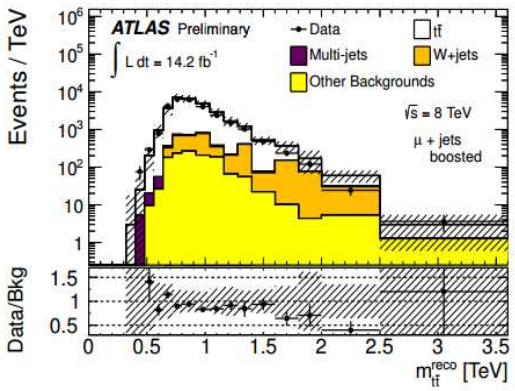

(f) Muon channel , boosted selection

Figure 5.1: The $m_{t\bar{t}}$ spectrum for the different channels.

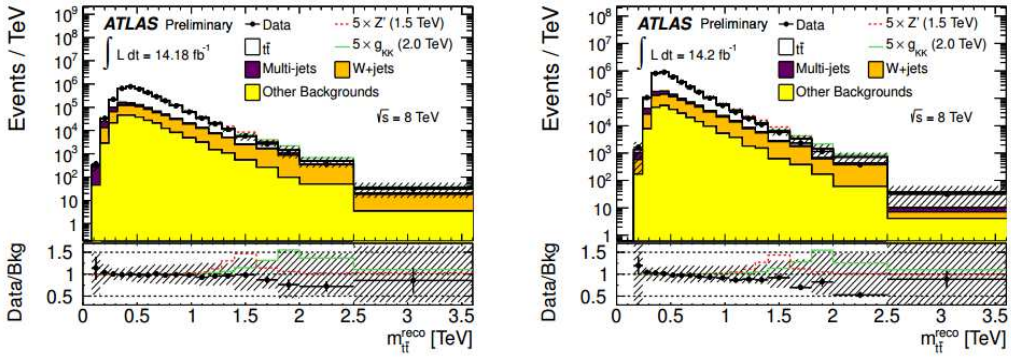

(a) Reconstructed with *dRmin* in the resolved selection. (b) Reconstructed with χ^2 in the resolved selection.

Figure 5.2: The $m_{t\bar{t}}$ distribution summed over all channels and selections for the two different resolved reconstruction options.

$$P(d_i, b_i) = \begin{cases} \Gamma(d_i, b_i) = \sum_{n=d_i}^{\infty} \frac{b_i^n}{n!} & d_i \geq b_i \\ 1 - \Gamma(1 + d_i, b_i) & d_i < b_i \end{cases} \tag{5.1}$$

when searching for an excess (the inequality signs are reversed when looking for deficits). Γ is the Gamma function. The smallest P(d_i, b_i) from all the windows, P_i^{min} corresponds to the most interesting (discrepant) window. The BumpHunter test statistic t is computed as

$$t = \begin{cases} \Gamma(d_i, b_i) = 0 & d_i \geq b_i \\ -log(P_i^{min}) & d_i < b_i \end{cases} \tag{5.2}$$

The p-value of the most interesting bump is found by comparing the test statistic from data with the test statistics found in N = 10, 000 pseudo experiments, where the pseudodata is generated by Poisson fluctuations of the expected background. The p-value is defined as

$$p - value = \frac{\int_{t_{obs}}^{\inf} f(t)}{\int_{0}^{\inf} f(t)} \tag{5.3}$$

where $f(t)$ is the distribution of the test statistic values from the pseudodata and t_{obs} is the test statistic obtained from data. A p-value of 0 means that no deviation was observed in the pseudoexperiments that is bigger than the one obtained in data, i.e. the deviation is very large. Data has been divided into four distinct channels, e+jets resolved, μ+jets resolved, e+jets boosted and μ+jets boosted. In addition we also have the case where an event has been reconstructed both as resolved and boosted (the overlap region), in which case it is reconstructed with the boosted technique and included in that sample. There is no overlap in the events between the two categories after this procedure. The results of the channel combination can be done in two ways: adding the spectra or searching for overlaps. In the first case, the spectra are simply added, and the search is made as usual. The second case is slightly more sophisticated, and is based on the fact that if a $t\bar{t}$ resonance exists, bumps will arise in the various spectra at approximately the same mass point. In this case, the most interesting windows found, for each channel, are compared. If they do not overlap, it is called "no signal". If they overlap, the combined probability, to observe a larger data count, is taken as the product of the individual probabilities, from which the BumpHunter test statistic is computed. The test statistic obtained from data is then compared with pseudo experiments, conducted under the same conditions. In Table 5.1, the p-values and mass ranges of the most interesting deviations are listed, as well as the corresponding significance in sigmas, for statistical errors only. Significances when taking the various systematic uncertainties into account can be found in Table 5.2, 5.3 and 5.4. In order to avoid fake bumps and dips created by a normalization shift, the yield of the

expected distribution has been normalized to the data count before the comparison.

5.1 Upper production cross section limits on $t\bar{t}$ resonances

As shown in the previous section, no significant data excess over the expected SM background is found, and we proceed to set upper limits on the production cross section of our benchmark models. Upper cross section limits are set on the existence of the benchmark models using a Bayesian technique, implemented in a tool developed by the $D\emptyset$ collaboration [110]. The $D\emptyset$ tool defines the likelihood L_ν for a particular resonance mass ν as

$$L_\nu(D|\sigma_\nu, a_\nu, b) = \prod_{i=1}^{N} \frac{e^{-(a_{\nu,i}+b_i)}(a_{\nu,i}+b_i)^{D_i}}{\Gamma(D_i+1)} \tag{5.4}$$

where D is the number of data events, b is the sum of all expected backgrounds, σ_ν is the signal cross section for mass ν and a_ν is the acceptance times luminosity for the signal. The index i runs over all the bins of all spectra in all the two or four channels. The gamma-function $\gamma(D_i+1)$ reduces to $D_i!$ if D_i is an integer. The likelihood is computed as a function of the cross section of the inserted signal. It is converted into a posterior probability, $p(\sigma, a, b|D)$, using Bayes' theorem. The prior is flat, and non-zero only for positive cross sections. The 95% C.L. upper limit is found by integrating the posterior probability to 95%. The systematic uncertainties are included by randomly sampling each effect from a Gaussian function (or a lognormal function if the relative uncertainty exceeds 20%). For each of the models investigated, 95% C.L. upper limits on the cross section times the $t\bar{t}$

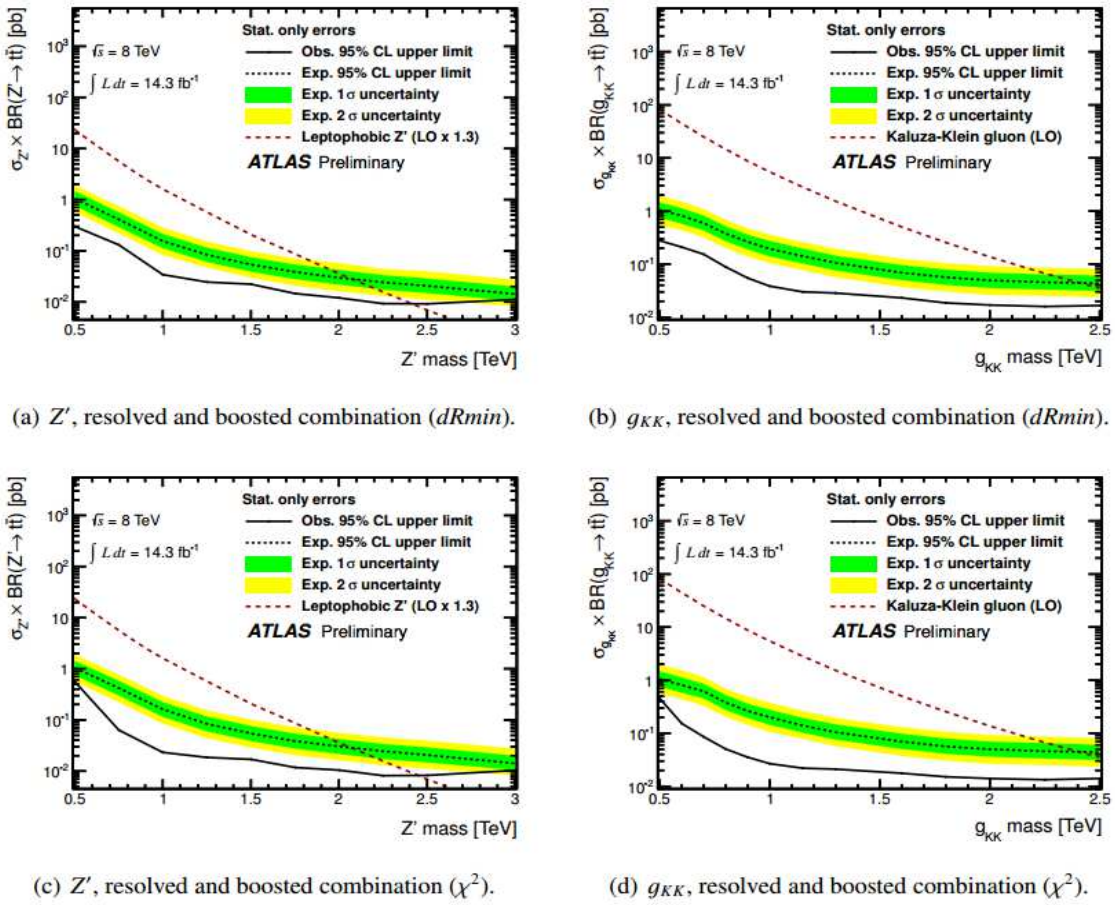

(a) Z', resolved and boosted combination (*dRmin*).

(b) g_{KK}, resolved and boosted combination (*dRmin*).

(c) Z', resolved and boosted combination (χ^2).

(d) g_{KK}, resolved and boosted combination (χ^2).

Figure 5.3: Expected and observed upper cross section limits times the $t\bar{t}$ branching ratio on (a,c) $Z\prime$ and (b,d) Kaluza-Klein gluons considering statistical uncertainties only.

branching ratio is set. Figure 5.3 shows the upper cross section limits including statistical uncertainties only. Figure 5.4 shows the upper cross section limits including systematic and statistical uncertainties. In the high $m_{t\bar{t}}$ region the observed limit moves from below the expected limit in the "statistical uncertainties only" plot, to above the expected limit in the "systematic and statistical uncertainty" plot. This is due to constraints from the low $m_{t\bar{t}}$ that propagate to the high $m_{t\bar{t}}$ region.

5.2 Posterior probabilities from limit setting

For each systematic uncertainty a set of Gaussian random numbers are sampled. The mean of this Gaussian distribution is 0 and the RMS is 1. Figure 5.5 shows the mean and

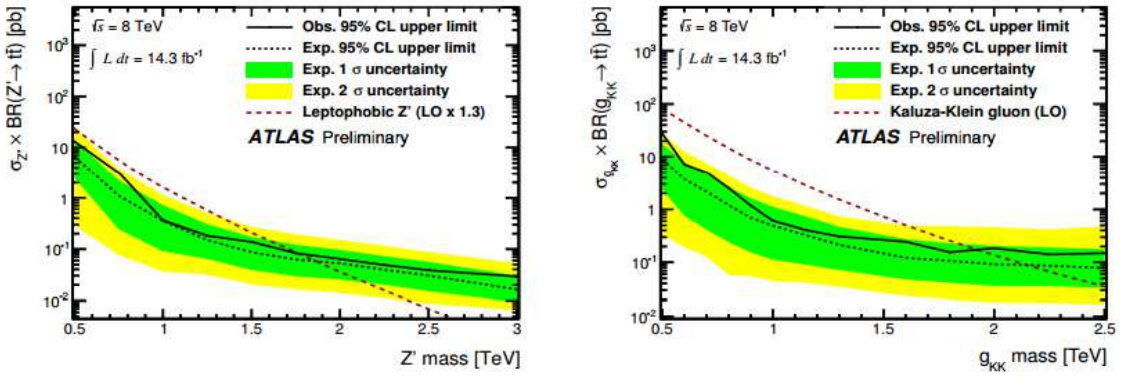

(a) Z', resolved and boosted combination (*dRmin*).

(b) g_{KK}, resolved and boosted combination (*dRmin*).

(c) Z', resolved and boosted combination (χ^2).

(d) g_{KK}, resolved and boosted combination (χ^2).

Figure 5.4: Expected and observed upper cross section limits times the $t\bar{t}$ branching ratio on (a,c) $Z\prime$ and (b,d) Kaluza-Klein gluons. Systematic and statistical uncertainties are considered.

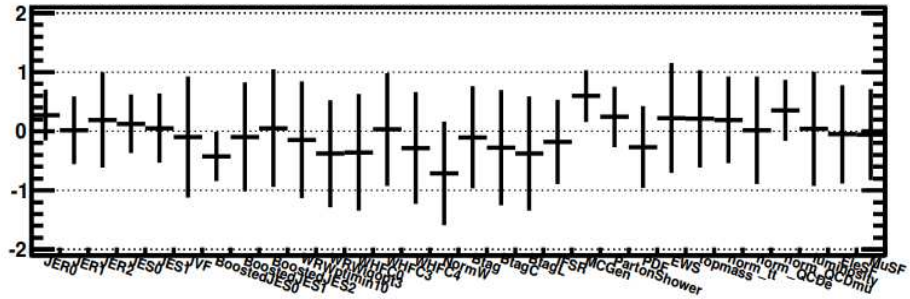

(a) Observed posteriors. Combined limits with the χ^2 method used in the resolved selection

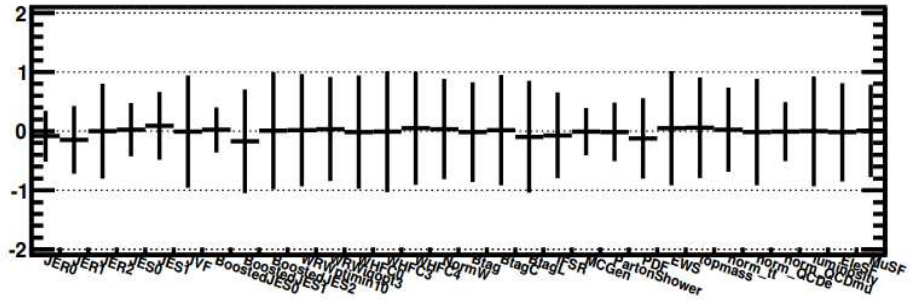

(b) Mean and RMS of the expected-observed posterior probability distributions, Combined limits with the χ^2 method used in the resolved selection.

Figure 5.5: Mean and RMS of the observed and expected-observed posterior probability distributions, Z' 1.75 TeV.

RMS of the corresponding posterior probability distributions, for oberved-expected[1] limits evaluated at the $Z\prime$ masses 1.75 TeV. The systematic uncertainty in each case is taken as the parameter of interest. All the other parameters are integrated over to obtain the marginalized posterior probability distribution for the given systematic shift. This shows the extent to which the data prefer (or pseudodata is able to prefer) particular values of the nuisance parameters associated with individual systematics.

[1]Observed-expected posteriors are obtained by using a pseudodata sample composed of the central background expectation only in the limit setting.

Excesses			
Channel	p-value	σ(low, high)	mass range (GeV)
resolved e	0.2174 ± 0.0013	0.7810 (0.7765,0.7854)	240 - 400
resolved mu	0.0000 ± 0.0000	> 5	240 - 480
boosted e	0.5000 ± 0.0016	No Excess	1800 - 3600
boosted mu	0.1797 ± 0.0012	0.9163 (0.9117,0.9210)	400 - 560
all added	0.0000 ± 0.0000	> 5	240 - 480
combined	1.0000 ± 0.0000	No Excess	0 - 0
Deficits			
Channel	p-value	σ(low, high)	mass range (GeV)
resolved e	0.0000 ± 0.0000	> 5	720 - 1160
resolved mu	0.0000 ± 0.0000	> 5	1040 - 1280
boosted e	0.0000 ± 0.0000	> 5	640 - 1160
boosted mu	0.0000 ± 0.0000	> 5	920 - 2000
all added	0.0000 ± 0.0000	> 5	720 - 920
combined	0.0000 ± 0.0000	> 5	920 - 2000

Table 5.1: *Impact of the various systematic effects on the background yield and on the estimated yield of a Z′ with m = 1.5 TeV. The shift is given in percent of the nominal value. Only the systematic uncertainties that enter in the limit calculation are displayed. Boosted selection.*

Excesses			
Channel	p-value	σ(low, high)	mass range (GeV)
resolved e	0.0002 ± 0.0000	3.5827 (3.5256,3.6546)	240 - 480
resolved mu	0.0000 ± 0.0000	> 5	240 - 480
boosted e	0.1657 ± 0.0012	0.9715 (0.9667,0.9762)	1160 - 1400
boosted mu	0.0023 ± 0.0002	2.8352 (2.8147,2.8569)	400 - 720
all added	0.0000 ± 0.0000	> 5	240 - 480
combined	1.0000 ± 0.0000	No Excess	0 - 0
Deficits			
Channel	p-value	σ(low, high)	mass range (GeV)
resolved e	0.0000 ± 0.0000	> 5	800 - 1800
resolved mu	0.0000 ± 0.0000	> 5	2000 - 3600
boosted e	0.7772 ± 0.0013	No Deficit	640 - 920
boosted mu	0.0012 ± 0.0001	3.0307 (3.0044,3.0592)	1600 - 2500
all added	0.0000 ± 0.0000	> 5	920 - 1160
combined	1.0000 ± 0.0000	No Deficit	0 - 0

Table 5.2: *The most significant deviations found in the $t\bar{t}$ mass spectra, considering only statistical uncertainties, electron and muon channels separately, added, and combined. The background yield has been normalised to the data count.*

Excesses			
Channel	p-value	σ(low, high)	mass range (GeV)
resolved e	0.0682 ± 0.0025	1.4893 (1.4704,1.5088)	240 - 400
resolved mu	0.0154 ± 0.0012	2.1596 (2.1289,2.1926)	240 - 400
boosted e	0.6715 ± 0.0047	No Excess	1800 - 2500
boosted mu	0.8570 ± 0.0035	No Excess	400 - 560
all added	0.0266 ± 0.0016	1.9333 (1.9078,1.9601)	240 - 400
combined	1.0000 ± 0.0000	No Excess	0 - 0
Deficits			
Channel	p-value	σ(low, high)	mass range (GeV)
resolved e	0.7065 ± 0.0046	No Deficit	1600 - 2000
resolved mu	0.9976 ± 0.0005	No Deficit	2000 - 3600
boosted e	0.3868 ± 0.0049	0.2877 (0.2750,0.3004)	1400 - 1800
boosted mu	0.8756 ± 0.0033	No Deficit	2000 - 3600
all added	0.7572 ± 0.0043	No Deficit	1600 - 2500
combined	1.0000 ± 0.0000	No Deficit	0 - 0

Table 5.3: *The most significant deviations found in the $t\bar{t}$ mass spectra, considering both systematic and statistical uncertainties, electron and muon channels separately and added.*

Excesses			
Channel	p-value	σ(low, high)	mass range (GeV)
resolved e	0.0229 ± 0.0015	1.9972 (1.9704,2.0256)	240 - 400
resolved mu	0.0690 ± 0.0025	1.4833 (1.4645,1.5026)	240 - 400
boosted e	0.6576 ± 0.0047	No Excess	1800 - 2500
boosted mu	0.8526 ± 0.0035	No Excess	400 - 560
all added	0.0349 ± 0.0018	1.8132 (1.7899,1.8375)	240 - 400
combined	1.0000 ± 0.0000	No Excess	0 - 0
Deficits			
Channel	p-value	σ(low, high)	mass range (GeV)
resolved e	0.7029 ± 0.0046	No Deficit	1600 - 2000
resolved mu	0.9996 ± 0.0002	No Deficit	2000 - 3600
boosted e	0.3078 ± 0.0046	0.5021 (0.4890,0.5153)	1400 - 1800
boosted mu	0.8819 ± 0.0032	No Deficit	2000 - 3600
all added	1.0000 ± 0.0000	No Deficit	2000 - 3600
combined	1.0000 ± 0.0000	No Deficit	0 - 0

Table 5.4: *The most significant deviations found in the $t\bar{t}$ mass spectra, considering both systematic and statistical uncertainties, electron and muon channels separately and added. The background yield has been normalised to the data count*

Chapter 6

Summary and Conclusions

Searching for new physics in this new era, is both challenging and difficult. The hadron-hadron machine, with its great advantages, also makes it very difficult to obtain a "pure" signal/s conducting a study within this "hostile environment" makes one to develop new tools and approaches. While challenging, it is impotent that we conduct a methodological an generic as possible approaches for new physics searches.

In the begging of this thesis we investigate the existent of an FGB, In order conduct this task, we wrote a dedicated Monta-Carlo program in the framework of Moses and PYTHIA. Using this new MC generation and standard approaches we showed that the manifestation of an FGB particle can be detected under some parameter space. We also showed that a good and relative "Standard" approach would be to search via the $t\bar{t}$ production channel and decay products. This, is due to the Top uniquely large mass that in some extra dimensional models (such as the one we used for the FGB) can give rise to enhance coupling. Utilizing this "feature" of the theory, were the top quark interact stringer with the FGB, it is only natural that we would select this channel of the FGB decay.

Moving onwards we have joined forces with the $t\bar{t}$ resonance search within ATLAS to

perform a generic new physics search in the $t\bar{t}$ decay channel. This search, performed for the production of a generic new particles decaying to $t\bar{t}$, gave no evidence for any type of new physics. Upper limits on the possible cross-section $\times$ branching ratio for new particles have been set. These limits translate to Observed (expected) lower bounds on the allowed mass of the new particle in the benchmark scenarios of $m(Z\prime) > 1.8$ TeV (1.8 TeV) and $m(g_{KK})$ >2.0 TeV(2.2 TeV).

ATLAS collected in total 20 fb^{-1} by the end of 2012, the results of the studies conducted, contaning all data is about to be published. So far, no hint for new physics is found in the full 8 TeV data set. However, there is still strong motivation to continue the hunt for new Physics in the *tbart* channel at the Run-2 of LHC. Run-2 with center of mass energy of 13 TeV and much more data, will explore different parameter space. Sorter "time-to-market", given analysis tools and approaches have already been developed for Run-1. Only makes the motivation even stronger.

With the discovery of the Higgs boson, one can also look for a new approach and channels using the higgs data, as mention in here [117] for (different model) flavor physics in the era of the Higgs.

Chapter 7

Acknowledgments

First and foremost I wish to thank my supervisor, mentor and friend, Prof, Erez Etzion, without him this work would not be possible. I have learned a great deal over the years under his guidance and supervision, staring early from my undergrad years as a B.Sc. student through my master's and eventually Ph.D. studies. Erez has had a great positive impact on my life, and there are no words to describe my gratitude and love.

I also wish to thank all of my colleagues who are also my dear friends,

Yan Benhammou - who taught me all I need to know about computers, Linux, good friends and life.

Gideon Bella - who taught me a great deal about physics, good practice, and infinite advices I received over the years.

Meny Ben Moshe - who taught me that 5Kv wont kill me.. and also for listening when I needed a friend.

Noam Hod - who taught me all I needed to now about work excellence and programing skills.

Nir Gutmann - who taught me how to be motivated.

Yiftah Silver - who taught me that I can do better by believing in myself.

Yonathan Munwes - who taught me never to give up and how to strive to be better.

Nimrod Taiblum - who taught me be a better physicist.

Eran Greenberg - who has been my dear friend with whom I shared all the courses during my Physics studies, without his friendship it would have been impossible to reach the level of a Ph.D. candidate.

More over, I wish to thank Prof. Abner Sofer, Prof. Shmuel Nussinov for countless conversations about physics who have inspired me in countless ways.

Bibliography

[1] S. Weinberg, Phys. Rev. Lett. 19, 1264 (1967); A. Salam, p. 367 of Elementary Particle Theory, ed. N. Svartholm (Almquist and Wiksells, Stockholm, 1969); S.L. Glashow, J. Iliopoulos, and L. Maiani, Phys. Rev. D2, 1285 (1970).

[2] G. Bella, E. Etzion, N. Hod and M. Sutton, "Introduction to the MCnet Moses project and Heavy gauge bosons search at the LHC", arXiv:1004.1649

[3] T. Sjostrand, S. Mrenna, P. Skands, "A brief introduction to PYTHIA 8.1", Computer Physics Communications, ISSN 0010-4655.

[4] T. Gleisberg et al., "SHERPA 1. alpha: A Proof of concept version", arXiv:hep-ph/0311263; F. Maltoni and T. Stelzer, "MadEvent: Automatic Event Generation with MadGraph", JHEP 0302, 027 (2003) arXiv:hep-ph/0208156; T. Stelzer and W. F. Long, "MadGraph: Automatic Generation of Tree Level Helicity Amplitudes Comput". Phys. Commun. 81, 357 (1994) arXiv:hep-ph/9401258; J. Alwall et al., "MadGraph/MadEvent v4: The New Web Generation", JHEP 0709, 028 (2007) arXiv:0706.2334 hep-ph.

[5] CDF Collaboration, T. Aaltonen et al., Evidence for a Mass Dependent Forward-Backward Asymmetry in Top Quark Pair Production, Phys.Rev. D83 (2011) 112003, arXiv:1101.0034 [hep-ex].

[6] C. T. Hill, Topcolor assisted technicolor, Phys.Lett. B345 (1995) 483-489, arXiv:hep-ph/9411426 [hep-ph].

[7] R. M. Harris, C. T. Hill, and S. J. Parke, Cross section for topcolor Z'(t) decaying to t anti-t, arXiv:hep-ph/9911288.

[8] R. M. Harris and S. Jain, Cross Sections for Leptophobic Topcolor Z' decaying to top-antitop, arXiv:1112.4928 [hep-ph].

[9] B. Lillie, L. Randall, and L.T. Wang, The Bulk RS KK-gluon at the LHC, JHEP 09 (2007) 074, arXiv:hep-ph/0701166.

[10] B. Lillie, J. Shu, and T. M. P. Tait, Kaluza-Klein Gluons as a Diagnostic of Warped Models, Phys. Rev. D76 (2007) 115016, arXiv:0706.3960 [hep-ph].

[11] K. Agashe, H. Davoudiasl, G. Perez, and A. Soni, Warped Gravitons at the LHC and Beyond, Phys.Rev. D76 (2007) 036006, arXiv:hep-ph/0701186 [hep-ph].

[12] CDF Collaboration, T. Aaltonen et al., A search for resonant production of $t\bar{t}$ pairs in 4.8 fb^{-1} of integrated luminosity of pp collisions at $sqrts = 1.96$ TeV, Phys.Rev. D84 (2011) 072004, arXiv:1107.5063 [hep-ex].

[13] CDF Collaboration, T. Aaltonen et al., Search for resonant production of $t\bar{t}$ decaying to jets in $p\bar{p}$ collisions at $sqrts = 1.96$ TeV, Phys.Rev. D84 (2011) 072003, arXiv:1108.4755 [hep-ex]. 8 pages, 4 figures.

[14] CDF Collaboration, T. Aaltonen et al., Search for Resonant $t\bar{t}$ Production in the Semi-leptonic Decay Mode Using the Full CDF Data Set, arXiv:1211.5363 [hep-ex].

[15] $D\emptyset$ Collaboration, V. M. Abazov et al., Search for a Narrow $t\bar{t}$ Resonance in pp Collisions at $sqrts = 1.96$ TeV, Phys.Rev. D85 (2012) 051101, arXiv:1111.1271 [hep-ex].

[16] CMS Collaboration, S. Chatrchyan et al., Search for anomalous $t\bar{t}$ production in the highly-boosted all-hadronic final state, JHEP 1209 (2012) 029, arXiv:1204.2488 [hep-ex].

[17] CMS Collaboration, S. Chatrchyan et al., Search for resonant $t\bar{t}$ production in lepton+jets events in pp collisions at $sqrts = 7$ TeV, JHEP 1212 (2012) 015, arXiv:1209.4397 [hep-ex].

[18] CMS Collaboration, S. Chatrchyan et al., Search for Z' resonances decaying to $t\bar{t}$ in dilepton+jets final states in pp collisions at $sqrts = 7$ TeV, arXiv:1211.3338 [hep-ex]. Not reviewed, for internal circulation only April 25, 2013 - 23 : 13 DRAFT 124

[19] ATLAS Collaboration, G. Aad et al., A search for $t\bar{t}$ resonances with the ATLAS detector in 2.05 fb^{-1} of proton-proton collisions at $sqrts = 7$ TeV, Eur.Phys.J. C72 (2012) 2083, arXiv:1205.5371 [hep-ex].

[20] ATLAS Collaboration, G. Aad et al., A search for $t\bar{t}$ resonances in lepton +jets events with highly boosted top quarks collected in pp collisions at $sqrts = 7$ TeV with the ATLAS detector, arXiv:1207.2409 [hep-ex]. Submitted to JHEP.

[21] ATLAS Collaboration, G. Aad et al., Search for resonances decaying into top-quark pairs using fully hadronic decays in pp collisions with ATLAS at $sqrts = 7$ TeV, arXiv:1211.2202 [hep-ex].

[22] A search for $t\bar{t}$ resonances in the lepton plus jets final state using 4.66 fb^{-1} of pp collisions at $\sqrt{s} = 7$ TeV, Tech. Rep. ATLAS-CONF-2012-136, CERN, Geneva, Sep, 2012

[23] G. Isidori, Y. Nir and G. Perez, "Flavor Physics Constraints for Physics Beyond the Standard Model".arXiv:1002.0900v2 [hep-ph]

[24] CDF Collaboration, T. Aaltonen et al., "Measurement of the Top Pair Production Cross Section in the Dilepton Decay Channel in p anti-p Collisions at $\sqrt{s} = 1.96$ TeV" Phys.

Rev. D82, 052002 (2010). arXiv: 1002.2919; The CMS Collaboration, "CMS Physics Analysis Summary", CMS PAS TOP-11-001;The ATLAS collaboration, "Top Quark Pair Production Cross-section Measurement in ATLAS in the Single Lepton+Jets Channel Without b-tagging", ATLAS-CONF-2011-023.

[25] S. J. Lee, private communication.

[26] M. Peskin and D. Schroeder, "An Introduction to QFT", Addison Wesley 1994.

[27] J. Pumplin et al., "New Generation of Parton Distributions with Uncertainties from Global QCD Analysis", arXiv:hep-ph/0201195v3

[28] W. Wagner, (section 3.2.1) "*Top* quark physics in hadron collisions". (2005) Rep. Prog. Phys. (68) 2409

[29] S. S. D. Willenbrock and D. A. Dicus, "Production of heavy quarks from W-gluon fusion", Phys. Rev. D 34, 155-161 (1986).

[30] The ATLAS Collaboration, "Generic ttbar resonance search with the ATLAS detector", Report number : ATL-COM-PHYS-2006-054 and ATL-PHYS-PUB-2006-033.

[31] B. S. Acharya et al.,"Re-discovery of the top quark at the LHC and first measurements", arXiv:0806.0484v1.

[32] W. Bernreuther, "Top-quark physics at the LHC" 2008 J. Phys. G: Nucl. Part. Phys. 35 083001

[33] L. G. Almeida et al., "Template Overlap Method for Massive Jets", arXiv:1006.2035v1.

[34] "High p_T Hadronic Top Quark Identification" Part I: Y. Splitter, "Jet Mass" ATL-COM-PHYS-2008-001 And Part 2: M. Vos, "The life time signature" ATL-PHYS-CONF-2008-016

[35] R. Brun and F. Rademakers, ROOT - An Object Oriented Data Analysis Framework, doi:10.1016/S0168-9002(97)00048-X.

[36] L. Evans and P. Bryant. "LHC Machine". JINST 3 S08001, 2008

[37] ATLAS Collaboration. Observation of a new particle in the search for the Standard Model Higgs boson with the ATLAS detector at the LHC. Phys.Lett. B716 (2012) 1-29 ; CMS Collaboration. Observation of a new boson at a mass of 125 GeV with the CMS experiment at the LHC. Phys.Lett. B716 (2012) 30-61

[38] ATLAS Collaboration. The ATLAS Experiment at the CERN Large Hadron Collider. JINST, 3:S08003, 2008

[39] S. Chatrchyan et al. The CMS experiment at the CERN LHC. JINST, 3:S08004, 2008.

[40] K. Aamodt et al. The ALICE experiment at the CERN LHC. JINST, 3:S08002, 2008.

[41] Jr. Alves, A. Augusto et al. The LHCb Detector at the LHC. JINST, 3:S08005, 2008.

[42] O. Adriani et al. The LHCf detector at the CERN Large Hadron Collider. JINST, 3:S08006, 2008.

[43] TOTEM Collaboration, G. Anelli, et al. The TOTEM experiment at the CERN Large Hadron Collider. JINST, 3:S08007, 2008.

[44] MoEDAL collaboration, James Pinfold, et al. Technical design report of the moedal experiment. Technical Report CERN-LHCC-2009-006. MoEDAL-TDR-001, CERN, Geneva, 2009

[45] E. Eichten, I. Hinchliffe, K. Lane, and C. Quigg. Supercollider physics. Rev. Mod. Phys., 56:579-707, Oct 1984

[46] ATLAS Collaboration. ATLAS high-level trigger, data acquisition and controls: Technical design report. 2003, CERN-LHCC-2003-022, ATLAS-TRD-016.

[47] D. Brandt and D. Brandt. Intermediate accelerator physics. Proceedings, CERN Accelerator School, Zeuthen, Germany, September 15-26, 2003. 2006, cds.cern.ch/record/603056/files/CERN-2006-002.pdf.

[48] O. Bruning, H. Burkhardt, and S. Myers. The large hadron collider. Progress in Particle and Nuclear Physics, 67(3):705 - 734, 2012.

[49] P. Schmser. Superconductivity in high energy particle accelerators. Progress in Particle and Nuclear Physics, 49(1):155 - 244, 2002.

[50] R. Assmann, M. Lamont, and S. Myers. A brief history of the LEP collider. Nucl.Phys.Proc.Suppl., 109B:17-31, 2002.

[51] L Rossi. Experience with lhc magnets from prototyping to large scale industrial production and integration. (LHC-Project-Report-730. CERN-LHC-Project-Report-730):Streaming video ; 6 transparencies, 2004, accelconf.web.cern.ch/AccelConf/e04/PAPERS/WEXCH01.PDF.

[52] R Bailey and Paul Collier. Standard filling schemes for various lhc operation modes. Technical Report LHC-PROJECT-NOTE-323, CERN, Geneva, Sep 2003, http://cds.cern.ch/record/691782/files/project-note-323.pdf.

[53] T. Bohl, O. Brunner, F. Dubouchet, D.C. Glenat, J. Lollierou, et al.. The LHC RF System - Experience with Beam Operation. Conf.Proc., C110904:202-204, 2011, accelconf.web.cern.ch/AccelConf/IPAC2011/papers/MOPC054.PDF.

[54] Luca Arnaudon, Philippe Baudrenghien, Olivier Brunner, and Andrew Butterworth. Operation Experience with the LHC RF System. Conf.Proc., C100523:TUPEB056, 2010, accelconf.web.cern.ch/AccelConf/IPAC10/papers/tupeb056.pdf.

[55] Oswald Grobner. Bunch induced multipactoring. Technical Report CERN-ISR-VA-77-38, CERN, Geneva, Jun 1977.

[56] Frank Zimmermann. A simulation study of electron-cloud instability and beam-induced multipacting in the lhc. Technical Report LHC-Project-Report-95. CERN-LHC-Project-Report-95. SLAC-PUB-7425, CERN, Geneva, Feb 1997.

[57] P. Chiggiato, V. Baglin, P. Cruikshank, J.M. Jimenez, G. Bregliozzi, et al.. Observations of Electron Cloud Effects with the LHC Vacuum System. Conf.Proc., C110904:1560-1562, 2011, accel-conf.web.cern.ch/accelconf/ipac2011/papers/tups018.pdf

[58] "The ATLAS Experiment", Work Book Atlas Experiment, https://atlas-computing.web.cern.ch/atlas-computing/projects/twikiUtils/twiki2pdf/cache/WorkBookAtlasExperiment.pdf

[59] The ATLAS Collaboration, "The ATLAS Experiment at the CERN Large Hadron Collider", JINST 3 S08003 2008, doi: 10.1088/1748-0221/3/08/S08003

[60] LHC layout, *http* : *//cdsweb.cern.ch/record/*841542.

[61] Figure from : http://scipp.ucsc.edu/personnel/atlas.html

[62] J. Pequenao and P. Schaffner. A computer generated image representing how atlas detects particles. Jan 2013, cds.cern.ch/record/1505342

[63] S Haywood, L Rossi, R Nickerson, and A Romaniouk. AT-LAS inner detector: Technical Design Report, 2. 1997, at-las.web.cern.ch/Atlas/GROUPS/INNER DETECTOR/TDR/tdr.html.

[64] ATLAS Collaboration. ATLAS liquid-argon calorimeter: Technical Design Report. 1996.

[65] ATLAS Collaboration. ATLAS tile calorimeter: Technical design report. 1996, at-las.web.cern.ch/Atlas/SUB DETECTORS/TILE/TDR/TDR.html.

[66] ATLAS Collaboration. ATLAS muon spectrometer: Technical Design Report. 1997, atlas.web.cern.ch/Atlas/GROUPS/MUON/TDR/Web/TDR.html.

[67] ATLAS Collaboration. Performance of Particle Identification with the ATLAS Transition Radiation Tracker. 2011, arXiv:1109.5925 [physics.ins-det].

[68] J Adelman, M Donega, S Fratina, S Heisterkamp, E Hines, E Klinkby, T Koffas, T Peterson, K Tackmann, and E Thomson. Study of high-threshold probability in the atlas transition radiation tracker. (ATL-COM-INDET-2011-009), 2011.

[69] ATLAS Collaboration. Expected Performance of the ATLAS Experiment - Detector, Trigger and Physics. 2009, 0901.0512.

[70] ATLAS Collaboration. Atlas pixel detector electronics and sensors. Journal of Instrumentation, 3(07):P07007, 2008.

[71] A. Ahmad et al.. The silicon microstrip sensors of the ATLAS semiconductor tracker. Nuclear Instruments and Methods in Physics Research Section A: Accelerators, Spectrometers, Detectors and Associated Equipment, 578(1):98 - 118, 2007.

[72] The ATLAS TRT collaboration, E Abat, et al.. The atlas transition radiation tracker (trt) proportional drift tube: design and performance. Journal of Instrumentation, 3(02):P02013, 2008.; ATLAS Collaboration. Expected electron performance in the ATLAS experiment. 2011, ATL-PHYS-PUB-2011-006.

[73] D. Green. The physics of particle detectors. Camb.Monogr.Part.Phys.Nucl.Phys.Cosmol., 12:1-361, 2000.

[74] E. Abat, J.M. Abdallah, T.N. Addy, P. Adragna, M. Aharrouche, et al.. Response and shower topology of 2 to 180 GeV pions measured with the ATLAS barrel

calorimeter at the CERN test-beam and comparison to Monte Carlo simulations. 2010, cds.cern.ch/record/1263861/files/ATL-CAL-PUB-2010-001.pdf.

[75] J. Matthews. A Heitler model of extensive air showers. Astroparticle Physics, 22:387-397, January 2005.

[76] P. Amaral et al.. Hadronic shower development in iron scintillator tile calorimetry. Nucl.Instrum.Meth., A443:51-70, 2000, hep-ex/9904032.

[77] J.C. Barriere et al.. The alignment system of the ATLAS barrel muon spectrometer. 2008, cds.cern.ch/record/1081769/files/muon-pub-2008-007.pdf.

[78] S Aefsky et al.. The optical alignment system of the atlas muon spectrometer endcaps. Journal of Instrumentation, 3(11):P11005, 2008.

[79] ATLAS Collaboration. Performance of the atlas trigger system in 2010. Eur. Phys. J. C, 72:1849, 2012, arXiv:1110.1530 [hep-ex].

[80] Fabian Kohn, Measurement of the charge asymmetry in top quark pair production in pp collision data at $sqrts$= 7 TeV using the ATLAS detector, arXiv:1204.0952 [hep-ex].

[81] ATLAS collaboration. Performance of the ATLAS Trigger System in 2010. Eur.Phys.J., C72:1849, 2012, 1110.1530.

[82] R. M. Harris, C. T. Hill, and S. J. Parke, Cross section for topcolor Z'(t) decaying to $t\bar{t}$, hep-ph/9911288.

[83] C. T. Hill and S. J. Parke, Top production: Sensitivity to new physics, Phys. Rev. D 49 (1994) 4454-4462, hep-ph/9312324.

[84] K. Agashe, A. Belyaev, T. Krupovnickas, G. Perez, and J. Virzi, LHC signals from warped

[85] B. Lillie, J. Shu, and T. M. P. Tait, Kaluza-Klein Gluons as a Diagnostic of Warped Models, Phys. Rev. D 76 (2007) 115016, [arXiv:0706.3960]

[86] B. Lillie, L. Randall, and L.T. Wang, The Bulk RS KK-gluon at the LHC. JHEP 09 (2007) 074, hep-ph/0701166.extra dimensions, Phys. Rev. D 77 (2008) 015003, hep-ph/0612015.

[87] M. Cacciari, G.P. Salam and G. Soyez, The Anti-k(t) jet clustering algorithm, JHEP 04 (2008) 63, arxiv:0802.1189.

[88] M. Cacciari, G. P. Salam, and G. Soyez, FastJet, http://fastjet.fr.

[89] B. Acharya, et al., Object selection and calibration, background estimations and MC samples for the Winter 2013 Top Quark analyses with 2012 data, Tech. Rep. ATL-COM-PHYS-2013-088, CERN, Geneva, Jan, 2013.

[90] D. Krohn, J. Thaler, and L.T. Wang, Jet Trimming, JHEP 1002 (2010) 084, 908 arXiv:0912.1342 [hep-ph].

[91] ATLAS Collaboration, Performance of large-R jets and jet substructure reconstruction with the ATLAS detector, ATLAS-CONF-2012-065, July, 2012.

[92] ATLAS Collaboration, G. Aad et al., Commissioning of the ATLAS high-performance b-tagging algorithms in the 7 TeV collision data, ATLAS conference note, ATLAS-CONF-2011-102, Jun, 954 2011.

[93] ATLAS Muon Combined Performance - Preliminary Guidelines for Analyses of 2012 Data, https://twiki.cern.ch/twiki/bin/viewauth/AtlasProtected/MCPAnalysisGuidelinesData2012.

[94] T. Chwalek, Messung der W-Boson-Helizittsanteile in Top-Quark-Zerfllen mit dem CDF II Experiment und Studien zu einer frhen Messung des ttbar-Wirkungsquerschnitts mit dem CMS Experiment. PhD thesis, Karlsruhe, U., Karlsruhe, 2010. http://cdsweb.cern.ch/record/1416031. Presented 12 Feb 2010

[95] ATLAS Collaboration, Improved Luminosity Determination in pp Collisions at $\sqrt{s} = 7$ TeV using the ATLAS Detector at the LHC, ATLAS-DAPR-2011-01-001, June, 2012.

[96] M. Botje, J. Butterworth, A. Cooper-Sarkar, A. de Roeck, J. Feltesse, et al., The PDF4LHC Working Group Interim Recommendations, arXiv:1101.0538 [hep-ph].

[97] R. D. Ball, V. Bertone, S. Carrazza, C. S. Deans, L. Del Debbio, et al., Parton distributions with LHC data, Nucl.Phys. B867 (2013) 244-289, arXiv:1207.1303 [hep-ph].

[98] H1 and ZEUS Collaboration. Combined Measurement and QCD Analysis of the Inclusive e+- p Scattering Cross Sections at HERA, JHEP 1001 (2010) 109, arXiv:0911.0884 [hep-ex].

[99] M. Aliev, H. Lacker, U. Langenfeld, S. Moch, P. Uwer, et al., HATHOR: HAdronic Top and Heavy quarks crOss section calculatoR, Comput.Phys.Commun. 182 (2011) 1034-1046, arXiv:1007.1327 [hep-ph].

[100] A. Martin, W. Stirling, R. Thorne, and G. Watt, Uncertainties on alpha(S) in global PDF analyses and implications for predicted hadronic cross sections, Eur. Phys. J. C64 (2009) 653-680, arXiv:0905.3531 [hep-ph].

[101] M. Cacciari, M. Czakon, M. Mangano, A. Mitov, and P. Nason, Top-pair production at hadron colliders with next-to-next-to-leading logarithmic soft-gluon resummation, Phys.Lett. B710 (2012) 612-622, arXiv:1111.5869 [hep-ph].; M. Czakon and A. Mitov, Top++: A Program for the Calculation of the Top-Pair Cross-Section at Hadron Colliders, arXiv:1112.5675 [hep-ph].

[102] A. V. Manohar and M. Trott, Electroweak Sudakov Corrections and the Top Quark Forward-Backward Asymmetry, Phys.Lett. B711 (2012) 313-316, arXiv:1201.3926 [hep-ph].

[103] ATLAS Collaboration. Measurement of $t\bar{t}$ production with a veto on additional central jet activity in pp collisions at sqrt(s) = 7 TeV using the ATLAS detector, Eur.Phys.J. C72 (2012) 2043, arXiv:1203.5015 [hep-ex].

[104] ATLAS Collaboration, TopSystematicUncertainties for Winter 2012 (rel17) 5 fb^{-1} analyses, https://twiki.cern.ch/twiki/bin/viewauth/AtlasProtected/TopSystematicUncertainties, June, 2012.

[105] ATLAS Collaboration, MultijetJESUncertaintyProvider for Top for R17 analyses, https://twiki.cern.ch/twiki/bin/viewauth/AtlasProtected/MultijetJESUncertaintyProviderTop, May, 2012.

[106] ATLAS Collaboration, Jet mass and substructure of inclusive jets in $\sqrt{s}$= 7 TeV pp collisions with the ATLAS experiment, JHEP 1205 (2012) 128, arXiv:1203.4606 [hep-ex].

[107] ATLAS Collaboration, Unusual Jet Uncertainty Provider, https://twiki.cern.ch/twiki/bin/viewauth/AtlasProtected/UJUncertaintyProvider, July, 2012.

[108] ATLAS Collaboration, Jet Energy Resolution Provider, https://twiki.cern.ch/twiki/bin/viewauth/AtlasProtected/JetEnergyResolutionProvider, June, 2012.

[109] G. Choudalakis, On hypothesis testing, trials factor, hypertests and the BumpHunter, arXiv:1101.0390 [physics.data-an].

[110] D0 Collaboration, I. Bertram et al., A Recipe for the Construction of Confidence Limits, Fermilab-tm-2104, fermilab, 2000. http://lss.fnal.gov/archive/test-tm/2000/fermilab-tm-2104.shtml.

[111] J. Alwall, P. Demin, S. de Visscher, R. Frederix, M. Herquet, et al.. MadGraph/MadEvent v4: The New Web Generation. JHEP, 0709:028, 2007, arXiv:0706.2334 [hep-ph].

[112] P. Meade and M. Reece. BRIDGE: Branching Ratio Inquiry/Decay Generated Events. 2007, arXiv:0703031 [hep-ph].

[113] T. Sjostrand, S. Mrenna, and P. Z. Skands. PYTHIA 6.4 Physics and Manual. JHEP, 0605:026, 2006, arXiv:0603175 [hep-ph].

[114] A. Martin, W. Stirling, R. Thorne, and G. Watt, Parton distributions for the LHC, Eur.Phys.J. C63 (2009) 189-285, arXiv:0901.0002 [hep-ph].

[115] J. Alwall, P. Demin, S. de Visscher, R. Frederix, M. Herquet, et al., MadGraph/MadEvent v4: The New Web Generation, JHEP 0709 (2007) 028, arXiv:0706.2334 [hep-ph].

[116] A search for $t\bar{t}$ resonances in the lepton plus jets final state using 4.7 fb^{-1} of pp collisions at $\sqrt{s} = 7$ TeV, Tech. Rep. ATLAS-COM-PHYS-2012-1753, CERN, Geneva, Nov, 2012.

[117] Edmond L., et al., Higgs-flavon mixing and LHC phenomenology in a simplified model of broken flavor symmetry, arXiv:1406.6054.

List of Figures

List of Tables

Appendix

Gell-Mann Matrices

The Gell-Mann matrices are defined as:

$$
\begin{aligned}
\Lambda^1 &= \tfrac{1}{\sqrt{2}} \begin{pmatrix} 0 & +1 & 0 \\ +1 & 0 & 0 \\ 0 & 0 & 0 \end{pmatrix}, \Lambda^2 = \tfrac{1}{\sqrt{2}} \begin{pmatrix} 0 & -i & 0 \\ +i & 0 & 0 \\ 0 & 0 & 0 \end{pmatrix}, \\
\Lambda^3 &= \tfrac{1}{\sqrt{2}} \begin{pmatrix} +1 & 0 & 0 \\ 0 & -1 & 0 \\ 0 & 0 & 0 \end{pmatrix}, \Lambda^4 = \tfrac{1}{\sqrt{2}} \begin{pmatrix} 0 & 0 & +1 \\ 0 & 0 & 0 \\ +1 & 0 & 0 \end{pmatrix}, \\
\Lambda^5 &= \tfrac{1}{\sqrt{2}} \begin{pmatrix} 0 & 0 & -i \\ 0 & 0 & 0 \\ +i & 0 & 0 \end{pmatrix}, \Lambda^6 = \tfrac{1}{\sqrt{2}} \begin{pmatrix} 0 & 0 & 0 \\ 0 & 0 & +1 \\ 0 & +1 & 0 \end{pmatrix}, \\
\Lambda^7 &= \tfrac{1}{\sqrt{2}} \begin{pmatrix} 0 & 0 & 0 \\ 0 & 0 & -i \\ 0 & +i & 0 \end{pmatrix}, \Lambda^8 = \tfrac{1}{\sqrt{6}} \begin{pmatrix} +1 & 0 & 0 \\ 0 & 1 & 0 \\ 0 & 0 & -2 \end{pmatrix}.
\end{aligned} \tag{1}
$$